Accelerator Design Studies for the FCCee Positron Damping Ring and Transfer Line

John Adams Institute Student Design Project 2023

Darren Chan, **Sasha Horney**, **Emily Howling**,
Sebastian Kaloš, **Vlad Mușat**, **John Salvesen**
University of Oxford
Max Bosman, **Alex Keyken**
Royal Holloway, University of London
Ginevra Casati, **Rohan Kamath**, **Enzo Kuo**,
Runfeng Luo, **Rehanah Razak**
Imperial College London

Abstract

The electron-positron Future Circular Collider (FCCee) requires a complex of accelerators to create, damp and accelerate beams of positrons and electrons. Potential designs for aspects of the positron Damping Ring (pDR) and transfer line are presented in this report. Several options for a bunch compressor in the transfer line between the pDR and following accelerating stage were designed and analysed. The accelerator magnets for use in the pDR were designed and modelled. The models were optimised to meet the accelerator requirements. Cost and environmental impact were also considered.

Acknowledgements

We would like to acknowledge the contributions of the following:

Professor Emmanuel Tsesmelis

for all your time, expertise and support throughout the JAI course.

Rebecca Louise Ramjiawan

for your assistance of the lattice team.

Ian Martin, Zena Patel, Attilio Milanese

for your advice on magnet design and software.

Ciprian Plostinar

for your RF tutorials and support.

Thank you also to all other lecturers and guests who contributed to the JAI Accelerator Course.

Principal editor: **Emily Howling**
Deputy editor: **Sasha Horney**
Formatted by: **John Salvesen**

Lattice team: **Rohan Kamath, Sebastian Kaloš, Alex Keyken, Rehanah Razak**
Magnets team: **Darren Chan, Sasha Horney, Emily Howling, Enzo Kuo, John Salvesen**
RF Cavities team: **Max Bosman, Ginevra Casati, Runfeng Luo, Vlad Mușat**

Contents

List of Figures

List of Tables

Foreword

The John Adams Institute is one of two UK centres of excellence in accelerator science and technology, composed of a collaboration between the accelerator research groups at Royal Holloway University of London, Imperial College London and the University of Oxford. Each year, as part of their training, the first year doctoral students in the John Adams Institute are assigned a future accelerator design, on which to complete a group project on over the course of an academic term. This report presents the work done by the students for this year's project: accelerator design studies for the FCCee positron damping ring and transfer line. The thirteen students split into three groups to work on the lattice, the magnets and the radio-frequency cavities, respectively. Weekly meetings were held with all students present to foster collaboration between the different groups. The results of the project were first presented as a John Adams Institute seminar [1] and later presented at the 2023 John Adams Institute Advisory Board meeting [2]. A seminar was also delivered to members of the FCCee study team at CERN.

Chapter 1

Introduction

1.1 Physics Addressed by FCCee

There are many unsolved problems in particle physics, such as the hierarchy problem, dark matter, baryon asymmetry and neutrino masses. To make progress in resolving these issues it is necessary to push the frontiers of energy, intensity and precision in high energy physics.

The FCCee would be a 91.17 km ring underneath the Franco-Swiss region around CERN, colliding electrons and positrons. It would be at the precision frontier of high energy physics, providing an electroweak and Higgs factory. Since lepton colliders are colliding fundamental (rather than composite) particles, they have much cleaner signals than hadron colliders making it easier to reconstruct events precisely.

The FCCee would run at four energies and have four interaction points. The energies are chosen to optimise the production of certain particles. These four energy modes are at the Z pole, WW threshold, ZH (to provide a Higgs factory), and around the $t\bar{t}$ threshold [3].

At the Z pole, there could be studies of flavour physics, including decay modes unreachable by LHCb or Belle 2, i.e. $\mathcal{B}(B_0 \to K^*(892)\tau^+\tau^-)$ and $B_c^+ \to \tau^+\mu_\tau$. Running at the Z pole energy in a circular collider means that the electroweak and Higgs sectors measurements can be taken in isolation from each other [4].

As a Higgs factory, the FCCee would be used to make precision measurements of the Higgs mass, branching ratios and self coupling. The FCCee Higgs physics programme would be complementary to the LHC's, with FCCee producing Higgs bosons at a lower rate, but providing measurements with greater precision. FCCee would also undertake precision studies of the electroweak sector,

including electroweak top quark couplings.

1.2 Comparison with Other Future Colliders

There are currently several designs being developed for a future collider. Some of these designs are circular, like the FCC, whereas others such as CLIC and ILC are linear colliders. Most collide electrons and positrons, but there are also designs for muon colliders being developed. The potential parameters and cost estimates of some of the future accelerators being planned are given in Table 1.1.

Accelerator	Topology	Energy, TeV	Int. Luminosity, a^{-1}	Power, MW	Cost, GCHF
FCCee	Circular	0.091+0.16	150+10	259	10.5
		0.24	5	282	
		0.365 (+0.35)	1.5 (+0.2)	340	+1.1
CEPC	Circular	0.091+0.16	16+2.6	149	4.8
		0.24	5.6	266	
ILC	Linear	0.25	2	129-200	7.15
		0.5	4	153-204	
		1		300	
CLIC	Linear	0.38	8	168	5.9
		1.5	7	(370)	+5.1
		3	8	(590)	+7.3

Table 1.1: Comparison of different future accelerators [5][6].

One advantage of the FCCee over alternative future accelerators being studied is that it provides the highest luminosity for input power of all proposals. Per Higgs boson event, the electricity cost would be ∼200 CHF [7].

Another advantage is that it could be succeeded by a 100 TeV hadron collider in the same tunnel, FCChh. If a linear collider were built instead, it is less likely that the infrastructure would be able to be directly repurposed for a hadron collider at the high energy frontier in the future. Another potential stage would be FCCeh, which would collide leptons and hadrons to study high-precision quantum chromodynamics and probe the structure of hadrons [8].

Since it is a circular collider, the FCCee would provide high precision centre-of-mass calibration for the Z and W modes due to availability of transverse polarisation up to over 80 GeV beam energy.

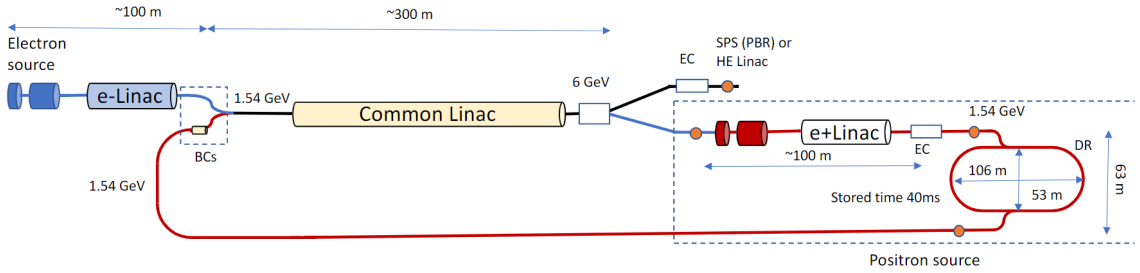

Figure 1.1: A schematic of the Linacs and pDR for generating positrons and accelerating both positrons and electrons to 6 GeV for the FCCee. [9]

This would not be possible in linear colliders such as CLIC and ILC.

A muon accelerator is an exciting prospect, but the novel technology development needed to create such an accelerator is far greater than what would be needed for the FCC, meaning it is a less feasible solution in the next few decades. One challenge is that muons have a lifetime of 2.2 μs at rest so it is necessary to produce, accelerate and collide them very quickly before they decay.

Overall, the FCCee is a future collider design well suited to measuring the properties of standard model particles with excellent statistical precision and experimental accuracy, as well as providing infrastructure that could be repurposed for the FCChh and FCChe, providing tools for a century of particle physics research [7].

1.3 FCCee Pre-injector Complex

A chain of several accelerators is needed to create the high energy beams of electrons and positrons needed for the FCCee. The positrons for collision will be created by firing electrons at a target. The positron beam will initially have a high emittance, which will be reduced by the positron damping ring. Then both the electrons and positrons will be accelerated to 6 GeV by a series of linacs, as shown in Fig.1.1.

There are a few accelerators being considered to increase the particle energy from 6 GeV to 20 GeV. One option would be re-purposing the Super Proton Synchrotron, but a new high energy linac is also being considered.

The final stage of acceleration before the collider will be a high energy booster ring which will increase the particle energy from 20 GeV to the energy needed for collisions (depending on which mode the collider is running in). This booster ring will have the same 91.17 km circumference as the FCCee and be in the same tunnel, as shown in Fig.1.2. The booster will be used to fill the

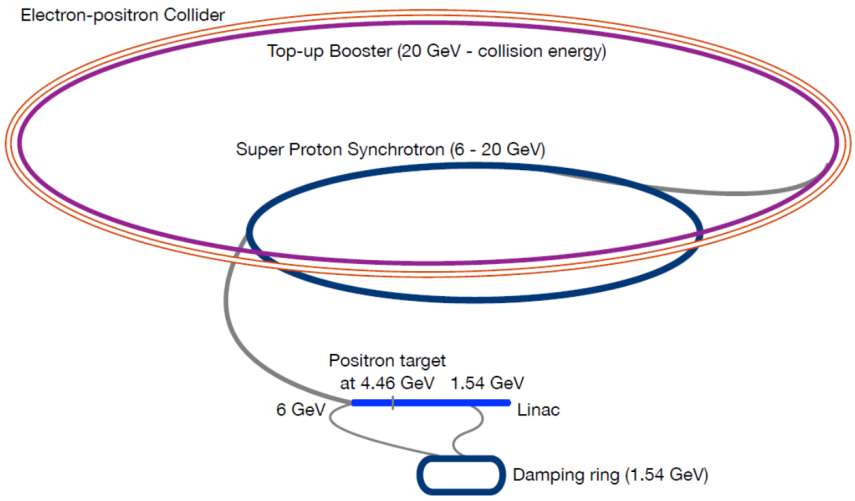

Figure 1.2: A schematic of the accelerator complex for the FCCee if the SPS is used. [10]

collider as well as provide regular top up injection.

1.4 FCCee Positron Damping Ring and Tranfer Line

The purpose of the positron damping ring is to reduce the emittance of the beam of positrons. It is a 241.8 m ring accelerating 5 trains of 2 bunches, with each train 100 ns apart [3]. The emittance is primarily reduced through synchrotron radiation damping in the wigglers. It is important to keep the beam focused and with minimal chromaticity using quadrupole and sextupole magnets. Kicker and septum magnets are used to inject and extract the beam and RF cavities are used to accelerate the beam and compensate for energy loss through synchrotron radiation.

Chapter 2

Lattice

2.1 Introduction

2.1.1 Overview

The lattice for the pDR has already been designed, so the lattice team in this project were instead allocated designing a bunch compressor for the transfer line. This transfer line takes the beam of positrons from the pDR to the common linac, as shown in Fig. 1.1.

The lattice part of this project comprises the design of two bunch compressor configurations. A compressor will be attached to the end of the positron transfer line, taking emittance-damped 1.54 GeV positrons from the damping ring back to the common linac [3]. Bunch compressors reduce the longitudinal bunch length of a particle beam by rotating the longitudinal phase space [11]. In particle accelerators, this technique is often used to increase the beam's peak brightness, and is required for a proper injection of the positron bunches back into the linac in the FCCee pre-injector complex.

The method of compressing a particle bunch is analogous to doing the same to a group of runners at a track; to have a longitudinally dispersed group of runners cross the finish line at the same time, one can let each runner follow a different path through the final corner, with faster ones completing a longer distance, and slower runners shorter. On the track, faster runners would lead the pack, and slower runners would be at its tail, corresponding to an "energy chirp". In an accelerator, however, this does not arise naturally; particles oscillate longitudinally back and forth within the bunch, higher momentum particles being mixed with those of lower momentum. To provide this correspondence between a particle's relative longitudinal position within the bunch

with its relative momentum offset, an RF cavity operating in phase with the synchronous (central) particle can be used. A bunch compressor, in a nutshell, is then a set of magnetic optics comprising a chicane, through which particles of different momenta travel different paths due to their difference in bending radii. By combining an energy chirp with the right magnetic elements, one can tune the final length of the particle bunch to the needs of a particular accelerator.

A particle bunch in an accelerator is centred around a hypothetical synchronous particle, which exactly follows the designed trajectory. Other particles are ahead or lagging, as shown in Fig.2.1. Each particle experiences some acceleration due to the sinusoidally varying electric field within an RF cavity. If we set the phase of these oscillations to be match the reference (synchronous) particle, only the momenta of the lagging and ahead particles will be altered. This way, particles are sorted spatially based on their momentum. As the ahead/lagging particles take paths of various lengths through the bunch compressor optics, we get what appears as a rotation of the bunch in the longitudinal phase space, as shown in Fig. 2.2. As long as there is no net acceleration, the longitudinal emittance, remains constant. This means that the compression of the bunch longitudinally necessarily comes with its spreading in momentum space. Therefore, a balance between the required compression and allowed momentum spread needs to be found for a specific system [12].

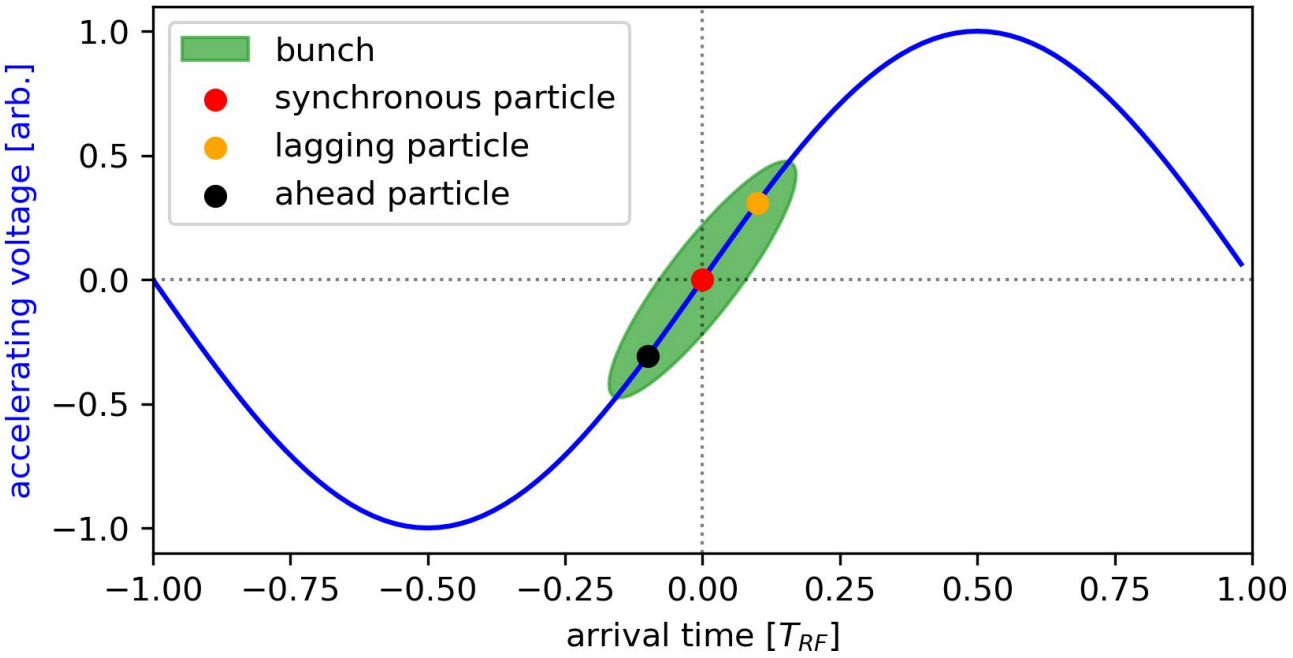

Figure 2.1: Distribution of particles in a bunch before receiving an energy chirp from the RF cavities.

Bunch compressors are necessary for high-energy accelerator/collider systems, such as the FCCee, as they require high peak currents. This means the bunch must be compressed to widths in the pico/femtosecond range to generate the required high peak current necessary for the FCCee

positron beam energy, which is in the order of GeV [13]. They are also necessary to reduce the effects of spatial dispersion experienced due to space charges within the beam. During acceleration, this causes stretching of the bunch length and hence increase of the longitudinal beam emittance [13].

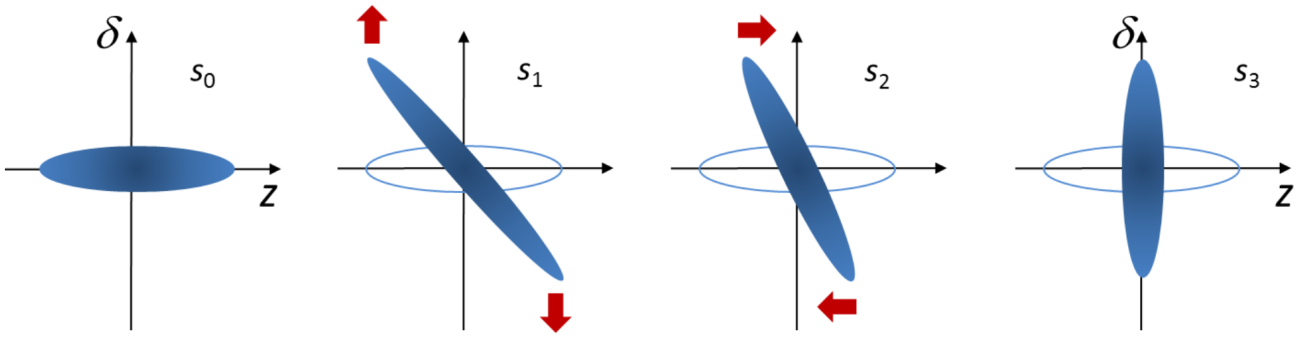

Figure 2.2: Example of a bunch (distribution of particles) rotating in longitudinal phase space, with a conserved area [14].

The magnetic optics for the bunch compressor designs consist of dipoles and focusing and defocusing quadrupoles in varying arrangements. The two configurations of bunch compressors that were designed as a part of this work are:

- C-bend Achromat
- FDDF Dog-Leg

2.1.2 Design Requirements

The bunch compressor was designed for 1.54 GeV bunches of positrons. These bunches have a 0.1 % momentum spread upon exit of the pDR. They then travel down the FCCee positron transfer line and are compressed from an initial RMS bunch length of 2 mm to the desired 1 mm. These compressed 1 mm bunches then enter the common linac [15].

2.2 Theory

Optical bunch compressors rely on introducing a velocity-dependent path length difference using a dipole. This means the time of flight is longer for the particles ahead of the bunch centre (synchronous particle) than for the particles lagging. As a result, the lower momentum particles

at the tail of the bunch will be deflected more by the dipole and travel a longer path than the higher momentum particles.

The effectiveness of the bunch compression process using dipoles depends on the initial distribution of particles in the bunch. In cases where the particles' momenta are uniformly distributed across the bunch, applying dipoles alone would merely cause particle rearrangement without noticeable compression of the bunch length. To overcome this limitation, an RF cavity is introduced before the dipoles to provide an energy chirp in the bunch.

An energy chirp refers to a modulation in the energy of the particles in the bunch as they pass through the cavity. This modulation is typically achieved by varying the frequency or phase of the RF field in the cavity. The following section provides the mathematical motivation for this and elucidates how parameters for the lattice were chosen.

For particles that travel through an element, their 6D coordinates before and after can be mapped to each other using a transfer matrix,

$$x_i = \mathbf{R}_{ij} x_j \tag{2.1}$$

where x_i and x_j are final and inital positions, and R_{ij} is the transfer matrix.

Since this project focuses on a longitudinal bunch compressor, the R_{55}, R_{56}, R_{65}, R_{66} parameters of these elements were the relevant parameters to consider and optimise.

2.2.1 Cavity

In the longitudinal plane, for a particle in a bunch passing through an RF cavity, its fractional momentum offset from the central particle can be given by:

$$\delta' = \delta \left(1 - \frac{qV}{E_s} sin\phi_s\right) - \frac{qV}{E_s}\Big(sin(\phi_s - k_{rf} z) - sin\phi_s\Big) \tag{2.2}$$

where V is the voltage of the RF cavity, k_{rf} its wave vector, and E_s the energy of the incoming beam and ϕ_s is the phase of the synchronous particle and δ' and δ are its fractional momentum offsets before and after the RF cavity. [16].

The term $k_{rf} z$ represents the deviation in phase of the particle from the synchronous particle.

Assuming this deviation is small, the above equation reduces to:

$$\delta' = \delta\left(1 - \frac{qV}{E_s} sin\phi_s\right) - z\frac{qVk_{rf}}{E_s} cos\phi_s \tag{2.3}$$

We also assume the RF cavity does not change the position of the particle with respect to the reference particle under the thin lens approximation. Under this, we can rewrite the above in matrix form,

$$\begin{bmatrix} x_5' \\ x_6' \end{bmatrix} = \begin{bmatrix} 1 & 0 \\ R_{65} & R_{66} \end{bmatrix} \begin{bmatrix} x_5 \\ x_6 \end{bmatrix} \tag{2.4}$$

where the R_{65} and R_{66} parameters take the form:

$$R_{65} = \frac{qVk_{rf}}{E_s} cos\phi_s \tag{2.5}$$

and

$$R_{66} = 1 - \frac{qV}{E_s} sin\phi_s \tag{2.6}$$

with all terms as previously defined.

2.2.2 Optics

The optics of an accelerator refers to the distribution and properties of the magnets in the accelerator that focus and bend the beam.

Following the RF cavity, the particles go through the magnet optics. Under a conservative force, magnets cannot change the momentum offset of a particle. Hence, we can set R_{65} and R_{66} to 0 and 1 respectively.

The parameter which is required is R_{56}, and refers to the change in path length as a function of momentum offset. For any given optical element, the R_{56} parameter can be related to the dispersion function as ,

$$R_{56} = \int_0^L \frac{D(s)}{\rho} ds \tag{2.7}$$

where $D(s)$ is the dispersion function and ρ is the bending radius. This can be further simplified based on the specific optics and is discussed in the following sections.

2.2.3 Parameter Optimisation

We can combine all of the above to optimise the bunch compressor. This gives us,

$$\begin{bmatrix} x_5' \\ x_6' \end{bmatrix} = \begin{bmatrix} 1 & R_{56} \\ 0 & 1 \end{bmatrix}^{optics} \begin{bmatrix} 1 & 0 \\ R_{65} & R_{66} \end{bmatrix}^{cavity} \begin{bmatrix} x_5 \\ x_6 \end{bmatrix} \tag{2.8}$$

as the overall transfer matrix. For a given particle, its initial and final position in the bunch can be related as,

$$z' = (1 + R_{56}^o R_{65}^c)z + R_{56}\delta \tag{2.9}$$

where z and z' are its positions before and after the bunch compressor respectively.

Averaging over all particles in the bunch, the RMS bunch length is given by,

$$\sigma' = \sqrt{(1 + R_{56}^o R_{65}^c)^2\sigma^2 + R_{56}^2\delta^2} \tag{2.10}$$

which is minimised when $R_{56}^o = -1/R_{65}^c$. Hence, a specific setting of the RF cavity system works in tandem with a specific configuration of the magnetic optics chicane to achieve the desired bunch compression.

Two bunch types of compressors were designed using these analytic results as a starting point. The optics were matched to the end of the pDR transfer line given in the MADX files provided[17]. The various configurations were implemented and further optimized using the MADX program [18].

2.3 C-bend Achromat

2.3.1 Layout

One possible design of a bunch compressor is the C-bend achromat. The name comes from it being a 'C' shape and achromat refers to fact that the dispersion function of the lattice remains zero downstream of the compressor. The layout of one cell of such design is shown in Fig.2.3. Upon introducing an energy chirp in an RF cavity system, particles are deflected to a parallel trajectory via a set of two magnetic dipoles and then back to the axis of the original trajectory. The structure is axially symmetric. In a simple system like this, particles of higher momenta travel a shorter

path, corresponding to a specific R_{56} value, depending on the exact settings. The R_{56} parameter in this case, however, can be tuned by varying the magnetic field gradient of two additional focusing quadrupoles inserted between the first two and last two quadrupoles. An additional defocusing quadrupole must be inserted in the middle of the lattice to preserve the achromaticity of the design. Its gradient K_2 needs to be tuned in sync with K_1.

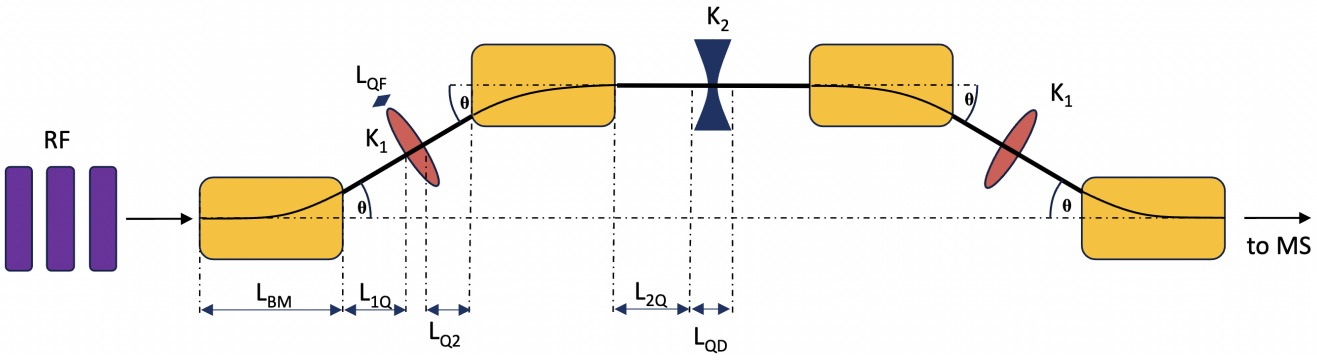

Figure 2.3: 2D layout of a C-bend achromat. Dipoles are in yellow, focusing quadrupoles are in red, defocusing quadrupole are in blue, and RF cavities are in violet. K_1 and K_2 refer to the strengths of the quadrupoles.

Up to the first order, the analytical expression for R_{56} for such a design reads,

$$R_{56} = -2\left(L_{12} + \frac{2}{3}L_{BM}\right)\theta^2 - L_{BM}\theta^2 - 2K_1\left(L_{1Q} + \frac{L_{BM}}{2}\right)\left(L_{Q2} + \frac{L_{BM}}{2}\right)\theta^2 \tag{2.11}$$

where L_{12} is the distance between the end of the first dipole and the beginning of the second along the original beam axis, L_{BM} is the length of the bending magnet, and θ is the bending angle of the dipole [16].

Figure 2.4 shows the global layout of the combined transfer line and the C-bend achromat bunch compressor. The 1.54 GeV emittance-damped positron beam passes through a straight section composed of F0D0 cells, followed by a 2-section arc bending the trajectory by 180 degrees, orienting the beam along the main linac (shown in Fig. 1.2). Using the approach explained in section 2.2, a set of parameters suitable for the transfer line and capable of delivering the desired compression was converged upon. Crude analysis was done analytically, with fine-tuning performed in MADX.

2.3.2 Results

To provide a sufficient energy chirp, and final bunch compression, it was found that the design shown in Fig. 2.4 is suitable. A matching section (MS_{ARC}) already used upstream in the transfer line connects the arc to a FODO cell, followed by three identical RF cavities operating at 3 GHz

and 10 MV peak accelerating voltage, followed by three identical C-bend cells coupled to each other via custom matching sections. The parameters of each C-bend cell , RF system, and the matching sections are presented in Table 2.1.

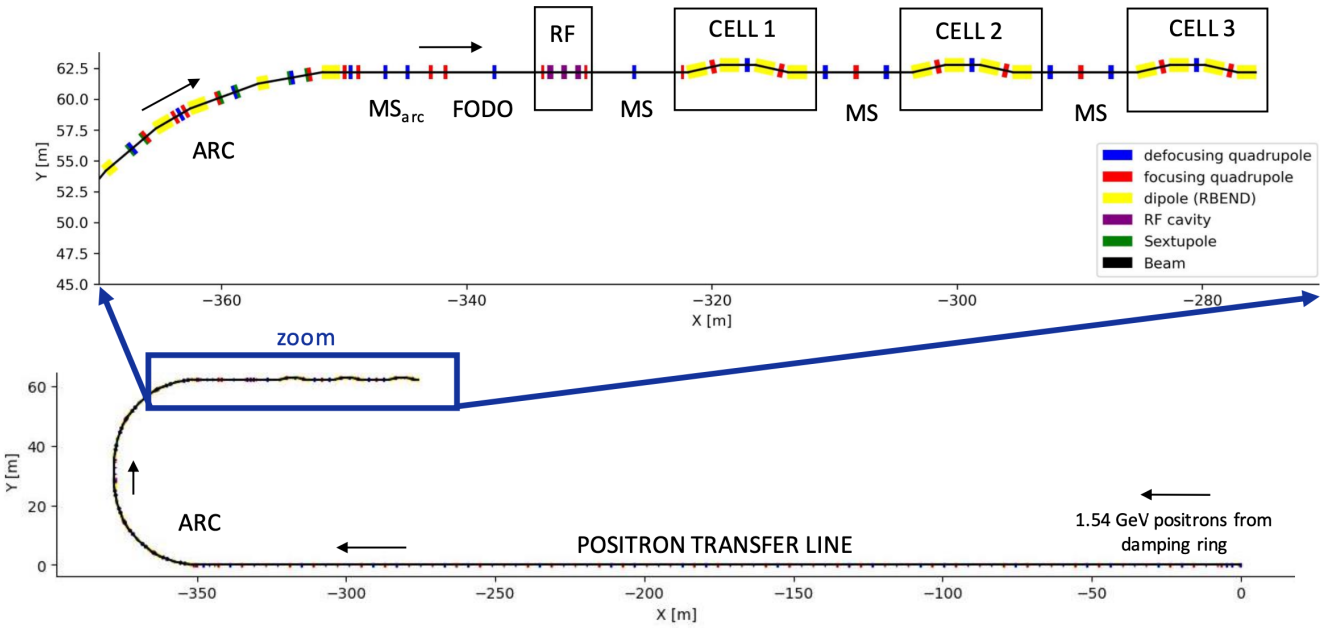

Figure 2.4: Global layout of the C-bend achromat positioning within the pre-injector complex.

Dimension	Value (m)	Magnet Parameter	Value	RF Parameter	Value
L_{BM}	1.5	K_1	1.1 m^{-2}	f (acc. frequency)	3 GHz
L_{1Q}, L_{Q2}	0.45	K_2	1.92 m^{-2}	V (peak acc. voltage)	10 MV
L_{QF}	0.3	θ	12.5°	# of cavities	3
L_{2Q}	0.55	K_{MS}	±1.5 m^{-2}		
L_{QD}	0.3				
L_{MS0}	1.4				
L_{MS1}	2.2				

Table 2.1: Key parameters of the final C-bend achromat design.

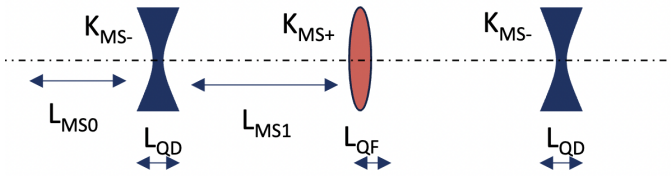

Figure 2.5: 2D layout of a matching section connecting two C-bend cells.

The layout of the matching section is shown in Fig. 2.5. Using these parameters and assuming a Gaussian particle distribution in the longitudinal phase space at the entrance to the transfer line, the development of the bunch phase-space is presented in Fig.2.6. The element sequence, dispersion, and β functions are plotted against the distance s along the beamline in Fig.2.7.

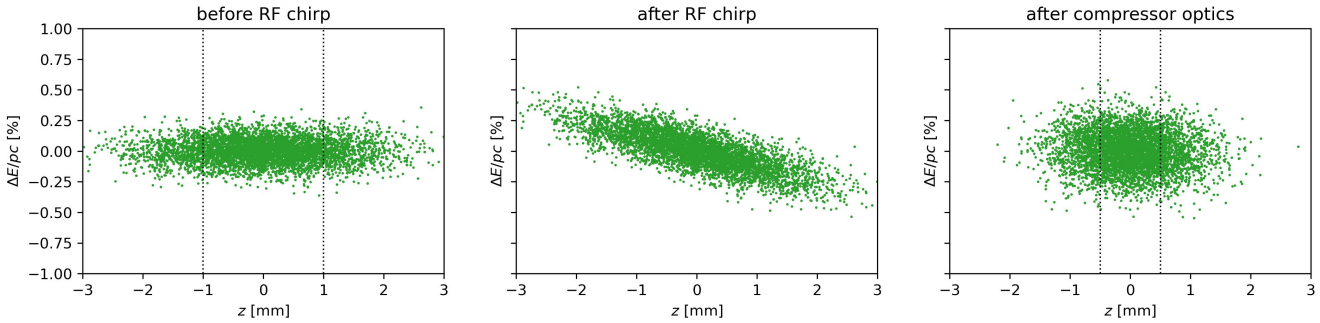

Figure 2.6: Plot of the longitudinal phase space development, denoting its state before, during, and after passing through the full bunch compressor sequence.

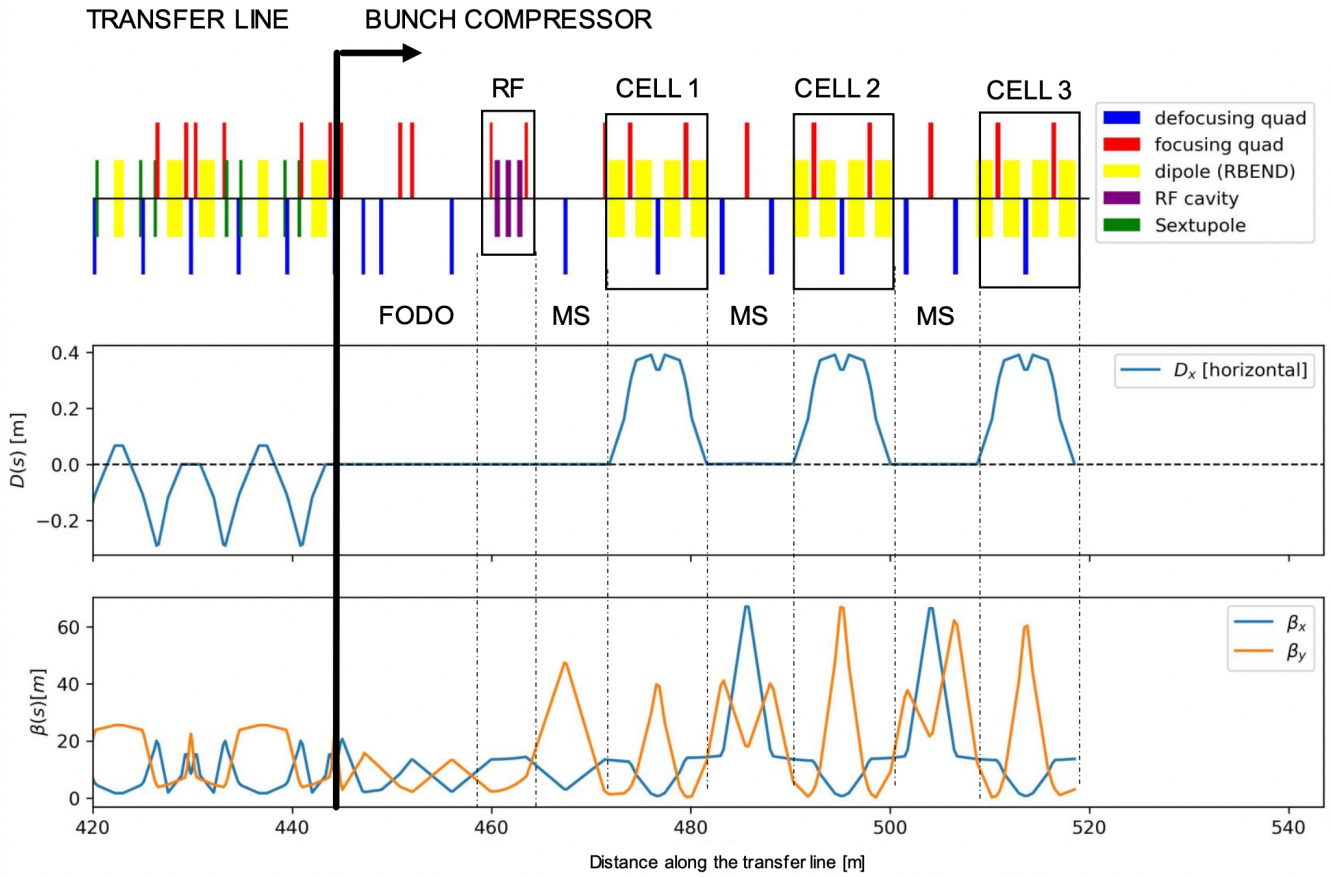

Figure 2.7: Plot of element sequence, dispersion, and β function along the transfer line. The vertical black line denotes the end of the pre-existing transfer line and the beginning of the design developed in this study.

2.3.3 Discussion

Figure 2.6 shows a good longitudinal compression of the bunch, from 2 mm to 1 mm RMS, while preserving a low momentum spread. This result was arrived at after taking into consideration the engineering works required for putting such systems in place.

The overall bunch compression is achieved by a combination of sufficient energy chirp and a sufficient difference in distance travelled by particles of different momenta. If one side of this relationship is limited, the other must compensate for it. The positron bunches' combination of energy and relative compactness places high requirements on the RF system. To provide sufficient chirp, i.e. difference in the electric field experienced by particles at the head and tail of the bunch, one needs to make the peak accelerating voltage and the operating frequency high. It was quickly realised that the cavities used in other sections of the FCCee (400 MHz and 800 MHz), including the damping ring, would not be sufficient. Therefore, a dedicated RF cavity must be designed, ideally to work at 3 GHz, and 10 MV peak accelerating voltage.

To increase the R_{56} of the compressor optics, i.e. the amount of "longitudinal slipping", it is best to increase the bending angle of the dipole used. However, this increases the amount of synchrotron radiation which leads to energy loss from the beam and a decrease in emittance. A standalone synchrotron radiation study would be required to assess how much this is an issue for a given design. It was decided to use an angle of 12.5 degrees, which is a value large enough to keep the system relatively manageable in size, yet low enough to make the amount of synchrotron radiation reasonably low. As a result, three C-bend cells are required to provide sufficient longitudinal compression.

Although this system provides a sufficient bunch compression, it is apparent from Fig. 2.4 that the overall size of the compressor beamline is rather large. The added length would require around 75 m of tunnel, which would involve considerable civil engineering works. Also, an additional matching section bringing the compressed bunches back into the common linac needs to be added. With these concerns in mind, an alternative compressor design capable of bringing the positrons closer to the linac, with a smaller physical footprint, is presented next.

2.4 Dog-Leg Bunch Compressor

A dog-leg bunch compressor consists of a series of quadrupoles and sextupoles on a straight beam line, positioned between two dipole magnets with opposite bending angles. Both bending magnets contribute constructively to bunch compression. However, due to this dipole configuration, a beam

must undergo a 2π dispersive phase shift between the bending magnets to remain achromatic. Said phase shift features in any achromatic dog-leg design, causing contributions to compression (other than from the bending magnets) to cancel by symmetry.

A dog-leg is one of the simplest and shortest bunch compressor lay-outs, but tunability of the R_{56} parameter is limited. Furthermore, a dog-leg requires stronger magnets than most bunch compressors, meaning chromatic effects are more significant [19].

2.4.1 RF Kick

Minimal bunch length is achieved when $R_{65} = -1/R_{56}$. The final bunch length is proportional to R_{56}. Hence, R_{65} must be maximised. In an RF cavity with voltage V_{RF} and frequency f_{RF},

$$R_{65} = -\frac{qV_{RF}}{E_s}\frac{2\pi}{cf_{RF}} \tag{2.12}$$

where q is particle charge and E_s is synchronous energy.

As seen in Fig.2.8a and Fig.2.8b, V_{RF} and f_{RF} must be large, to minimise $|R_{56}|$. Therefore in this design the RF chirp for the dog-leg is provided by two RF cavities with $V_{RF} = 10$ MV and $f_{RF} = 8000$ MHz. Cavities with higher V_{RF} and f_{RF} are more expensive and difficult to design, providing minimal improvements to chirp. For positrons in the transfer line with $E_s = 1.54$ GeV, the bunch compressor must have $R_{56} = 0.36$ m. Additionally, the bunch compressor must include a synchronous phase shift of π radians, to match the signs of R_{56} and R_{65}, without longitudinally accelerating the bunch.

From the transfer matrix multiplication of elements in a dog-leg design, the R_{56} parameter is given by,

$$R_{56} \approx \frac{L_{BM}\theta^2}{3} \tag{2.13}$$

to first order. As mentioned previously, only the dipoles with length L_{BM} and bending angle θ contribute to compression. Given $L_{BM} = 1.0$ m, a bending angle of 60° is required, to match the RF chirp [20].

2.4.2 Focusing-Defocusing-Focusing Layout

Two focusing quadrupoles are required to introduce a 2π dispersive phase-shift between the dipoles. The magnets must be equal strength and separated by a distance corresponding to twice their

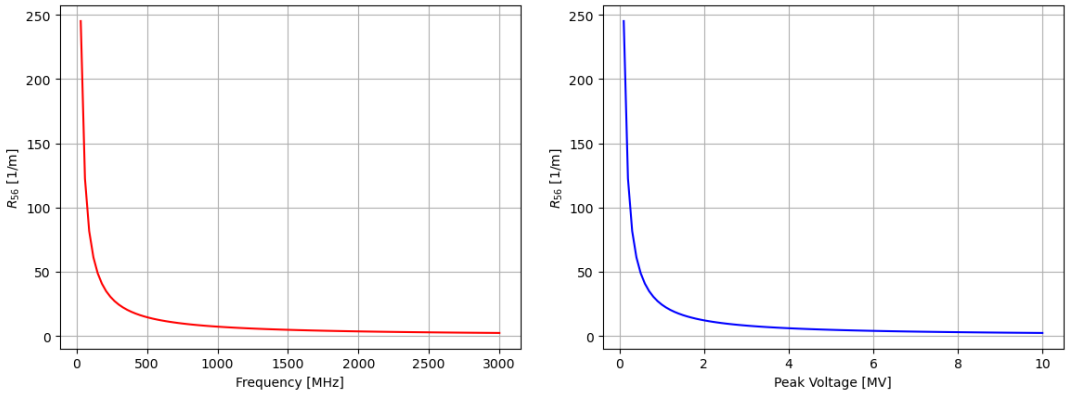

(a) The R_{56} parameter as a function of RF cavity frequency.

(b) The R_{56} parameter as a function of peak cavity voltage.

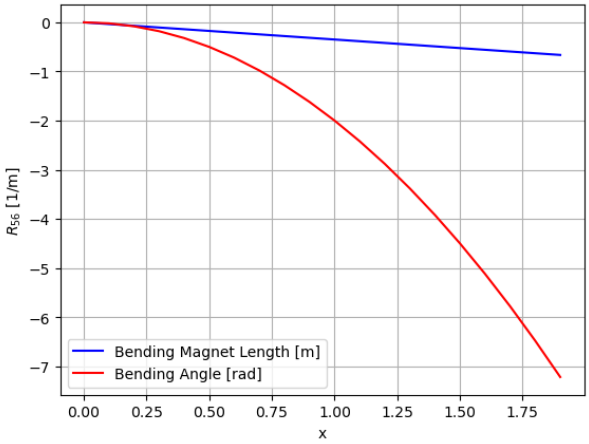

(c) The R_{56} parameter as a function of bending magnet length and angle.

Figure 2.8: R_{56} as a function of RF parameters V_{RF} and f_{RF}, and dog-leg parameters L_{BM} and θ.

focal length, to ensure symmetry and hence, achromaticity. A defocusing quadrupole situated on the point of zero dispersion allows tuning of the alpha and beta functions without disrupting achromaticity.

Dipole and RF settings have been discussed in Section 2.4.1. The distances between dipoles and quadrupoles L_1 and between quadrupoles L_2 are chosen to optimise Twiss parameter fits and the quadrupole strength is given by,

$$f = \frac{1}{\sqrt{K_{1f}}\sin\left(\sqrt{K_{1f}}L_Q\right)}. \tag{2.14}$$

where L_Q, f and K_{1f} are the quadrupole lengths, focal lengths and focusing strengths, respectively. The equation only holds for a small angle approximation, so the quadrupole triplet must obey the

stability condition,

$$f > \frac{L_{triplet}}{4}, \tag{2.15}$$

where $L_{triplet}$ is the length of the triplet. Choosing $L_Q = 0.5$ m, as is true for conventional quadrupoles, K_{1f} is calculated by combining Eq. 2.14 with the lens formula,

$$\frac{1}{f} = \frac{1}{L_1} + \frac{1}{L_2}. \tag{2.16}$$

where L_1 and L_2 are the distances as shown in Fig.2.9.

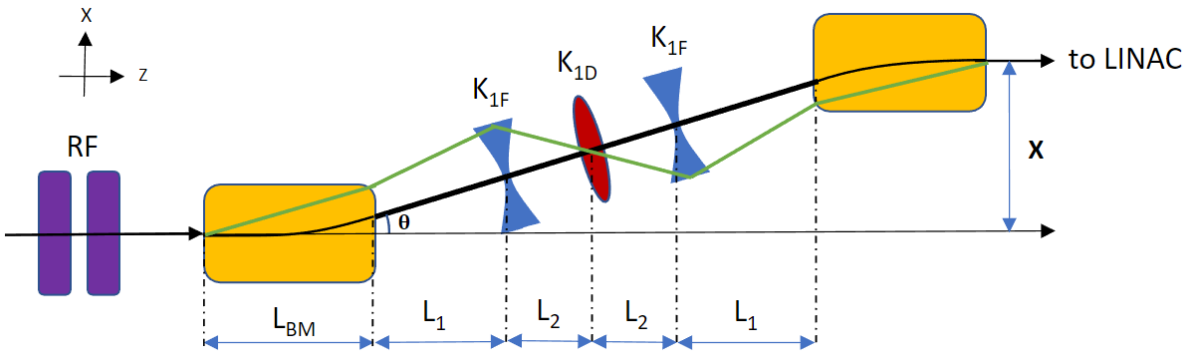

Figure 2.9: Top view schematic of the FDF dog-leg bunch compressor layout.

The quadrupole strength is then used as a starting parameter for MADX sequence matching. The defocusing quadrupole strength is not a variable due to the achromatic condition: $K_{1f} = K_{1d}$. Figure 2.9 shows a top view of the design. The geometric and matched parameters are given in Table 2.2.

Parameter	Value	Parameter	Value
L_{BM}	1.0 m	L_1	8.0 m
θ_{BM}	60 ± 1^{o}	L_2	2.0 m
L_Q	0.5 m	X	17.32 m
K_{1f}	$1.3 \pm 0.1\ m^{-2}$	Z	10 m
K_{1d}	$-1.3 \pm 0.1\ m^{-2}$		

Table 2.2: Optimized parameter settings. Uncertainties are given to account for MADX reduced matching sensitivity.

2.4.3 Focusing-Defocusing-Defocusing-Focusing Layout

High magnet strengths correspond to more pronounced chromatic effects which distort the final bunch and increase its length. The focusing quadrupole strength K_{1f} is lowered for larger quadrupole separation. This is achieved with defocusing quadrupoles not situated on zero dispersion points. The resulting layout is illustrated in Fig. 2.10.

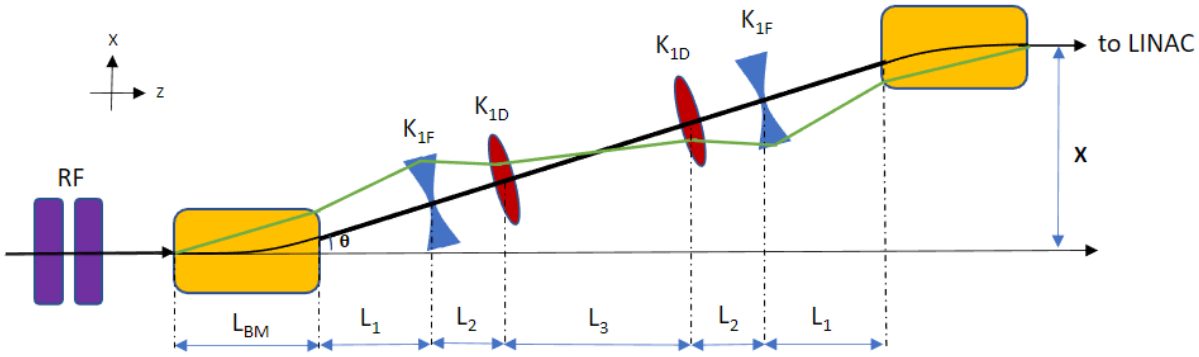

Figure 2.10: Top view schematic of the FDDF dog-leg bunch compressor layout. The bold black line shows the design trajectory and the green lines show a lower momentum dispersive path.

The optimisation is analogous to the process described in the previous section, with the approximate focal lengths given by lens equations:

$$\frac{1}{f_1} = \frac{1}{L_1} + \frac{2}{2L_2 + L_3}, \tag{2.17}$$

$$\frac{1}{f_2} = \frac{1}{L_1 + L_2} + \frac{2}{L_3}. \tag{2.18}$$

Parameter	Value	Parameter	Value
L_{BM}	1.0 m	L_1	8.0 m
θ_{BM}	$60 \pm 1^{\circ}$	L_2	2.0 m
L_Q	0.5 m	L_2	2.0 m
K_{1f}	$1.02 \pm 0.01\ m^{-2}$	X	24.25 m
K_{1d}	$-0.61 \pm 0.01\ m^{-2}$	Z	14.0 m

Table 2.3: Optimized parameter settings. Error bars are given to account for MADX reduced matching sensitivity.

2.4.4 Multiple Dog-leg Sequences

The following layouts are propositions for reducing dipole strength to further limit chromatic effects. However, as seen in Section 2.4.1, this will also require a modification of the RF. While it is possible to add more RF cavities, higher chirps mean higher uncorrelated momentum distributions and the bunch is more sensitive to over- or under-compression.

Instead, we consider multi-compressor sequence designs. Assuming each dog-leg contribution to compression is additive and that all dipole bending angles θ are equal, then chaining N dog-legs in succession reduces the angle by a factor of $1/\sqrt{N}$. Twiss parameters can be matched in designated matching sections between dog-legs, similar to the chicane approach. Using the values presented in Section 2.4.3, a triple dog-leg is created with bending angles of $\theta \approx 35^{o}$. The compressor sequence is small enough to fit within the spatial limit of 50 m along the z-axis, between the transfer line and linac. However, a double dog-leg design, shown in Figure 2.11, is capable of minimising the angle further by tuning R_{56} with a variable quadrupole.

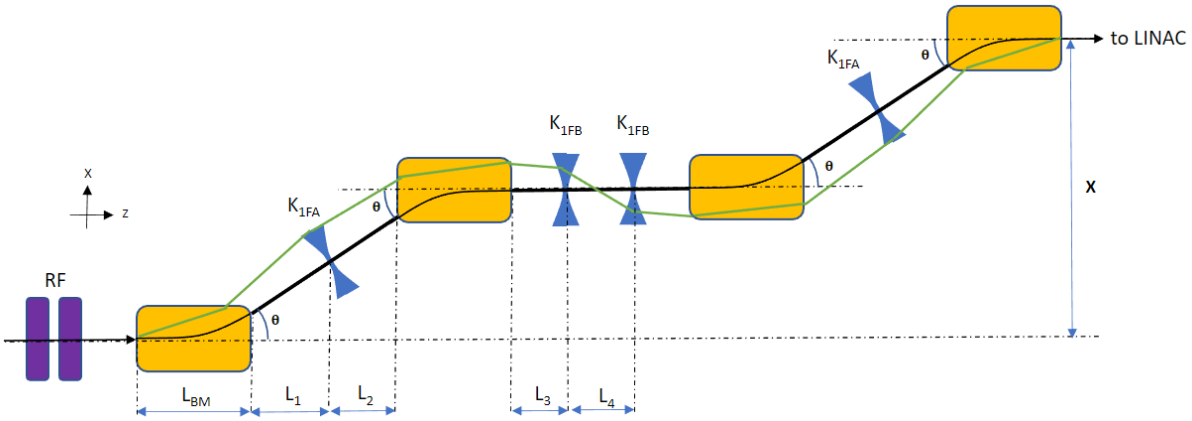

Figure 2.11: Top view schematic of the double dog-leg bunch compressor layout. The bold black line shows the design trajectory and the green lines show a lower momentum dispersive path.

The double dog-leg bunch compressor features two consecutive dog-legs, with a shared dispersive phase rotation in the central segment. The outer quadrupoles are adjustable and contribute to R_{56} by regulating the beam entry-angle and horizontal/vertical off-set at the second and third dipoles. Although the quadrupole contribution is very limited ($R_{56} \approx K_{1FA} L_{BM} \theta^2$), it allows another reduction of θ. This design is more compact than a dog-leg chain.

2.4.5 Dog-Leg Results

Parameters were optimised using the Fast Gradient Minimization method available through MADX matching. The method consists of minimising the numerical derivative of the sum of squares of the constraint functions [18].

Next, a python code was used to visualise the evolution of Twiss parameters along the track, as shown in Figure 2.12. MADX particle tracking provided the necessary information to reproduce the particle bunch phase space before entering the RF cavities, at the exit of the RF sequence and at the end of the bunch compressor. Results are shown in Fig.2.13 and Fig.2.14.

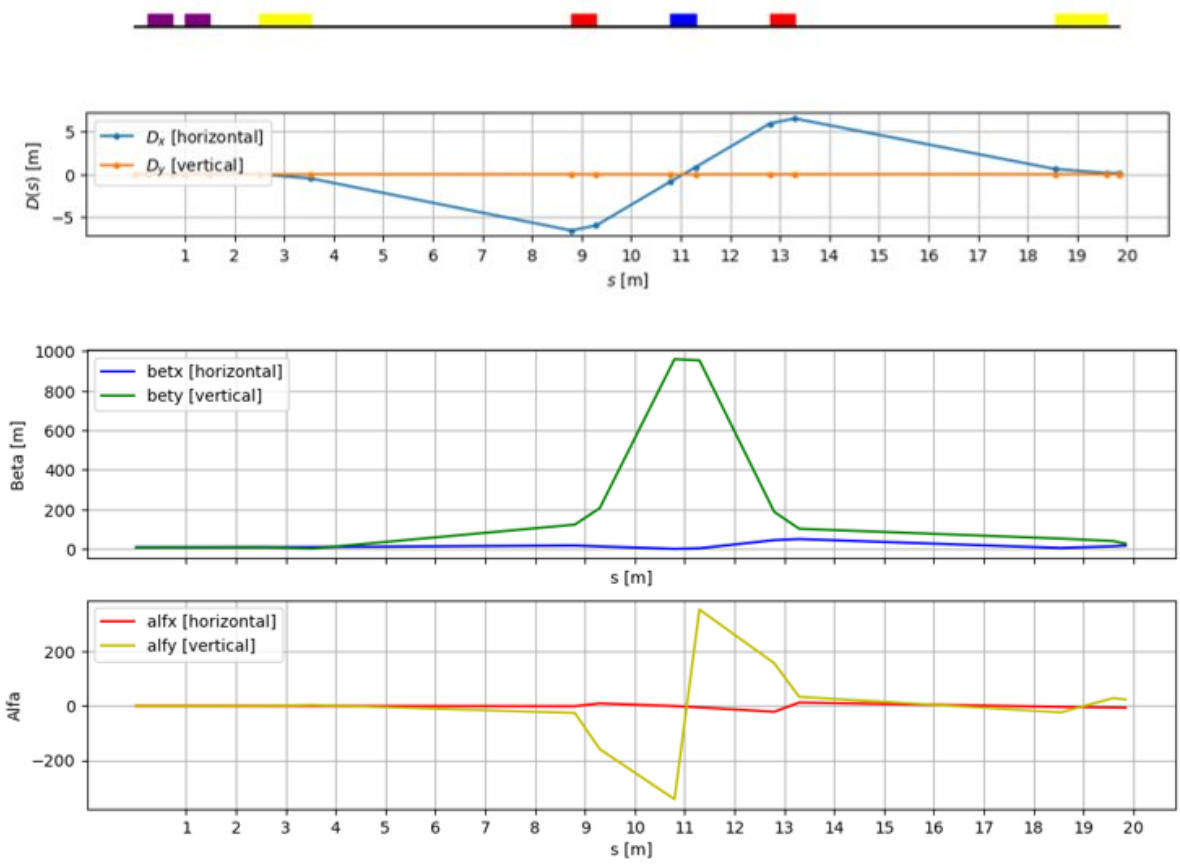

Figure 2.12: Graphs of horizontal and vertical Twiss paramters: D_x and D_y (top), β_x and β_y (centre), and α_x and α_y (bottom). For reference, the FDF layout has been graphed above the figures, in line with the x-axis. The blocks portray RF cavities in purple, dipoles in yellow, focusing quadrupoles in red and defocusing quadrupoles in blue. Due to the high quadrupole strengths, the final bunch features a tail in the negative energy domain.

The graph for dispersion shows the 2π phase shift and the alpha and beta functions match at the beginning and end as required. The slant in the beta peak where a straight section would be

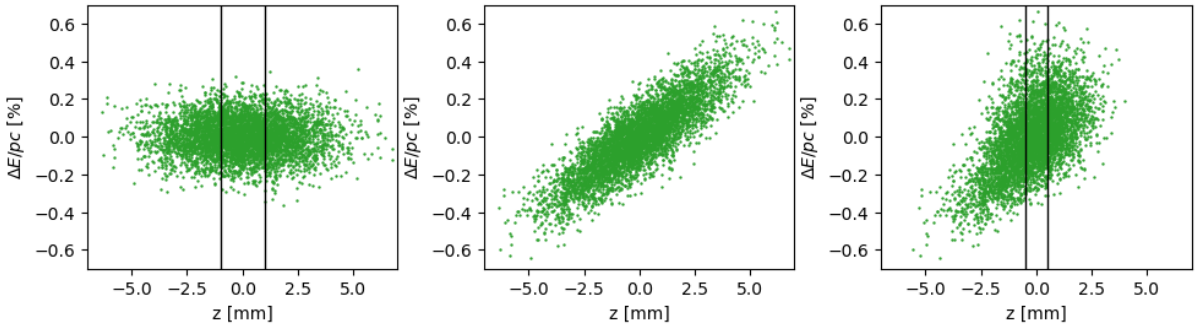

Figure 2.13: Energy-space bunch distribution of a beam containing 500 particles before compression (left), after receiving the RF chirp (centre) and at the end of the FDF dog-leg layout (right). Vertical lines show a FWHM of 2 mm before compression, and of 1 mm after compression. Due to higher order effects, the bunch features a tail spread in the direction of negative energy.

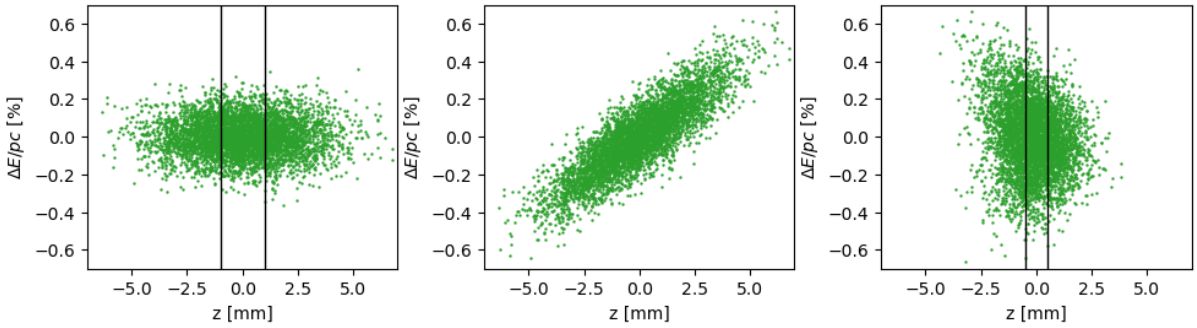

Figure 2.14: Energy-space bunch distribution of a beam containing 500 particles before compression (left), after receiving the RF chirp (centre) and at the end of the FDF dog-leg layout (right). Vertical lines show a FWHM of 2 mm before compression, and of 1 mm after compression.

expected is likely due to missing data points as the overall shape follows the expected parabola. The beta peak is large ($\beta_{max} \approx 1000$), but will be lower for smaller bending angles. A different matching method or matching with increased precision (smaller step size) would allow optimisation at smaller magnet distances (up to the minimum required by the stability condition) and lower the alpha and beta peaks further.

Following project requirements, the initial conditions for the beam match the end of the transfer line. The FWHM of the Gaussian distributed initial bunch is 2 mm, with a momentum dispersion of 0.1%. As expected, by setting $R_{56} = 0.36$ m, a bunch of 500 particles is successfully compressed to a FWHM width of approximately 1 mm.

A tail is observed on the final bunch for the FDF design, even at higher statistics (1500 particles). this has been attributed to chromatic effects from large quadrupole strengths. The deformation is not present in the result for FDDF, which demonstrates its capacity to reduce higher order effects.

Overall, dog-legs are simple and compact, with inherent horizontal displacement of the beam line, ideal for connecting the transfer line and linac. Hence the design requires fewer magnets than a chicane or arc FODO, but high magnet strengths cause more prominent chromatic effects which must be mitigated through sextupoles.

Since the required compression is achieved with multiple designs, it would be useful to analyse performance with the inclusion of higher order chromatic effects and synchrotron radiation.

2.5 Further Work

A more detailed study is required to assess which design is more suitable. The C-bend achromat design has a tunable R_{56} and can be considered more flexible in tuning the bunch length. However, it takes a large amount of space and requires additional matching sequences to be designed and built. Tuning of R_{56} in the dog-leg design is more limited. However, the lattice features fewer elements, is more compact, and directly matches the common linac.

Both designs require a deeper study of higher-order terms. The potential need for additional sextupoles, to deal with curvature in the longitudinal phase space needs further assessment.

A detailed analysis of the beam energy and emittance changes due to coherent synchrotron radiation in the bending dipoles must be done.

Lastly, a dedicated 3 GHz, 10 MV cavity needs to be designed.

Chapter 3

Magnets

3.1 Introduction

3.1.1 Overview

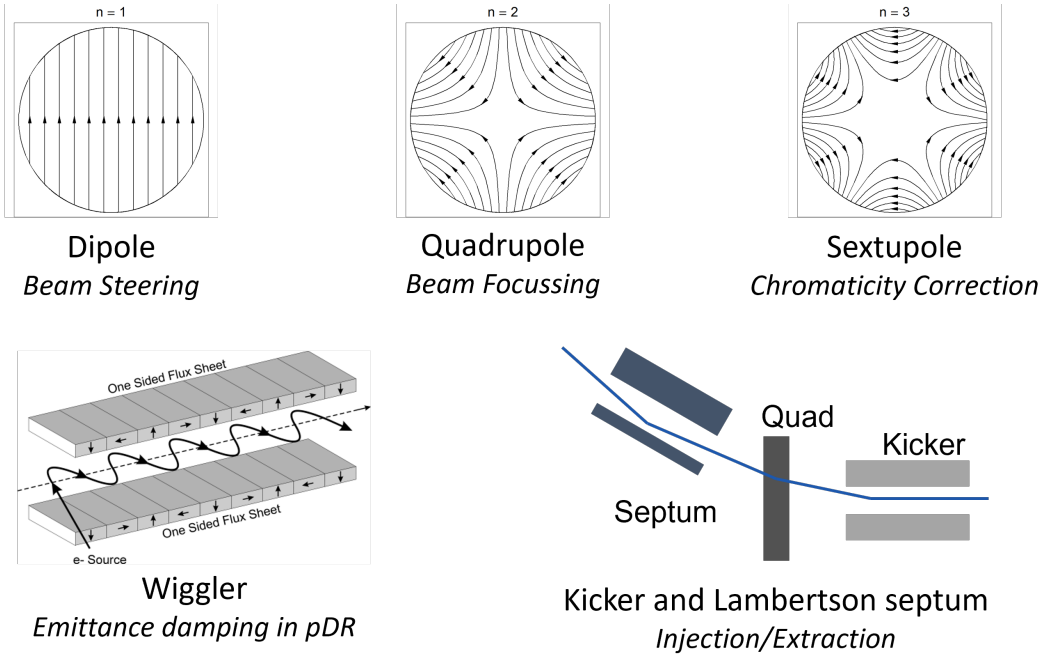

Figure 3.1: Schematic of the magnets or magnetic fields of the five types of magnets studied in the project.

In Chapter 2, the various desirable properties of the beam was outlined. Magnets play an extremely important role in accelerator design as they are responsible for many of the beam manipulations re-

quired to achieve these properties. For example, in Sections 2.4 and 2.3.1, the designed components were constructed primarily out of magnets such as dipoles, quadrupoles, and sextupoles.

For this design project, five types of magnets were modelled, which are shown in Fig. 3.1.

Each of these magnets will be installed in or around the pDR, as shown in Fig. 3.2.

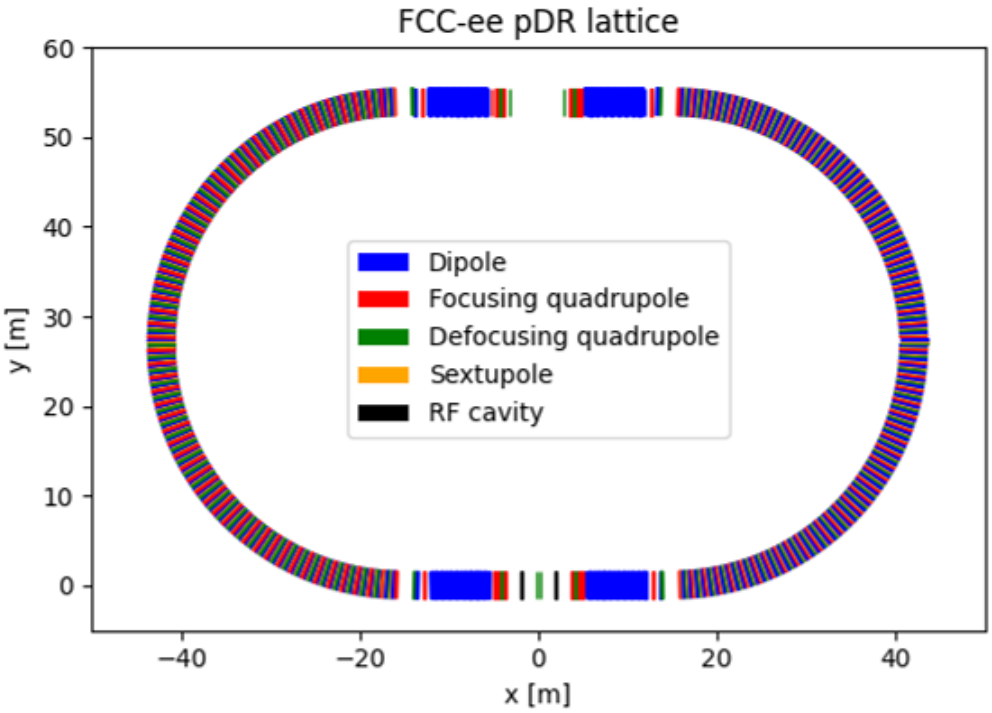

Figure 3.2: PDR lattice, with colour-coded labels for each magnet type. Note that the wigglers are indicated by the four long blue sections with many dipoles. The kicker and septum will be located in the gap at the top centre of the lattice ring.

Each magnet serves a different purpose:

- Dipoles: These are used to create a uniform magnetic field. By the Lorentz force law, such a field will bend charged particles around the ring.
- Quadrupoles: These are used to focus the particle beam. A single quadrupole can only focus in one plane, i.e. it will focus in the horizontal plane while simultaneously defocusing in the vertical plane (or vice versa). However, the overall effect of an alternating series of focusing and defocusing quadrupoles is to focus the beam.
- Sextupoles: These are used to correct chromaticity. The nonlinear magnetic fields force the momenta of off-orbit particles closer to the momentum of the reference particle [21].

- Wiggler: A wiggler magnet is a row of dipoles with alternating field directions. This orientation forces the beam to oscillate in the transverse plane as it travels longitudinally. Charged particles will then emit synchrotron radiation, damping the emittance of the beam. These wigglers are the lattice element that allows the pDR to fulfil its purpose.
- Kicker and septum: These are used in conjunction with each other as part of the injection/extraction process into a beamline. In injection the septum deflects the beam onto the closed orbit at the centre of the kicker, then the kicker compensates for the remaining angle. For extraction, the kicker first deflects the entire beam into the septum. After that, the septum deflects the entire kicked beam into the transfer line.

3.1.2 Design Goals

Environmentally conscious design

Minimising environmental impact is a key design goal for the Future Circular Collider. As such, the design of the individual components must also follow this design philosophy. With that in mind, material properties and power usage have been key in deciding the types of magnets, and optimising for performance. A more full discussion on which magnet technologies and materials are chosen is found in Section 3.1.7.

Aperture region

For the analysis carried out for the pDR, the beam-pipe was modelled as a circular cross section, 50 mm diameter, stainless steel tube. This geometry and size is in line with other CERN beam-pipe sizes, and still offers enough space at this high emittance point in the accelerator chain. Currently deployed magnets have used the following beam-pipe sizes [21]:

- CERN LHC dipole: 56 mm diameter circular aperture.
- CERN SPS dipoles: 39 mm and 52 mm vertical apertures.
- CERN LHC quadrupole: 56 mm diameter circular aperture.
- CERN SPS quadrupole: 88 mm diameter circular aperture.
- ELETTRA combined function bending magnet: 70 mm vertical central gap.

As such, a circular diameter of 50 mm is on the low end, but in line with the above.

See Section 3.1.5 for a discussion of the Good Field Region (GFR), which is the key performance metric for the magneto-static analysis discussed in this chapter.

Single design per magnet type

The proposed lattice for the pDR has requirements for multiple designs of quadrupole ($n = 10$) and sextupole ($n = 2$). Creating entirely different designs for each of these would be costly, and increase the difficulty of replacement and maintenance due to the increased number of different components. As such, it is preferred to have a single design for each, that operates with high performance in all regimes, and where the designed field gradient and second derivative (for quadrupoles and sextupoles respectively) is controlled by adjusting the current provided to the magnet.

Saturation

In general, magnetic materials do not exhibit a linear relationship between the applied current and the magnetic field produced by an electromagnet. In an unsaturated design, far from saturation magnetisation, there is a direct proportion between these values. This linearity makes tuning the magnets easier, so ideally the magnets would operate significantly below saturation.

Whilst the dipoles, quadrupoles, sextupoles and wiggler are all fixed magnets, saturation is particularly important for the kicker/septum where the ramping is highly important. Ramping power supplies linearly is preferred to ramping non-linearly, so ensuring that all fields are far from saturation is a priority.

3.1.3 Design parameters

The parameters are constrained by lattice requirements such as beam energy and emittance in the rest of the FCCee complex. As in Chapter 2.1, we took an input beam energy of 1.54 GeV for the pDR. In order to get the desired emittance damping, we designed magnets with the same length and bending angles as in the provided in a file already written for use in Methodical Accelerator Design software, (MAD-X) [22] [17].

After running the MAD-X file, we extracted the parameters shown in Table 3.1. Note that the values for the wiggler are those for one constituent dipole in the wiggler.

Dipole (B1)	Length (m)	Angle (°)	Energy (GeV)	Rigidity (T · m)	B-field (T)
	0.2100	0.0271	1.54	2.1660	0.0595
Quadrupole (QFH)	Length (m)	K_1 (m^{-2})	Energy (GeV)	Rigidity (T · m)	G (T/m)
	0.1000	8.0515	1.54	2.1660	3.7172
Sextupole (SD)	Length (m)	K_2 (m^{-3})	Energy (GeV)	Rigidity (T · m)	B/R^2 (T/m^2)
	0.0800	-686.7417	1.54	2.1660	-743.7415
Wiggler Dipole (B2)	Length (m)	Angle (°)	Energy (GeV)	Rigidity (T · m)	B-field (T)
	0.0500	0.0175	1.54	2.1660	0.1616

Table 3.1: Magnet parameters from MAD-X file. K_1 and K_2 are the quadrupole strengths. G is the field gradient of the quadrupole.

The length, angle and quadrupole strengths came directly from the MAD-X output. However, the rigidity, B-field, and its derivatives had to be calculated using the following formulae [21],

$$\text{Rigidity} = B\rho = \frac{10^9}{c \cdot pC[\text{GeV}]} \tag{3.1}$$

$$B = \frac{\left|\text{Angle}[^\circ]\right| \cdot B\rho}{L} \tag{3.2}$$

$$G = \left|K_1\right| \cdot B\rho \tag{3.3}$$

$$\frac{\partial^2 B}{\partial r^2} = \frac{1}{2} K_2 \cdot B\rho \tag{3.4}$$

where PC is the product (in GeV) of the particle's momentum and the speed of light, ρ is the bending radius, and G is the field gradient.

3.1.4 Finite Element Magnetostatics Analysis

Finite element analysis

The key components of a finite element method for solution of a boundary-value problem are given by:

1. A variational (weak) statement of the problem,
2. The approximate solution of the variational equations through the use of finite element functions [23].

Finite Element Analysis is a method of solving differential equations (boundary value problems) numerically. The system being analysed is split into smaller pieces (finite elements) which are easier to solve. This splitting is done by creating a mesh of the object with a set finite number of points. The method approximates solutions in each element, then reassembles them into a solution for the whole system. The overall solution is then found by minimising the error function associated with the solution.

FEMM

FEMM is a suite of programs for analysis of low frequency electromagnetic problems [24].

For this magneto-statics analysis, three programs from FEMM's suite were employed: the interactive shell (femm.exe), the triangle mesh (triangle.exe) and the magnetostatics solver (fkern.exe).

FEMM provides analysis tools for low frequency electromagnetic problems on two-dimensional planar and axisymmetric domains. For 'low frequency' problems, displacement currents are ignored in magneto-statics solutions. Displacement currents are typically relevant to magnetics problems only at radio frequencies [25].

Data was read out from FEMM using pyFEMM, which allows for either point-wise or line-wise extraction of data.

All of the designs were constructed and analysed using FEMM version: 4.2. The latest stable distribution was used: build 21Apr2019.

A Python interface to FEMM, PyFEMM, was used for data analysis [26]. PyFEMM version 0.1.3 was used. The latest stable distribution was used: build 20Jul2021.

FEMM Magnetostatics Solver

All fields in magnetostatics problems are time invariant. As such, the field intensity, H, and flux density, B, are adequately described by,

$$\nabla \times H = J \tag{3.5}$$

$$\nabla \cdot B = 0 \tag{3.6}$$

where J is the current density. The field intensity and flux density are related by the material property of magnetic permeability,

$$B = \mu(B)\, H \tag{3.7}$$

where μ is the magnetic permeability. In general, the permeability is a non-linear function of magnetic field strength.

FEMM uses a magnetic vector potential analysis to solve both Eq. 3.5 and Eq. 3.6. The flux density can be expressed in terms of the vector potential as,

$$B = \nabla \times A. \tag{3.8}$$

As such, all conditions can be expressed in the single differential equation,

$$\nabla \times \left(\frac{1}{\mu(B)} \nabla \times A \right) = J \tag{3.9}$$

where A is generally a vector with three components. However, in the 2D planar and axisymmetric cases, two of these three components are zero, leaving just the component perpendicular to the plane.

Once A is calculated, B and H are found by differentiation.

FEMM Problem Definitions

For the analysis described in this section, the following problem definition was applied to all analyses:

Problem Definition Setting	Value
Problem Type	Planar
Length Units	Millimetres
Frequency (Hz)	0
Solver Precision	1e-008
Min Angle (deg)	30

Table 3.2: Problem definition settings used in FEMM analysis

3.1.5 Magnet performance evaluation

Good field region

The Good Field Region (GFR) of a magnet, is the on-axis region between the poles where the B-field or a relevant derivative is within a given tolerance of the target design value.

The relevant derivative and tolerance varies by magnet type. For the magnets considered in this report, these parameters are,

$$\left|\frac{\frac{\partial^n}{\partial x^n}\left(B_{\text{pole}} - B\right)}{\frac{\partial^n}{\partial x^n}B_{\text{pole}}}\right| \sim \begin{cases} 10^{-4},\ n = 0 \text{ for dipoles} \\ 10^{-3},\ n = 1 \text{ for quadrupoles} \\ 10^{-3},\ n = 2 \text{ for sextupoles} \\ 10^{-3},\ n = 0 \text{ for wiggler} \\ 10^{-1},\ n = 0 \text{ for kicker and septum.} \end{cases} \tag{3.10}$$

It is standard to aim for a good field region radius of at least two-thirds of the aperture diameter (diameter taken to be 50 mm). As such, in this case the target value will be a radial GFR of 16.67 mm.

Differentiation methods

As is shown in Eq. 3.10, the performance of the quadrupoles and sextupoles is dependant on a derivative of the magnetic field. As a finite element analysis has been used to calculate the vector potential, and in turn flux density, calculation of the derivatives of the magnetic field requires additional care. There is no functional form for the calculated field, and so there are different options for calculating the derivatives of the field, each with benefits and drawbacks.

Numerical differentiation

Numerical differentiation is the simplest approach to finding the derivative from the calculated B field. Numerical differentiation algorithms estimate the derivative of a function using values of the function. This implementation was handled using Numpy's gradient function, where: "The gradient is computed using second order accurate central differences in the interior points and either first or second order accurate one-sides (forward or backwards) differences at the boundaries" [27].

The biggest drawback of numerical differentiation is the difficulty of dealing with noise. Conventional finite-difference approximations greatly amplify noise present in the data and de-noising the data before or after differentiating does not generally give satisfactory results [28]. The more derivatives required, the greater the impact of this issue as demonstrated in Fig. 3.4. This can be mitigated in multiple ways, discussed below.

Filtered numerical differentiation

One method of reducing the impact of noise in the data, is applying a low-pass filter to the smooth the data. This method was chosen to preserve the slowly varying behaviour whilst eliminating high frequency oscillations. In this analysis, a Butterworth filter was implemented since it has a maximally flat frequency response in the passband [29]. The Bode plot in Fig. 3.3 shows this graphically, where f_c is the cut-off frequency. It also shows the phase shift as a function of frequency.

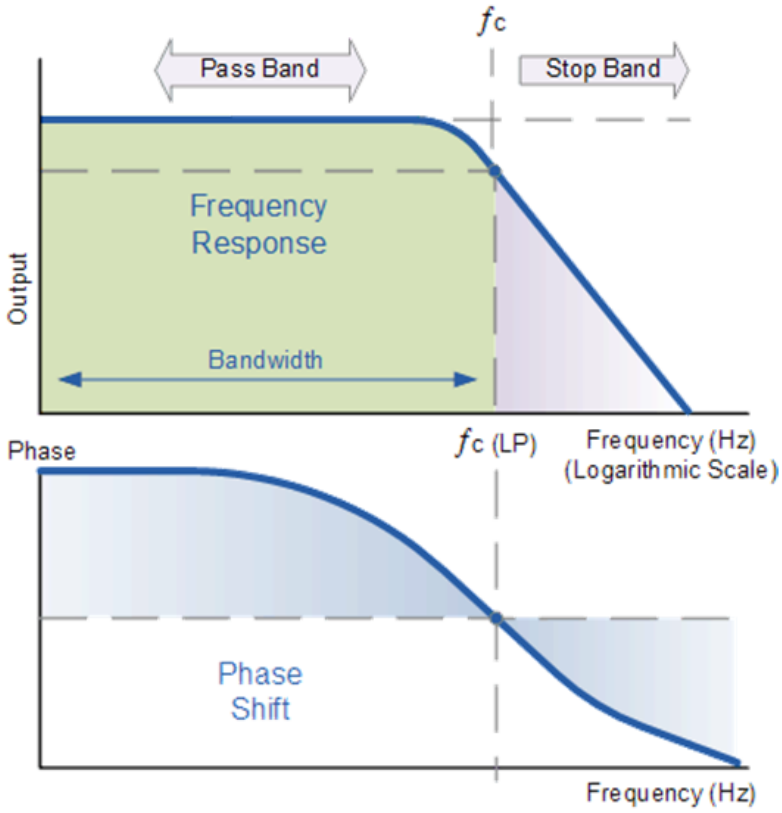

Figure 3.3: Bode plot for low-pass filter showing the cut-off frequency f_c and including the effects of the phase shift

The implementation of this filter was done using the builtin Butterworth filter in SciPy [30]. The variables outputted by this denote the numerator and denominator polynomials of the filter. These were used to further filter the array with Scipy's filtfilt package which applies a linear digital filter forward and backwards on the array which removes the non-linear phase-shift as a function of frequency introduced by the Butterworth filter [31].

Noisy data numerical differentiation using TVREGDIFF

To avoid de-noising the data before or after differentiating, an alternative method is to regularise the differentiation process itself. The computed derivative therefore has guaranteed regularity, to an extent that is under control by adjusting parameters [28].

For this analysis, the code tvregdiff (Python version of Rick Chartrand's algorithm for numerical differentiation of noisy data) was used [32]. This uses a total-variation regularisation (TVREG) method for calculating the derivatives, allowing for discontinuities. The TV regularisation allows the derivative to capture more features of the data, while adjusting the regularisation parameter controls the scale of fluctuations in the data that are ignored.

This has the benefit of a mathematically rigorous backing on the method of taking the derivative of noisy data, however introduces another degree of freedom in the analysis, in the form of the regularisation parameter. Furthermore, over large data sets this method is relatively computationally inefficient.

Polynomial fitting

As data is extracted point-wise or line-wise from FEMM, another option is to fit polynomial (or alternatively spline) curves to the data, and perform derivatives on these polynomials. The 2D array can then be built up from the different polynomial curves in x and y. The implementation of polynomial fitting is provided in Numpy's Polynomial package [27].

This is computationally efficient, however struggles when trying to fit to noise dominated data (as is the case in low field areas). Furthermore, another variable is introduced in the form of the degree of the polynomial to fit. Whilst the expected degree is low, this potentially over-smooths the problem, but using higher order polynomials can result in poorly matched behaviour at the boundaries of the sampled data.

3.1.6 Multipole expansion

The magnetic field can also be expressed in terms of a series of multipoles. For such an analysis, the 2D space is described as a series of scalar coefficients (harmonics/multipoles) denoted A_n, B_n. Such a decomposition holds in a region:

1. without currents

2. without (hard or soft) magnetic materials

3. where the z component (3^{rd} dimension, longitudinal) of B is constant.

This is well approximated within the beam-pipe region of a long magnet (and in this instance, where no out-of-plane magnetic fields are considered in the 2D analysis). The sums of the multipoles are given by,

$$B_r = \sum_{n=1}^{\infty} \left(\frac{r}{R}\right)^{n-1} \left[B_n \sin(n\theta) + A_n \cos(n\theta)\right] \tag{3.11}$$

$$B_\theta = \sum_{n=1}^{\infty} \left(\frac{r}{R}\right)^{n-1} \left[B_n \cos(n\theta) - A_n \sin(n\theta)\right] \tag{3.12}$$

where B_r and B_θ are the radial and angular components of the magnetic field strength, R is the reference radius for evaluation, A_n are the skew multipole components and B_n are the normal multipole components.

From the above, a description of the B field can be constructed in complex form as follows:

$$B_y(z) + iB_x(z) = \sum_{n=1}^{\infty} (B_n + iA_n) \left(\frac{z}{R}\right)^{n-1} \quad z = x + iy = re^{i\theta}. \tag{3.13}$$

Such an expansion is computationally efficient to calculate, requiring sampling of points to extract the multi-pole coefficients. The derivatives can then be expressed analytically in terms of the extracted multi-pole components.

Furthermore, symmetry considerations allow for further reductions of the multi-pole components considered. The allowed/forbidden harmonics are the terms that won't or will cancel out due to symmetries present in the design of the magnet. For example, a fully symmetric sextupole has allowed harmonics: (A3, B3, A9, B9, A15, B15...) . All other harmonics are not allowed by symmetries.

Due to the inefficiency of extracting individual point values in pyFEMM, this method becomes inefficient when a high number of sample points are considered.

Choice of Methodology

For analysis of the dipoles and wiggler, no differentiation was required.

For the quadrupole, numerical differentiation was attempted, but noise propagation from the Finite Element Analysis proved to be overwhelming and multipole analysis was employed.

For the sextupole, numerical differentiation was attempted. For computational ease, TVREGDIFF was used when performing sensitivity tests and initial optimisation, while a multipole expansion was used for analysis of the good field region.

For analysis of the kicker and septum, numerical differentiation was used, and filtered numerical differentiation was used, using the Butterworth filter method described above.

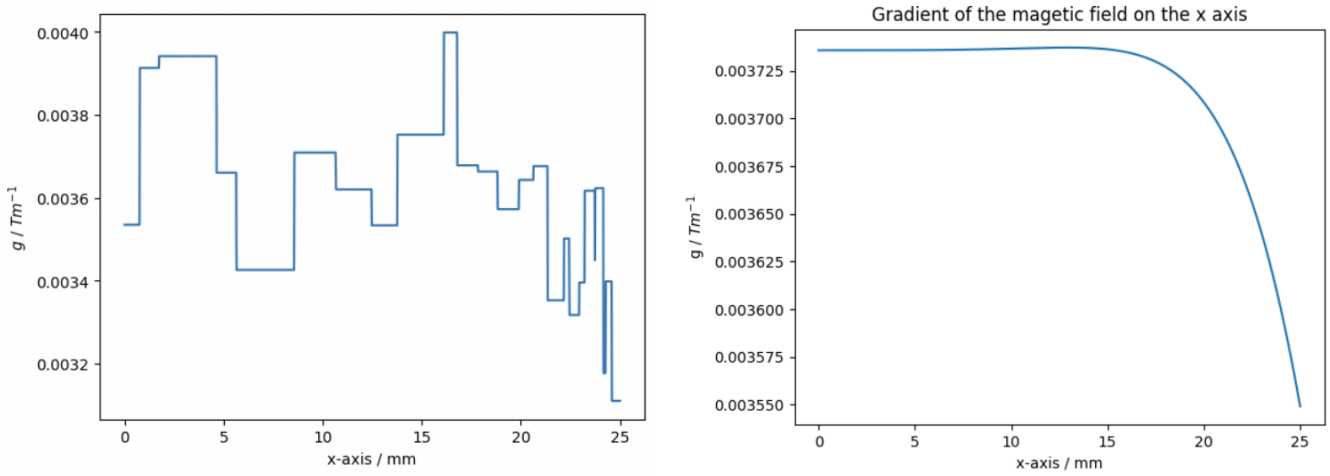

Figure 3.4: A comparison of noise for the gradient of the magnetic field calculated in a quadrupole, shown left: calculated with numerical differentiation, right: calculated with a multipole expansion.

3.1.7 Magnet Technologies and Material Choices

Permanent magnets

Permanent magnets are made from materials that, once magnetised, hold persistent magnetic fields. These magnets are made from 'hard' ferromagnetic materials. Common examples of permanent magnetic materials are Alnico, ferrite or neodymium. Manufacture of permanent magnets requires processing inside strong magnetic fields during manufacture, such that the internal crystalline structure aligns to create the magnetic field.

Hard magnetic fields have high coercivity, and as such it takes a high threshold field to demagnetise the material. In this way, the magnets retain their field. However, over time, with temperature and radiation exposure, the field degrades.

Whilst manufacture of highly accurate permanent magnets can be expensive, there are great gains in the lack of running costs, as no electromagnetic coils (or associated cooling) is required.

New research has resulted in permanent magnet technology that can be used to build compact

quadrupoles capable of providing a gradients up to 500 T/m [33]. However, there are downsides as the magnets are now no longer easily tuned to different field strengths. As such, different designs would be required for different magnets, or suitably different manufacturing that adds additional complexity. For the wiggler however, only one configuration of field strengths is needed, so permanent magnets could be suitable.

Electromagnets

Electromagnets are made when a current passing through a coil of wire induces a magnetic field. The magnetic field stops when the current stops. The coil is typically wrapped around a core of a soft ferromagnetic material in order to enhance the magnetic field. This comes at the cost of introducing additional time delay in turning on and off the field, i.e. a ramp or rise time.

The magnetic field is related to the current by Ampere's Law,

$$\nabla \times \mathbf{B} = \mu_0 \mathbf{J} \tag{3.14}$$

where μ_0 is the vacuum permeability constant. Electromagnets offer a key advantage over permanent magnets, as they can be tuned. The magnetic field strength is controlled by the current in the conducting coils. As such, one magnet design may be used with different currents to achieve multiple different magnetic fields.

Normal Conducting Electromagnets

Normal conducting electromagnets operate in temperature ranges such that the wires remain normally conducting. As such, there is no need for cryocooling. However, as the coils remain resisting, the currents used to generate the magnetic fields are limited by Joule heating. Magnet coils must be cooled, and for high current magnets this is typically done using water channels.

Limitations on peak current due to heating results in limitations on the field strengths produced by normal conducting electromagnets. As such, for the highest strength magnets, superconducting magnets are required.

Superconducting Electromagnets

Superconducting magnets are electromagnets made with coils of superconducting wire. A superconductor has a critical temperature, below which the electrical resistance drops to zero, and

magnetic flux fields are expelled from the material. As there is no resistance, much larger currents can be conducted than in normal conducting wire. As such, more intense magnetic fields can be generated. Superconducting magnets offer the highest available magnetic fields and are used in many different commercial applications. Superconducting magnets are also used for the dipoles, quadrupoles and sextupoles at the LHC.

Superconducting magnets come with the downside that the material must be kept below the critical temperature to avoid quenching. A quench occurs when part of the superconducting coil is heated to above the critical temperature, becomes normal conducting, and results in rapid Joule heating from the high current. This raises the temperature in the surrounding area and results in the entire magnet rapidly becoming normal conducting and the energy of the magnetic field being converted to heat. This can result in permanent damage to the magnet, as occurred at the LHC in 2008, requiring replacement of some magnets [34]. As such, a cryocooling setup is required, which can be costly. Current LHC magnets require liquid helium cooling.

Choice of magnet technology

Throughout this analysis, two different magnet technologies have been considered. Both permanent magnets, and normal conducting electromagnets have been considered for applications in the pDR. Superconducting Electromagnets have been excluded, due to the requirement for cryocooling apparatus. The greatest benefit of superconducting electromagnets is the high field strengths possible, however this is not a requirement of the pDR.

There are 5 types of magnet considered throughout this analysis, and the choice for technology in each is discussed below.

The typical lattice magnets (dipoles, quadrupoles and sextupoles) were all modelled as normal conducting electromagnets. This decision was twofold:

1. Multiple designs of quadrupole ($n = 10$) and sextupole ($n = 2$) were required by the lattice design for the pDR. As such, creating one design and optimising for different uses by adjusting current was preferred
2. Significant work on normal conducting electromagnets for FCC-ee has been performed [22]. As such, aligning with this, both in material use and design philosophy seems the optimal solution

The kicker/septum requires the use of an electromagnet in order to only kick the beams into and out of the pDR at certain times. As such the choice was between normal and superconducting

electromagnets. Due to the low field strength required, the normal conducting electromagnet was chosen.

For the wiggler, both permanent and normal conducting magnets have been considered.

Material Choices

A full discussion of material choices goes beyond the scope of this report. A full analysis of material choices, requires more than just the analysis for magnetic performance, but would require a full cost and mechanical analysis also.

For the purposes of this analysis, materials used were those included in FEMM's materials library. Those were: Air, Pure Iron, Copper, 316 Stainless Steel, Y30 (ferrite) and 1020 Steel. The properties of these materials are given in Table 3.3 and the magnetisation curves of the non-linear materials are shown in Fig. 3.5.

Material	Relative Permeability	Electrical Conductivity [MS/m]	Linear
Air	1	0	Yes
Copper	1	58	Yes
316 Stainless Steel	1	1.334	Yes
Pure Iron	14872	10.44	No
1020 Steel	760	5.8	No
Y30 Ferrite	1	0	No

Table 3.3: Magnetic parameters for materials used in FEMM simulations, taken from the FEMM materials library

Normal Conducting Electromagnet Coils

As discussed above, one key consideration when designing electromagnets is the electromagnetic coils. This report does not include a thermal analysis, and as such a full analysis of the coil requirements is not possible. As such, caution has been taken to ensure the coils remain of reasonable finite size when modelling, and that currents are kept as low as possible whilst still achieving the target fields.

Coils have been modelled as bulk pieces, with a number of coils prescribed by FEMM. For iron dominated coils, there is no need to model individual coils, nor the detailed geometry of the

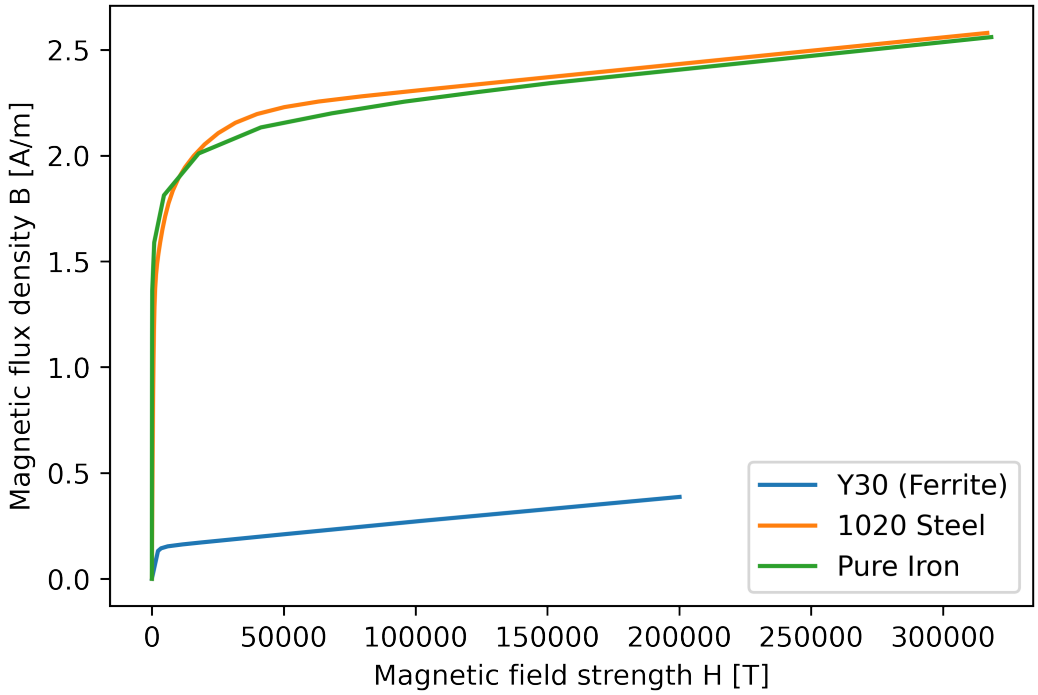

Figure 3.5: Magnetisation curves for non-linear magnetic materials used in FEMM: Y30 (Ferrite), 1020 Steel and Pure Iron

conductor, including the cooling holes. This is because the additional geometry modelled requires the creation of fine mesh around these edges which can result in incorrect calculations.

Common sizes of conductors are standard in the industry. and To minimise cost, using a standard size would be preferred. Common sizes are shown on manufacturer websites, for example the hollow conductors offered by Luvata [35]

3.2 Dipoles

Given the MADX parameters (Table 3.1), it was necessary to design a dipole with a pole tip magnetic field of 0.0595 T and a central gap of 50 mm. Given that the field magnitude was not very high, the design choice was a resistive electromagnet (non-superconducting). The design presented in this report is based on the JAI magnets tutorial example file, which is itself based on the dipoles used in the HIE-ISOLDE accelerator [36].

A C-type electromagnet was chosen as the design. The reasoning was that if sufficient field uniformity could be achieved with a C-type electromagnet, material could be saved relative to an O-type electromagnet. The materials used in the design were:

- Pure iron for the yoke, nonlinear B-H curve, electrical conductivity of 10.44 MS/m
- Copper for the coils, linear B-H curve, electrical conductivity of 58 MS/m.

The cross-section of the design is presented in Fig. 3.6.

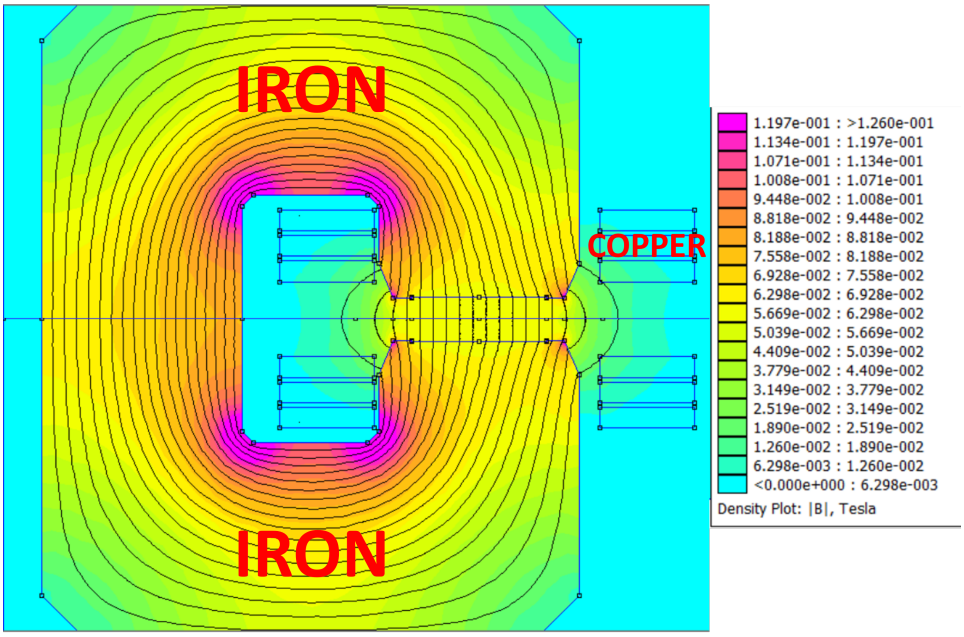

Figure 3.6: Cross-section of a potential dipole design for the FCC-ee pDR.

First, the two halves of the dipole were elongated away from each other to increase the gap to 50 mm. Next, chamfers were introduced at the inner corners of the yoke (purple regions) to smooth the B-fields around the corners. As shown by the legend, the maximum B-field magnitudes are less than 0.15 T, so overall the dipole is far from saturation. Finally, it was noted that the required on-axis B-fields (0.0595 T) were a lot lower than those in the JAI example. To reduce the B-field in the design, keeping the number of turns per coil constant and reducing the current in each coil was prioritised, rather than keeping the current constant and reducing the number of turns per coil. Whereas constructing the coils is a one-time investment, running a high current through them must be maintained over many years. Thus, the choice will reduce overall cost and energy consumption. The electromagnet has 18 turns per coil (139 mm^2/turn) and a current of 21.986 A.

The B-field along the middle axis of the gap was extracted using one of the FEMM features. This is shown in Figure 3.7:

The B-field looks very uniform everywhere throughout the gap except for the extreme edges. To quantify the field uniformity, the on-axis field's fractional difference relative to the desired pole tip field (Eqn. 3.10) was plotted. This plot is shown in Fig. 3.8. The orange line in Fig. 3.8 shows

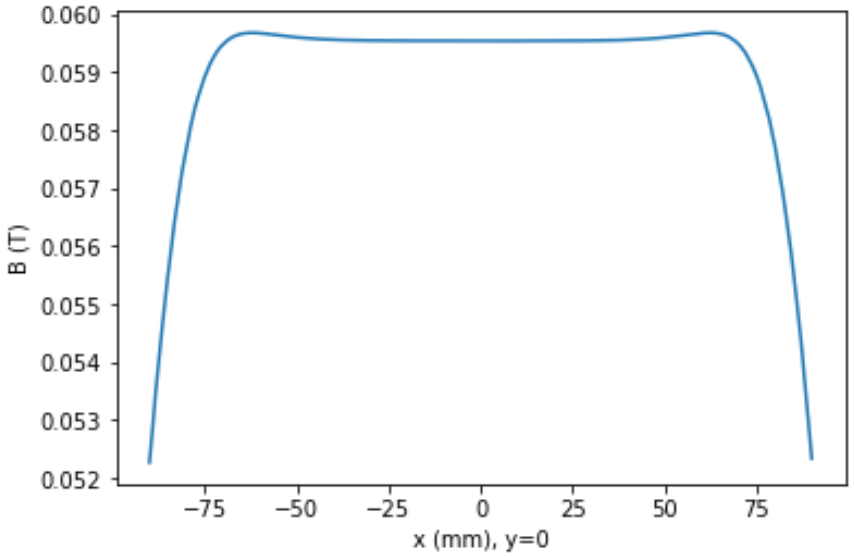

Figure 3.7: B-field of dipole along middle axis between the poles.

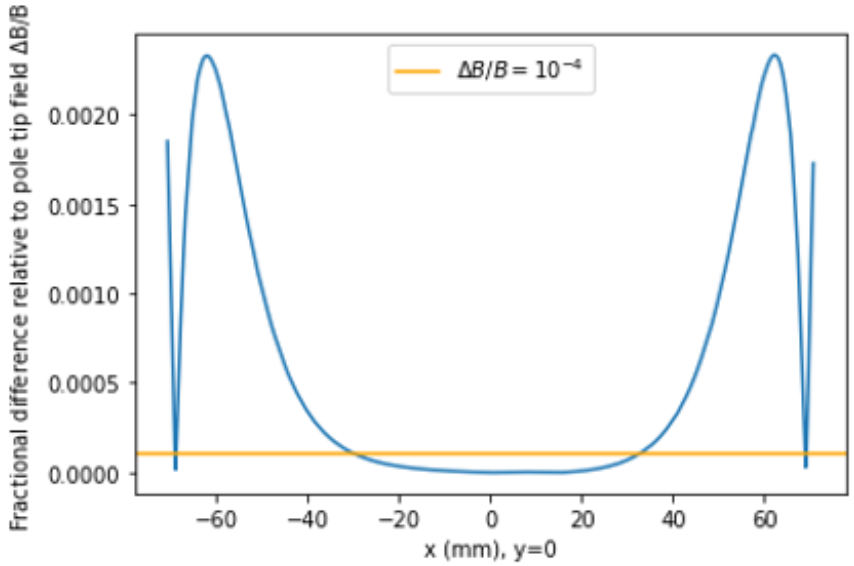

Figure 3.8: Fractional difference of B-field along middle axis relative to desired pole tip field.

where the fractional difference is 10^{-4}. As can be seen in the figure, the central region where the fractional difference curve dips below the line spans roughly 60 mm, which is greater than the beam-pipe diameter. Hence, this dipole design easily achieves the desired B= 0.0595 T with a GFR significantly exceeding the minimum requirement from Section 3.1.5.

3.3 Quadrupoles

3.3.1 Introduction

Dispersion is created when off momentum particles enter a bending element. This is compensated for by focusing the beam with a quadrupole magnet. The field in a quadrupole magnet is proportional to the radius, therefore focusing the off-orbit particles back to the reference trajectory [37].

The field of a quadrupole magnet is given by:

$$B_y = -g \cdot x, \quad B_x = -g \cdot y \quad \text{with} \quad g = -\frac{\partial B_y}{\partial x} = -\frac{\partial B_x}{\partial y} = \text{ const} \tag{3.15}$$

Quadrupole configurations

The key design parameters are given in Table 3.4.

Name	Length [mm]	K1	Energy [GeV]	Magnetic Rigidity	$\partial B/\partial r$ [T/m]
QRD	100	-0.0014	1.54	2.166	0.0006
QRF	100	4.4480	1.54	2.166	2.0536
QTD	100	-5.4389	1.54	2.166	2.5110
QTF	100	0.1342	1.54	2.166	0.0618
QTFD	150	1.0811	1.54	2.166	0.4991
QTFF	150	4.3436	1.54	2.166	2.0053
QSD	200	-4.8186	1.54	2.166	2.2247
QSF	200	6.2644	1.54	2.166	2.8921
QFH	100	8.0516	1.54	2.166	3.7173
QD	200	-7.8477	1.54	2.166	3.6231

Table 3.4: Quadrupole design parameters taken from pDR MAD-X file.

The quadrupole strength is given by,

$$K1 = \frac{q}{\rho} G, \quad [K1] = \text{m}^{-2} \tag{3.16}$$

where q is particle charge, ρ is the radius of curvature and G is field gradient. A focusing quadrupole has a negative K1 value; it focuses horizontally and defocuses vertically. A defocusing quadrupole

has a positive K1 value; it defocuses horizontally and focuses vertically. The following section will present the design of the magnet which has the highest field gradient (QFH in Table. 3.4).

3.3.2 Design

The ideal pole for quadrupole is a line of constant scalar potential defined by the aperture a,

$$y(x) = \pm\frac{a^2}{2x}. \tag{3.17}$$

In reality, the poles cannot extend to infinity and need to be terminated. However, with appropriate shimming the field quality will not be compromised.

The cross-section of the design for the QFH magnet is presented in Fig. 3.9. Shimming was added

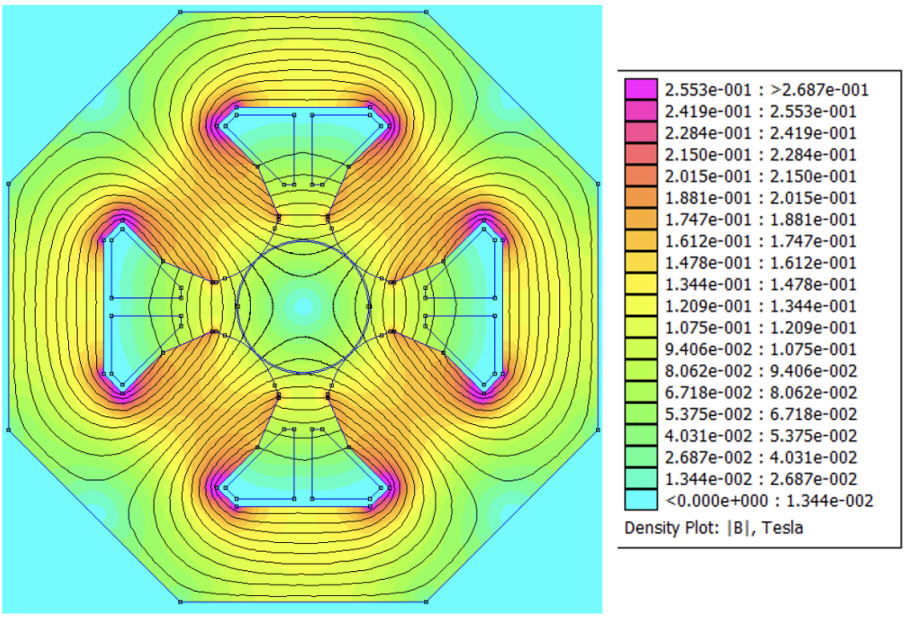

Figure 3.9: Cross-section of a potential quadrupole for the FCC-ee pDR.

to the pole tips to improve the field quality to a sufficient level, as demonstrated in Fig. 3.10. As shown by the legend, the maximum B-field magnitudes are less than 0.26 T which is below saturation. The magnetic gradient can be adjusted by varying the current and since the QFD magnet has the highest gradient, the magnetic fields in all other quadrupoles are also below saturation.

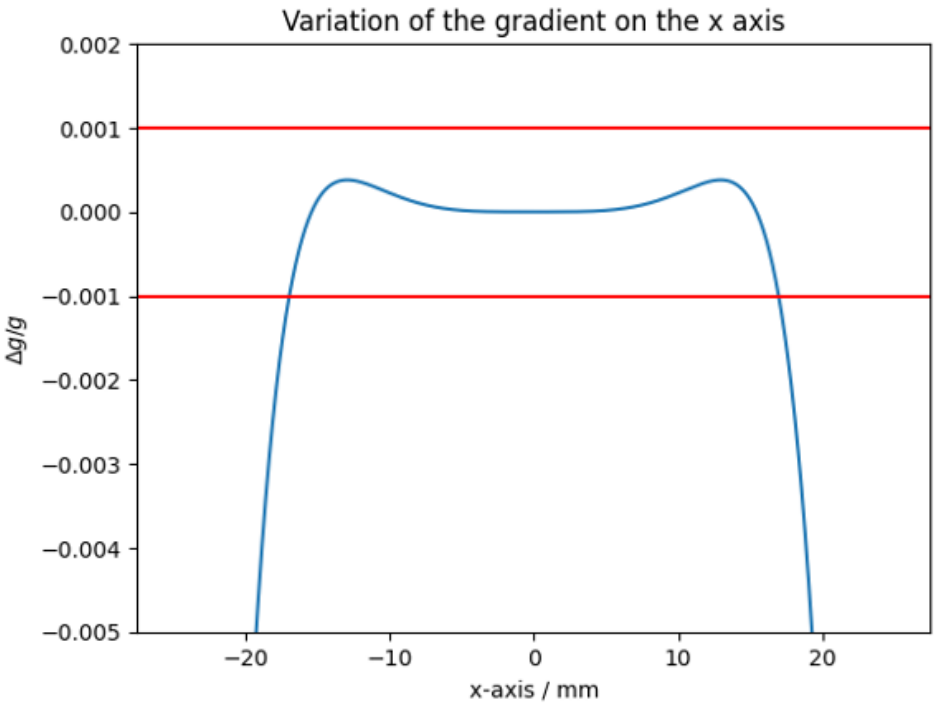

Figure 3.10: Fractional difference of the gradient of the magnetic field along the x axis.

Result

The gradient of the magnetic field was calculated by differentiating Eq. 3.13, with only (B2, A2, B6, A6, B10, A10 ...) allowed by symmetry. The change in gradient, as given in Eq. 3.10, is then calculated and plotted in Fig. 3.10. The red line shows where the fractional difference is 10^{-3}. It can be seen that the good field region spans 16.97 mm radially, which is above the target value of 16.67 mm. Therefore, this particular design achieves the gradient of 3.7173 Tm^{-1} as required, with a sufficiently large good field region.

3.4 Sextupoles

3.4.1 Introduction

Sextupole magnets are used in an accelerator lattice to correct the chromaticity produced by the focusing elements [38]. The field in a sextupole is proportional to the square of the radius. As such, a sextupole acts like a quadrupole with a focusing strength proportional to the displacement of the closed orbit from the sextupole centre. Particles that are off momentum are therefore corrected towards the reference orbit.

The field of a sextupole magnet is given by

$$B_x = \frac{\partial B_y^2}{\partial x^2} xy \qquad B_y = \frac{1}{2}\frac{\partial B_y^2}{\partial x^2}\left(x^2 - y^2\right). \tag{3.18}$$

Focusing and defocusing sextupoles

The lattice for the pDR requires two different sextupoles: SF (horizontally focusing sextupole) and SD (horizontally defocusing sextupole). Figure 3.11 shows the difference in polarity configurations for focusing and defocusing sextupoles.

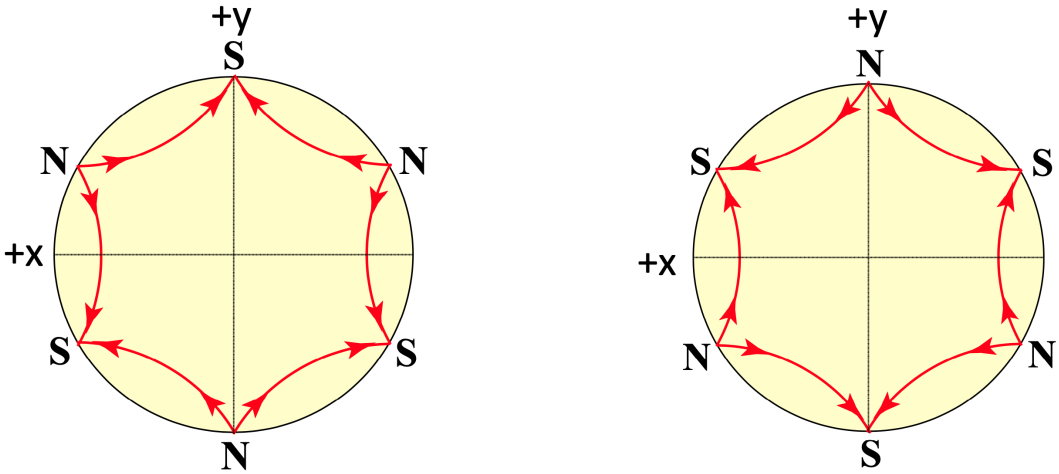

Figure 3.11: Pole configurations and magnetic field lines in (a) a focusing sextupole, and (b) a defocusing sextupole for an e– beam travelling in the positive z direction (into the page) [39].

From the MADX lattice, the key sextupole design parameters are given in Table 3.5.

Name	Length [mm]	K2 [m$^-$2]	Energy [GeV]	Magnetic Rigidity	$\partial B^2/\partial r^2$ [T/m^2]
SF	80	483.663	1.54	2.166	523.807
SD	80	-686.742	1.54	2.166	-743.741

Table 3.5: Sextupole design parameters from pDR MADX design. K2 is the sextupole strength.

3.4.2 Geometry

Tip Geometry

The ideal pole geometry for a sextupole is a line of constant scalar potential, where the flux lines flow perpendicularly to the poles. This idealised case would exist if the permeability of the pole was taken to infinity.

Specifically for a sextupole, this is a hyperbola given by (in polar and Cartesian coordinates),

$$r^3 \sin(3\theta) = \pm R^3 \qquad 3x^2y - y^3 = \pm R^3 \tag{3.19}$$

where R is the inner radius from the origin to the sextupole tip. A graphical representation of this is shown in 3.12.

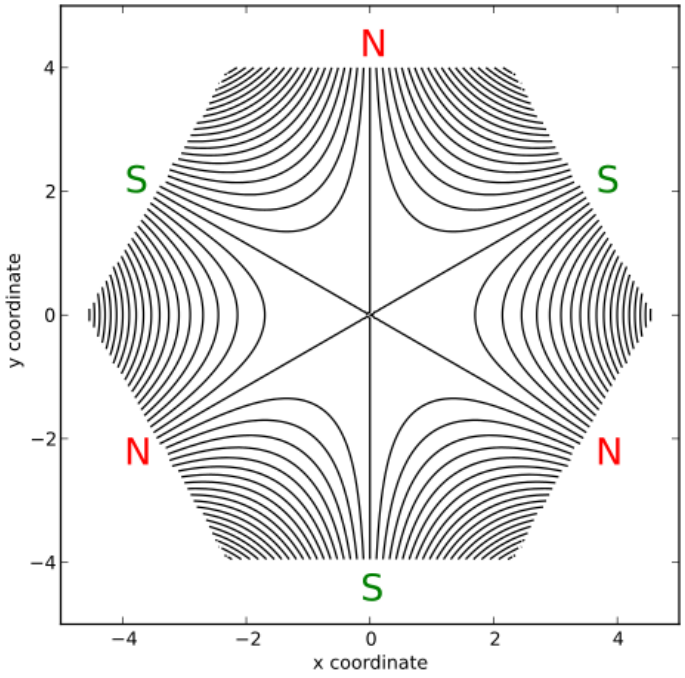

Figure 3.12: Magnetic field of an idealised sextupole [40].

Equation 3.19 gives the form of an ideal pole, with infinite width, and does not take into account the space required for any coils, cooling, or other structural elements. This is far from a realistic situation. An ideal hyperbolic segment for the pole tip provides a useful starting point. However, it is reasonable to move away from this if it is found to not be greatly detrimental to the field quality.

Though it has not been applied to the current proposed sextupole model, it is often preferential to deviate from the ideal profile when applying shimming, to deliberately enhance the field in edge regions. This increases the proportion of an aperture within the good field region.

Geometric Parameters

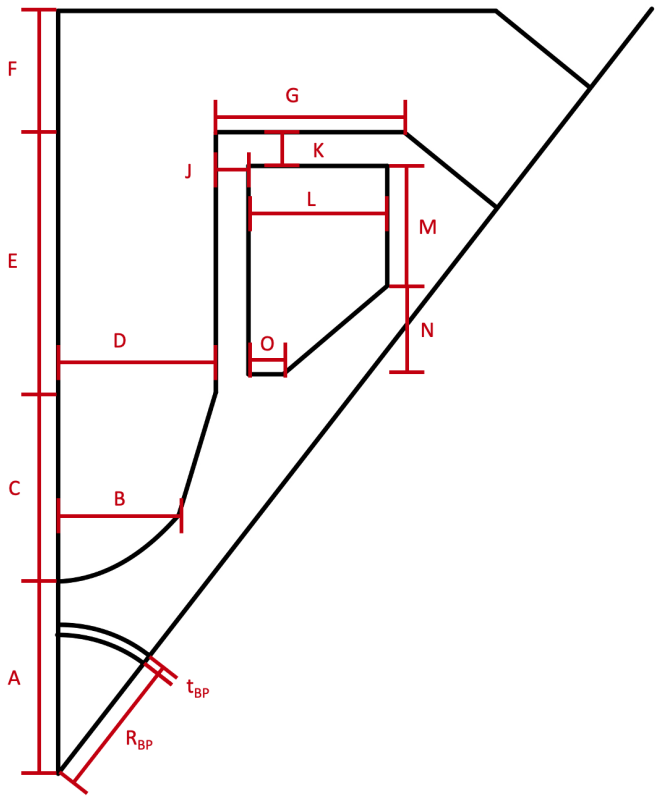

Figure 3.13: Geometric parameters considered in design of the pDR sextupole

The sextupole can be fully described by 15 geometric parameters (shown in Fig. 3.13):

- Yoke: 7 (A, B, C, D, E, F, G)
- Coil: 6 (J, K, L, M, N, O)
- Beam-pipe: 2 (R_{BP}, t_{BP}).

Of these parameters, the two beam-pipe parameters are considered to be fixed at 50 mm diameter and 1.5 mm thickness for this analysis.

3.5 Sensitivity Testing

In addition to the geometric variables discussed in Section 3.4.2, there are also the variables of number of coils, current, and the spacing of points along the hyperbolic tip of the magnet. As such, there are a total of 16 total parameters. This is excluding the possible additional considerations, such as material choices, choice of tip geometry, chamfering, shimming or any 3D considerations.

In order to reduce the scale of the problem, a sensitivity test was performed, to identify which parameters to optimise on.

The parameters searched over are given in Table 3.6.

Category	Parameter			
Yoke Geometry	A	B	C	D
	E	F	G	Tip Spacing
Coil Geometry	J	K	L	M
	N	O		
Coil & Current	Current		Number of Coils	

Table 3.6: Geometric parameters as shown in Fig. 3.13 and other sextupole parameters.

3.5.1 Sensitivity Test Methodology

For the sensitivity test, an initial sextupole design was created, with initial parameters set to fit appropriately with a sufficiently large copper coil for cooling. From this design, parameters were varied from 0.5 to 1.5 times the initial parameter value. In certain cases it was not possible to cover this full range, as to vary one parameter would cause the geometry to clash such that it is not a valid configuration. It is noted that each parameter was varied independently and the impact studied. With the 16 total parameters, variations across the whole parameter space go exponentially with the number of parameters and as such a scan of the full space was not plausible.

Evaluation of the field second derivative was performed using TVREGDIFF numerical differentiation (described in Section 3.1.5). For comparison, both the mean and standard deviation of the second derivative, within the inner 2/3 of the aperture were calculated. This was chosen, as the change in the mean gave an indication as to how much the value of the sextupole could be varied with a parameter, while the standard deviation gave a measure of the consistency of the field within the inner 2/3 of the aperture, i.e. the target good field area. Evaluating the good field

region directly would not be a useful metric while performing such a sensitivity test, as at values of field second derivative far from the target are zero and so do not show the variation.

Errors in the TVREGDIFF method were shown in this sensitivity test. Whilst the mean value showed good agreement with the mean value found using both polynomial and multipole expansions, the TVREGDIFF predictions show higher standard deviation due to the continued presence of the noise.

3.5.2 Sensitivity Test Insights

Results for the sensitivity test are shown in Appendix A.1.

There were a number of key insights to take from this sensitivity test:

1. The sextupole is most sensitive to variations in the number of coils and the current (in fact to the product of the two).
2. Very few parameters had a meaningful impact on the magneto-statics performance of the sextupole.

The parameters that had meaningful impact were: current, number of coils, A, B, D and the spacing of the hyperbolic tip.

As such, the number of parameters has been suitably reduced, and the sextupole design can be optimised.

It should be noted that this exclusion of these parameters is valid only in so far as an initial 2D magneto-statics evaluation. This parameter test has only shown the variation of the field second derivative with the parameters. The 'excluded' parameters may play a vital role in the costs, thermal performance or mechanical integrity of the sextupole. Furthermore, this sensitivity is only shown in 2D, where no edge effects are taken into account.

3.5.3 Optimisation

Optimisation was initially performed using a coarse optimisation algorithm, before manual tuning. Even after sensitivity testing, there were six remaining parameters of interest. As such, for fine adjustments, it was not possible to test variations of the combination of these. Rather, parameters

were varied individually. This was done in order for each parameter. The parameter that reduced the standard deviation the most, while approaching the mean, was chosen as the first parameter to vary. This process was repeated with the other parameters.

Following this coarse optimisation, some manual optimisations were performed. This reduced some of the sizes of other components, and ensured the coils fit sensibly. This was once again, only a magnetostatics optimisation. A more formal analysis would require other considerations.

Optimised parameters

The initial and final values for the sextupole parameters are given in Table 3.7. The final layout is shown in Fig. 3.14, showing the full geometry as modelled in FEMM.

Plots of the magnetic field strength, $|B|$, are shown for SF in Fig. 3.15 and for SD in Fig. 3.16. The fields show strong enhancement around the highly angular bases of the poles. Chamfering is required to reduce the high fields in these regions. SD reaches the saturation magnetisation of iron at these points, however as this magnet is fixed, this is not an issue for operation, and is a trade off of an increase in material for a decrease in saturation.

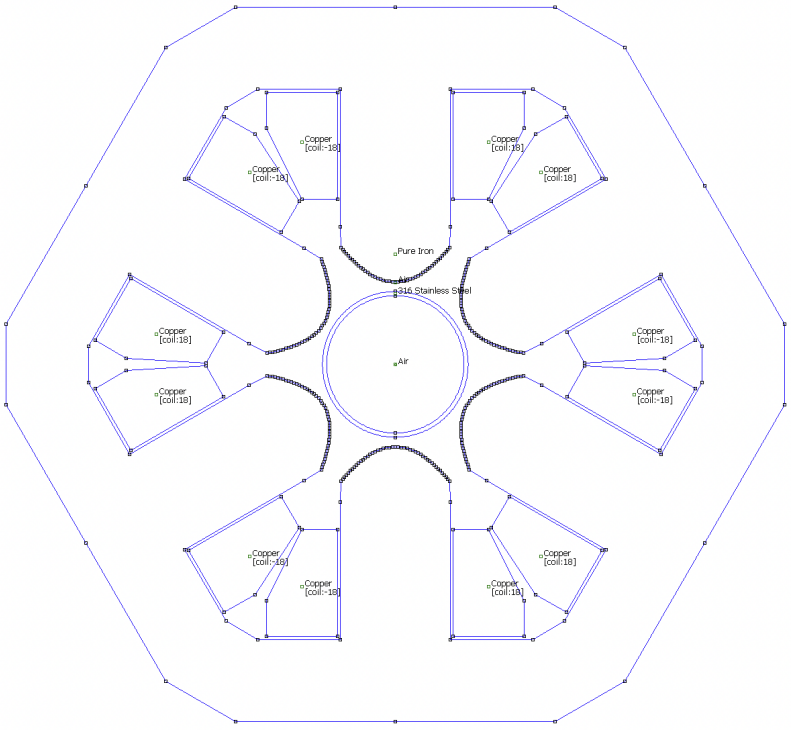

Figure 3.14: Sextupole design, as generated in FEMM

Parameter	Initial Value	Final Value	Units
Yoke Geometry Parameters			
A	30	30	mm
B	17	20	mm
C	30	20	mm
D	20	20	mm
E	50	50	mm
F	40	30	mm
G	40	30	mm
Tip Spacing	1	1	mm
Coil Geometry Parameters			
J	2	1	mm
K	2	1	mm
L	20	26	mm
M	20	13	mm
N	20	26	mm
O	10	13	mm
Coil Performance Parameters			
Number of Coils	18	18	
Current (SF)	115	104.66	A
Current (SD)	115	-148.72	A

Table 3.7: Initial and final design parameters for the proposed sextupoles SF and SD

Good Field Region Analysis

For analysis of the Good Field Region (GFR), a multipole analysis was used. This was performed both in 1D and in 2D. Due to the sextupole symmetry, the GFR was not a circular region, and as such there are different ways of considering the GFR:

1. Taking the minimum radius, such that all points within that radius satisfy the GFR.
2. Taking the mean radius, such that on average, a particle within that radius will satisfy the GFR.

Results with both considerations will be shown.

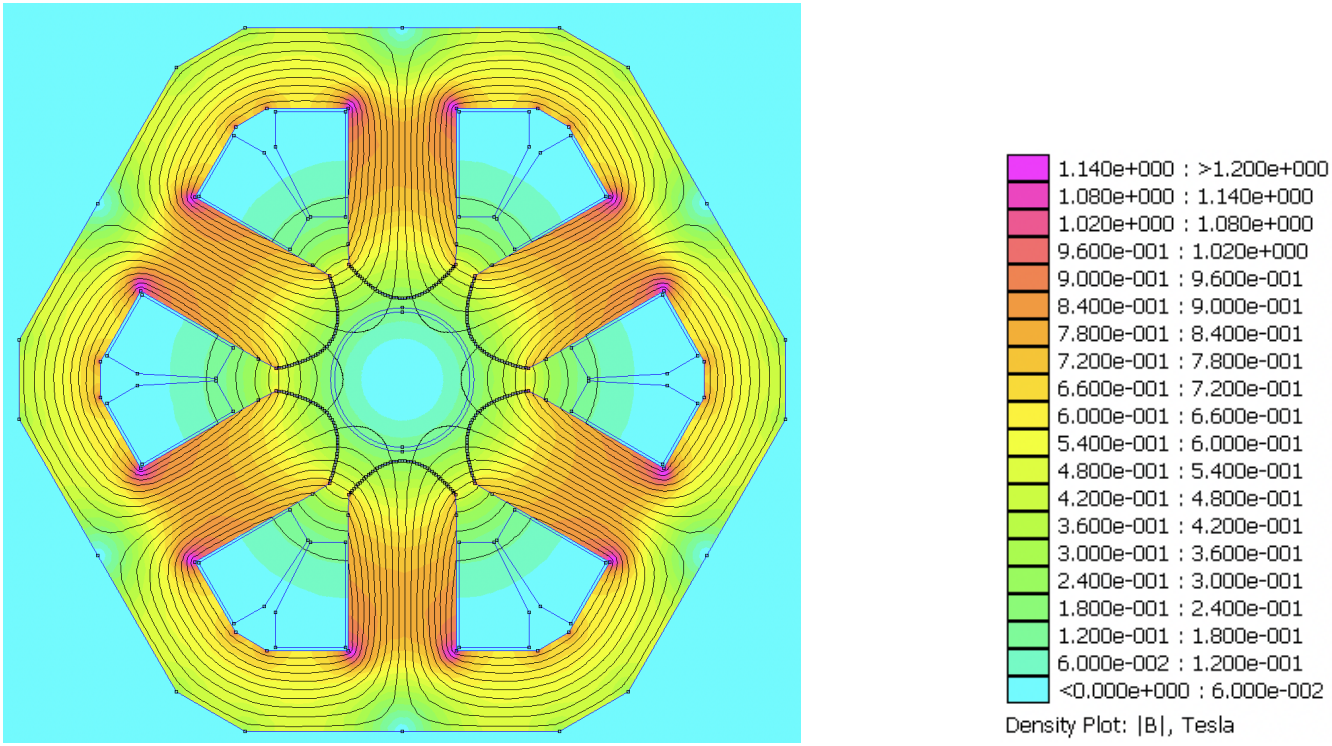

Figure 3.15: SF Sextupole magnetic field. Higher field strengths are observed around sharp corners, which can be reduced with chamfering. The field remains below saturation magnetisation.

When analysing the results in 2D, the calculated field strengths were enhanced by a factor of $\sqrt{2}$ compared to the raw field strengths calculated by FEMM. This does not align with the 1D analysis, so for results discussed below, this factor of $\sqrt{2}$ has been removed. The code used to perform the multipole analysis is found in Appendix A.2.

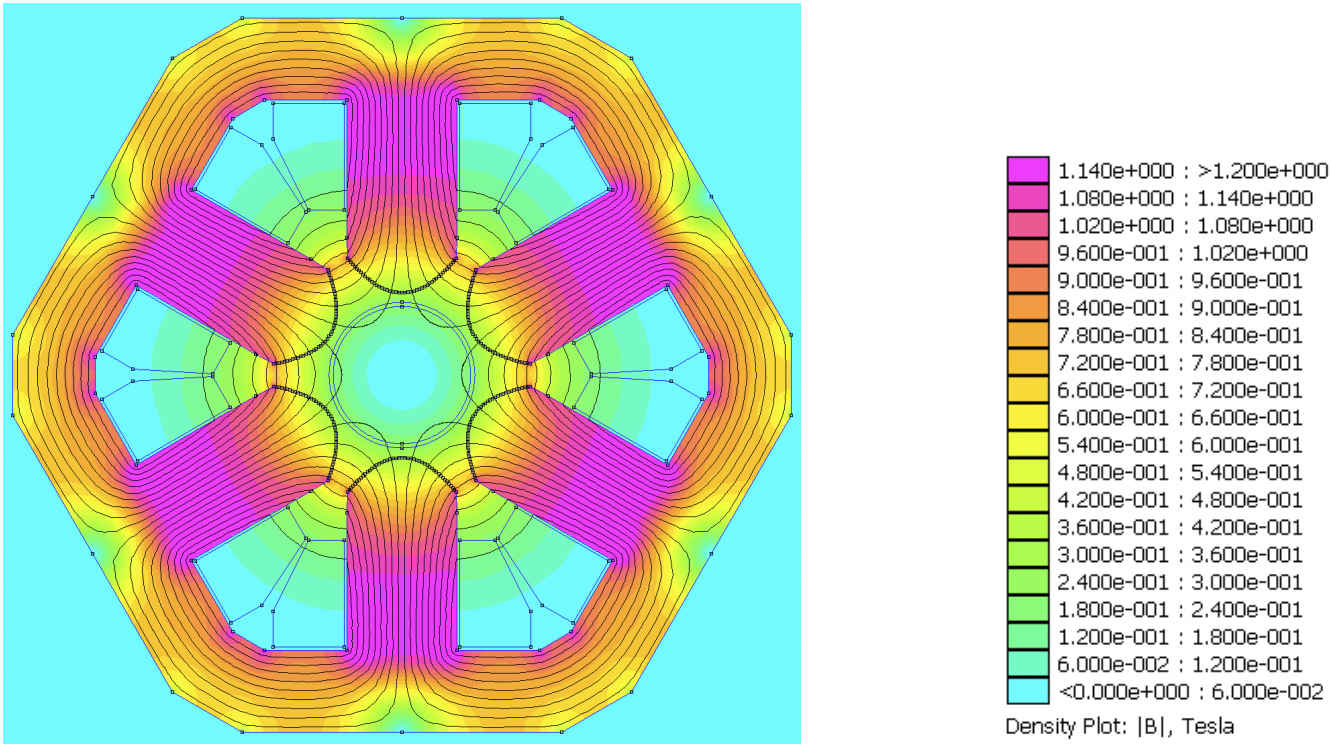

Figure 3.16: SD Sextupole magnetic field. Higher field strengths are observed around sharp corners, which can be reduced with chamfering. The field exceeds 1.2T within the iron yoke, and thus approaches saturation.

3.5.4 Performance

As with the quadrupole, the gradient of the magnetic field was calculated by differentiating Eq. 3.13 and considering only the symmetry-allowed modes. From this, the B field, its gradient and the second derivative are calculated. Along with this, the key metric is a good field region, which for the sextupole is the region where:

$$\left| \frac{\partial^2/\partial x^2 \left[B_{\text{pole}} - B \right]}{\partial^2/\partial x^2 \left[B_{\text{pole}} \right]} \right| \leq 10^{-3}. \tag{3.20}$$

For the analysis, 201 points were sampled at 0.95 $R_{\text{Beam Pipe}}$ for each set of multipole components (A_n: the skew components, and B_n: the normal components). The sampling code is shown in Appendix A.2.

Performance analysis was repeated twice. Two cases of multipole expansion were considered. One case considers only the fundamental mode and one higher order symmetry allowed mode (A3, B3, A9, B9). The other case considers the fundamental mode and ten higher order symmetry allowed modes (A3, B3, A9, B9, ..., A63, B63). Throughout, the two cases are shown side by side for comparison. Differences are addressed in Section 3.5.4.

Focusing Sextupole

For the focusing sextupole, the multipole coefficients extracted when considering only 2 harmonics (fundamental +1), were found to be the same as those when considering 11 harmonics (fundamental +10). SF multipole components are presented in Table. 3.8.

Plots of the second derivative of B vs position along the x or y axis in the beam-pipe are shown in Fig. 3.17. Plots of the calculated Good Field Region are shown in Fig. 3.18.

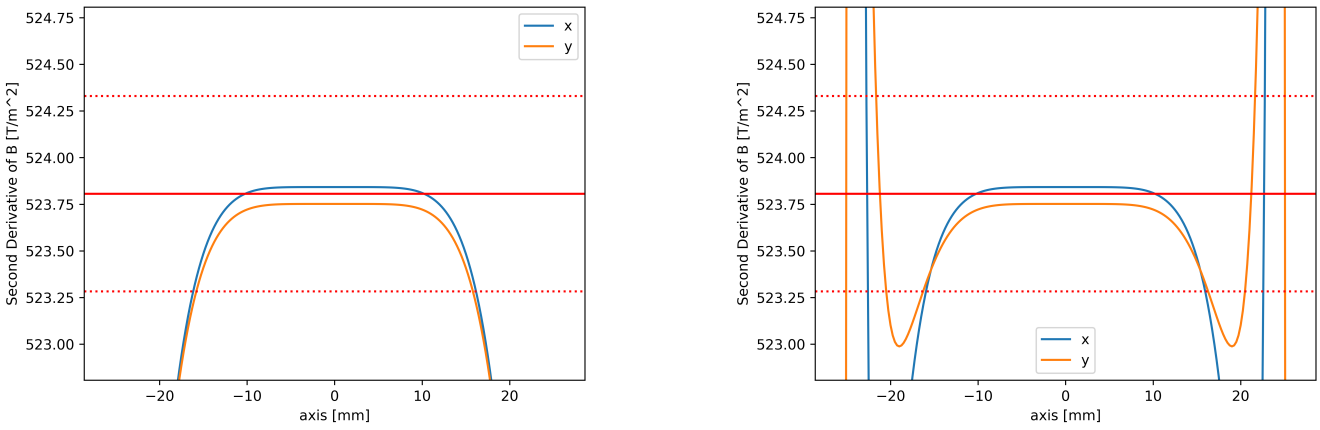

Figure 3.17: Plots of the second derivative of B vs position along the x or y axis in the beam-pipe for the Focusing Sextupole SF. Solid horizontal line shows the target, while dashed lines show the Good Field Region boundaries. Left: multipole prediction for fundamental mode (3) + 1 higher order symmetry allowed mode, Right: multipole prediction for fundamental mode (3) + 10 higher order symmetry allowed modes

Component	3	9	15	21	27	33	39	45	51	57	63
A_n ($\times 10^{-5}$)	16367.24	-8.22	5.04	2.42	1.19	-3.90	3.36	-0.32	1.18	-2.35	0.57
B_n ($\times 10^{-5}$)	16370.07	-8.58	-3.46	2.33	-0.08	5.63	-2.38	2.59	0.53	0.70	0.61

Table 3.8: Multipole coefficients for the Focusing Sextupole (SF), evaluated with the fundamental mode (3) and 10 higher order symmetry allowed modes.

The minimum radius which satisfies the GFR, taken from the 1D analysis, is 63.24% (or 16.81 mm). This is below the target value of 66.66%. When considering the 2D analysis instead, the average radius which satisfies the GFR, the 2D GFR area was 50.21%, corresponding to an average linear GFR of 70.86% (or 17.72 mm) which is above the target value of 66.66%. As such it is reasonable to conclude that the focusing sextupole has a sufficient good field region.

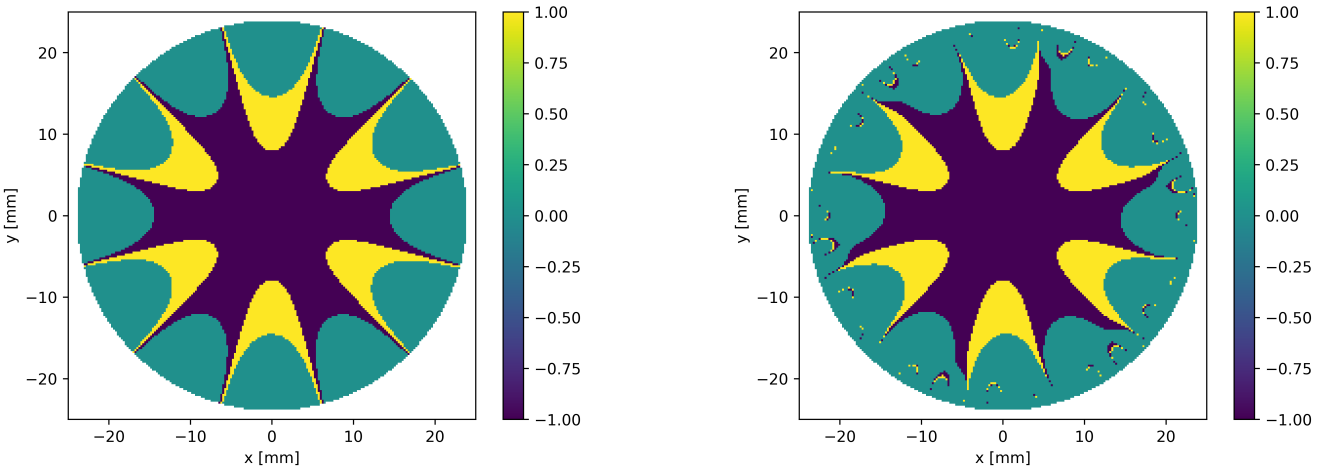

Figure 3.18: Plots of the Good Field Region within the beam-pipe for the Focusing Sextupole SF. Values of -1 indicate the area is within GFR limits, and below the target (shown in purple), values of +1 indicate the area is within GFR limits and above the target (shown in yellow). Left: multipole prediction for fundamental + 1 higher order mode, Right: multipole prediction for fundamental mode (3) + 10 higher order symmetry allowed modes

Defocusing Sextupole

For the defocusing sextupole, the multipole coefficients extracted when considering only 2 harmonics (fundamental +1), were found to be the same as those when considering 11 harmonics (fundamental +10). SF multipole components are presented in Table. 3.9.

Plots of the second derivative of B as a function of position along the x or y axis in the beam-pipe are shown in Fig. 3.19. Plots of the calculated Good Field Region are shown in Fig. 3.20.

Component	3	9	15	21	27	33	39	45	51	57	63
A_n ($\times 10^{-5}$)	-23239.09	11.63	-7.12	-3.48	-1.65	5.50	-4.73	0.42	-1.63	3.30	-0.77
B_n ($\times 10^{-5}$)	-23243.18	12.22	4.88	-3.27	0.07	-7.95	3.34	-3.64	-0.79	-0.94	-0.90

Table 3.9: Multipole Coefficients for the Defocusing Sextupole (SD), evaluated with the fundamental mode (3) and 10 higher order symmetry allowed modes

The minimum radius which satisfies the Good Field Region, taken from the 1D analysis, is 63.24% (or 16.81mm). This is below the target value of 66.66%, however is comparable. When considering instead, the average radius which satisfies the Good Field Region, the 2D GFR area was 50.12%, corresponding to an average linear Good Field Region of 70.80% (or 17.70mm) which is above the target value of 66.66%. As such it is reasonable to conclude that the focusing sextupole has a sufficient good field region.

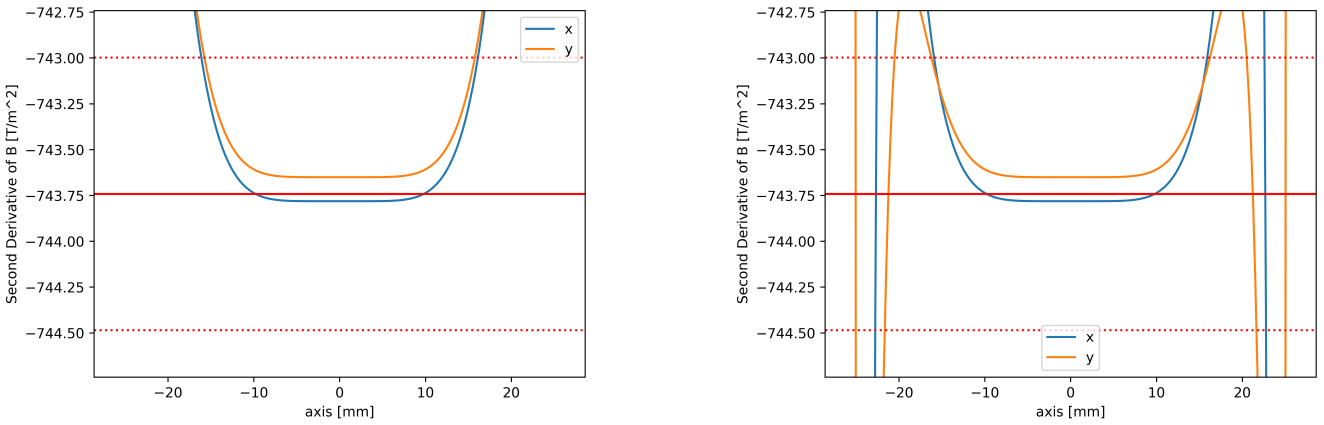

Figure 3.19: Plots of the second derivative of B as a function of position along the x or y axis in the beam-pipe for the defocusing sextupole. Solid horizontal line shows the target, while dashed lines show the GFR boundaries. Left: multipole prediction for fundamental mode (3) + 1 higher order symmetry allowed mode, Right: multipole prediction for fundamental mode (3) + 10 higher order symmetry allowed modes

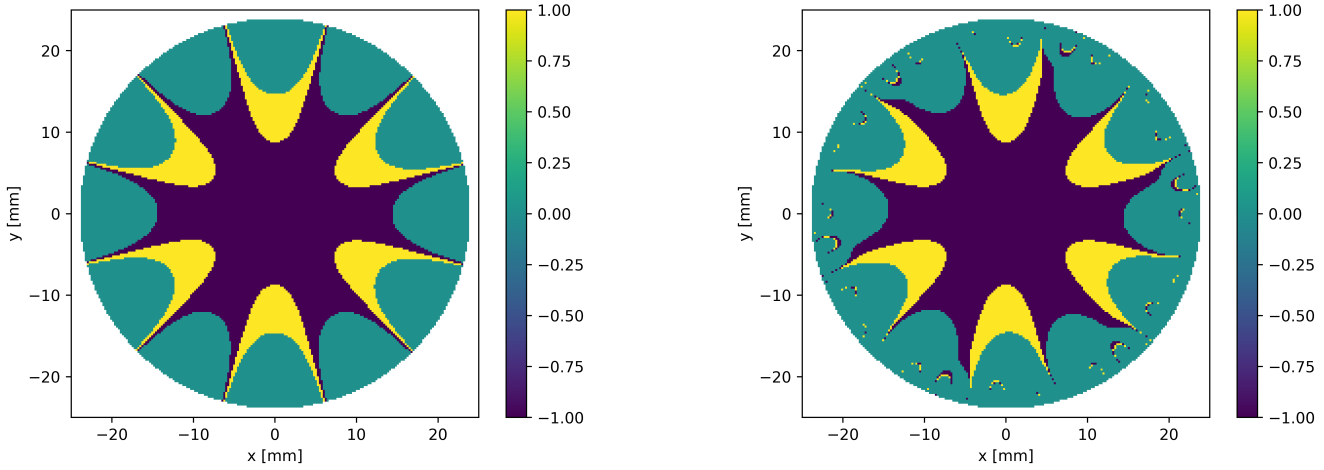

Figure 3.20: Plots of the Good Field Region within the beam-pipe for the defocusing sextupole. Values of -1 indicate the area is within GFR limits, and below the target (shown in purple). Values of +1 indicate the area is within GFR limits and above the target (shown in yellow). Left: multipole prediction for fundamental mode (3) + 1 higher order mode, Right: multipole prediction for fundamental mode (3) + 10 higher order symmetry allowed modes

Impact of higher order multipoles

Due to the sampling method (201 points were sampled at 0.95 $R_{\text{Beam Pipe}}$ for each set of multipole components), the results are only good estimates up to the sampling radius. At the beam-pipe radius, there is a change in materials (from vacuum to steel beampipe), which impacts the analysis.

Due to the power law nature of the higher order coefficients, when a large number of multipoles are considered, these dominate beyond the sampling radius. This is shown in Fig. 3.21. Differences in the scales shows that a higher order multipole expansion greatly impacts values beyond the sampling radius. Throughout, this effect has been impactful around the sampling radius (as demonstrated in Fig. 3.22). As the GFRs for the designed sextupoles are below this threshold, it is reasonable to consider the results with a finite (and small) number of harmonics.

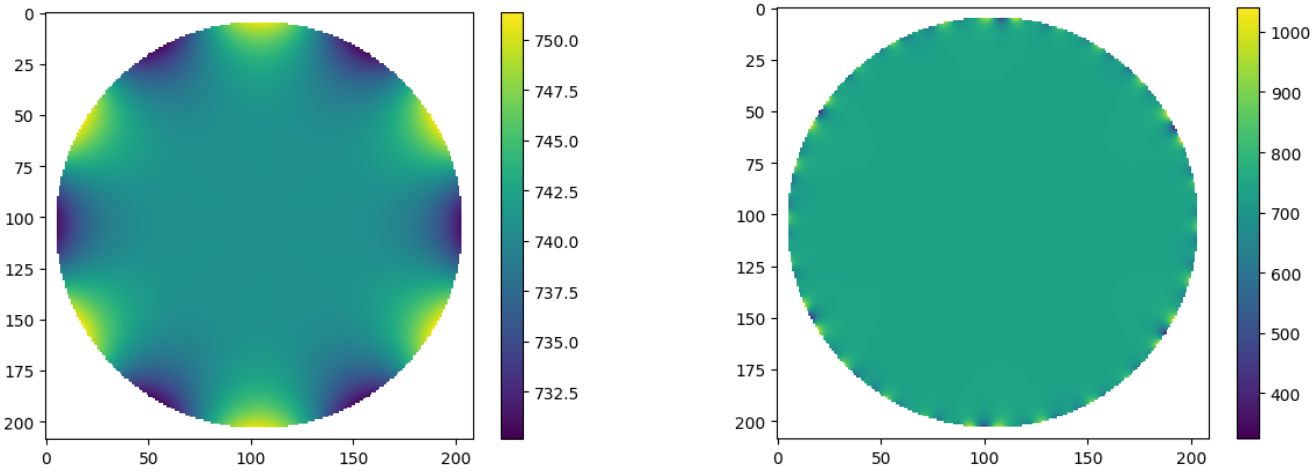

Figure 3.21: Effect of increased number of multipoles on field derivative predictions. Left: second derivative for SD, with 2 harmonics (fundamental +1). Right: second derivative for SD, with 11 harmonics (fundamental +10).

3.6 Kicker and Septum

As mentioned previously, kickers and septa are used in conjunction with each other as part of the injection/extraction process into an a beam-line.

3.6.1 Kicker

A kicker magnet is used to deflect and steer the particle beam in a controlled manner. This is achieved through the use of pulsed magnetic fields at precise intervals, in order to induce the

necessary changes in the particle beam's direction. The magnet is usually designed with a very fast rise time of around 100 ns to a few μs [41]. This is achieved through the use of conductors with a low number of coils (ideally one). The reason for the quick rise time being chosen is due to the possibility of instabilities in the beam arising during the ramp. However, it should be noted that for multi-turn injection/extraction slow kickers are used. The optimisation looked at was to minimise the stray field impacting the circulating beam. Otherwise the stray field could lead a potential closed orbit perturbation and tune modification. There was some optimising of the main field quality, despite the lack of strict requirement of good fields since it would be in a single pass set-up. Deflection uniformity can be influenced by electric fields due to the relatively low flux-density [42]. The choice of the shaping of the return conductor and yoke can help to achieve good deflection uniformity. The time domain is also important for a kicker to ensure flatness of pulse, fast rise and fall time, and to reduce any ripple after the pulse.

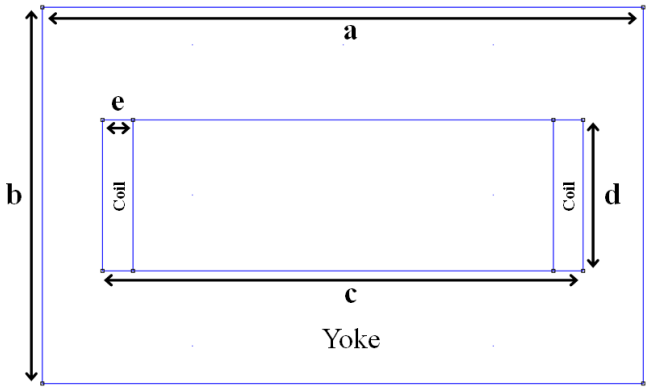

Figure 3.23: Diagram depicting the geometry of the kicker magnet designed

The 2D kicker designed can be described by 5 geometric parameters shown in Fig. 3.23 where a, b, c and d describe the yoke and the e denotes the thickness of the coil. A constant overall size of the kicker magnet was considered therefore a and b were kept the same at a value chosen to fit the beam-line best. First, the parameters geometrical parameters c and d and also the current and the number of coils were varied to look at the individual different effects. Graphs of these trends are shown below in Figs. 3.24.

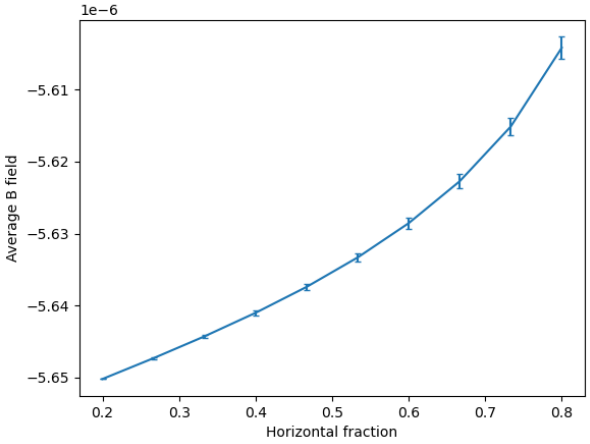

(a) Average size of the magnetic field, B, vs horizontal fraction that defines the size of the gap of the kicker

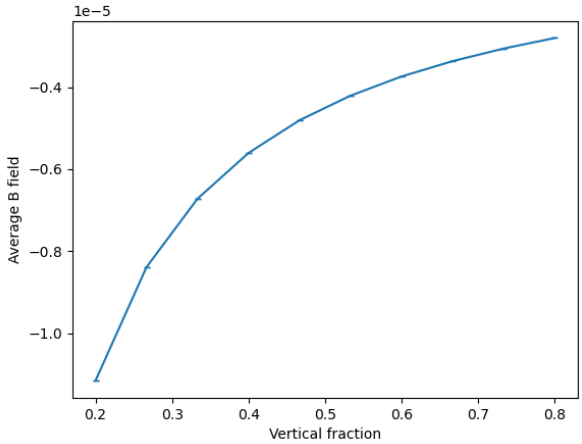

(b) Average size of B vs vertical fraction that defines the size of the gap of the kicker

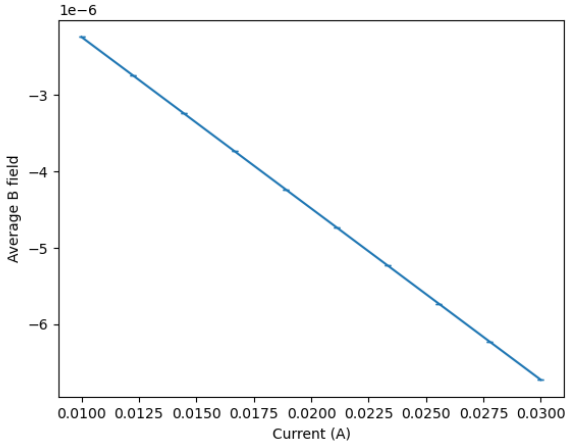

(c) Average size of B vs current of the kicker

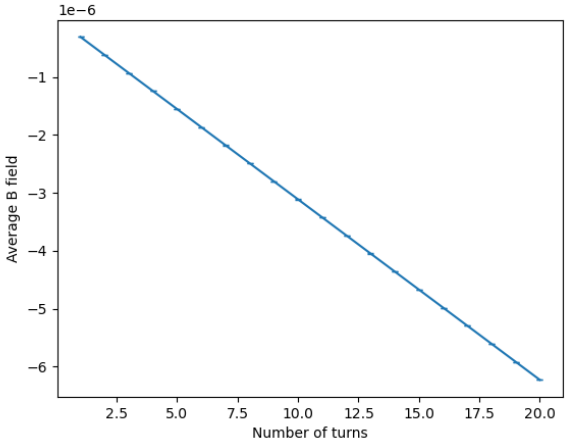

(d) Average size of B vs number of turns on the coil of the kicker

Figure 3.24: Graphs of the kicker magnetic field as a function of kicker parameters.

From this it can be seen that by decreasing the fractional sizes, and increasing the number of turns and the current, the size of the B field is increased. These parameters were then varied across the entire parameter space in order to optimise for the lowest stray fields as well as the best good field region. The optimum solution is shown in Fig. 3.25.

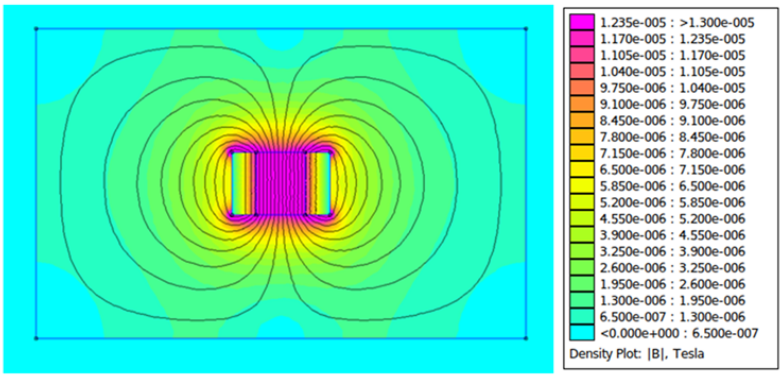

Figure 3.25: Contour plot of the magnetic fields in the kicker magnet designed

The plot of the magnetic field within the kicker (along a horizontal contour within the gap of the kicker) in Fig. 3.26 shows the level of uniformity in the magnitude of the magnetic field in red, and the good field region defined in the blue line plateau. It should be noted that, as mentioned in Section 3.1.5, the values was filtered using a low-pass filter. This was required due to some artefact that arose when numerically differentiating.

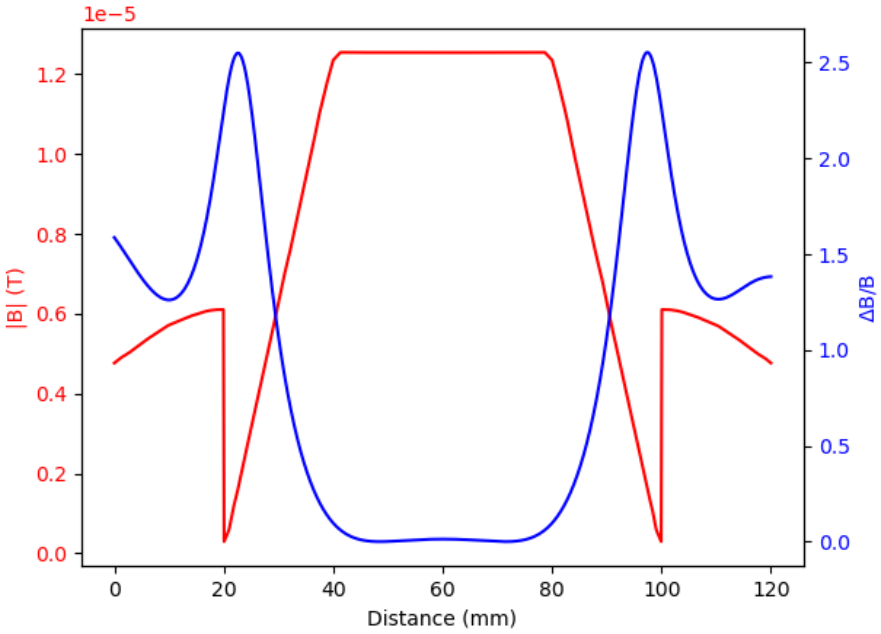

Figure 3.26: Graph of B vs. the distance along the contour in the kicker magnet designed.

3.6.2 Lambertson septum

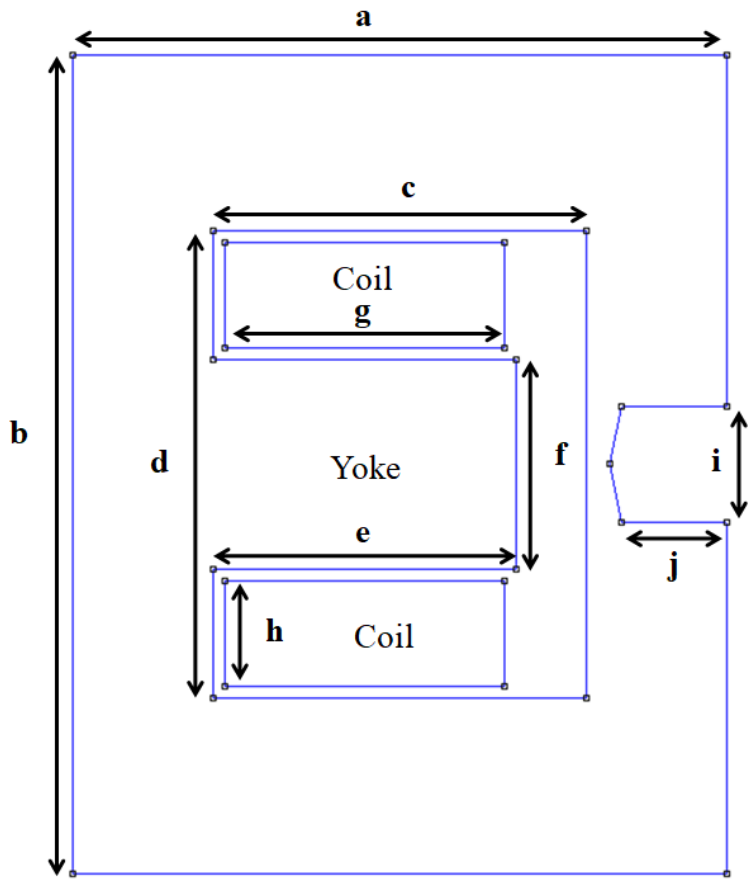

Figure 3.27: Diagram depicting the geometry of the Lambertson septum designed

There are two main types of septa. The first is an electrostatic septum, and the other is a magnetic septum (the sub-categories being a direct drive septum, an eddy current septum, and a Lambertson septum). In the interests of time, for this study only a Lambertson septum was studied. This can be constructed as either a direct current or a pulsed device which is mostly outside vacuum [43]. The conductors are encased in a steel yoke which, if far away from the beam, allows a robust low current density design. The septum is composed of the thinner part of the yoke, between the magnet aperture and the circulating beam, with additional steel required to prevent saturation. The main difference of it compared with other septa, is that the deflection of the particle is parallel (rather than orthogonal) to the septum itself. The same figures of merit, referring only to the magnetic fields, as the kicker were looked at for the septum too.

The Lambertson septum designed is defined by the geometric parameters shown in Fig. 3.27, where the magnet parameters are labelled a, b, c, d, e, f, i, and j, which specifies the yoke. Then there is g and h which define the size of the coils. The geometrical parameters c, d, e, f, g, and h were

varied to see how each variable impacted the fields whilst maintaining the same overall size of the yoke. The variables i and j were kept constant in order to have just enough room for the beam pipe. Plots showing how these changes affected the fields in the septum are shown in Fig. 3.28.

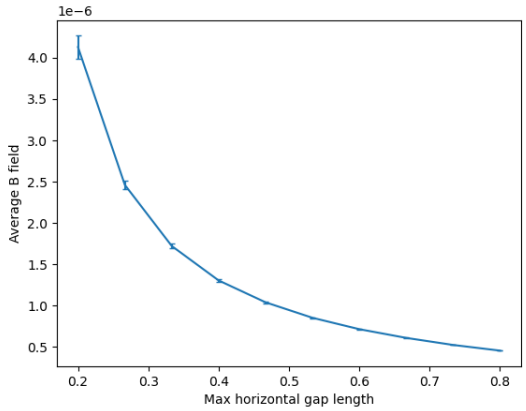

(a) Average magnitude of the magnetic field, B, vs maximum horizontal length of the gap of the septum

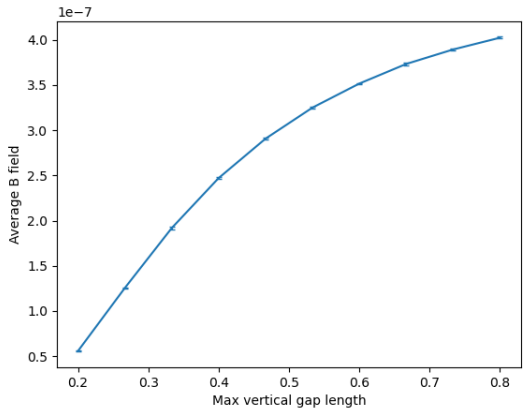

(b) Average magnitude of B vs maximum vertical length of the gap of the septum

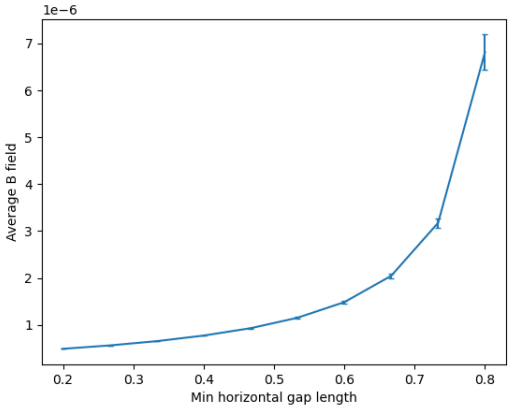

(c) Average magnitude of B vs minimum horizontal length of the gap of the septum

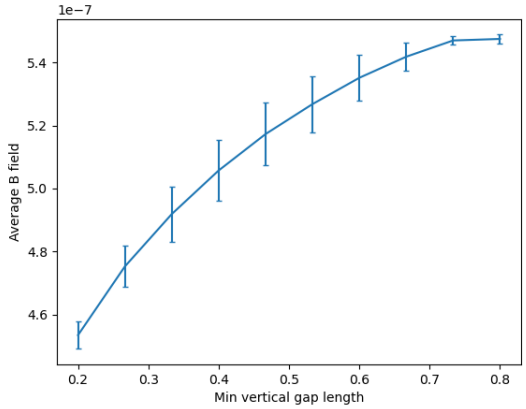

(d) Average magnitude of B vs minimum vertical length of the gap of the septum

Figure 3.28: B field as a function as a function of septum gap geometric parameters.

Then again, as with the kicker, the non-constant variables were varied across the entire parameter space. By optimising, similarly to the kicker, for the lowest stray fields and best quality of field, a solution was found. This is depicted in Fig. 3.29.

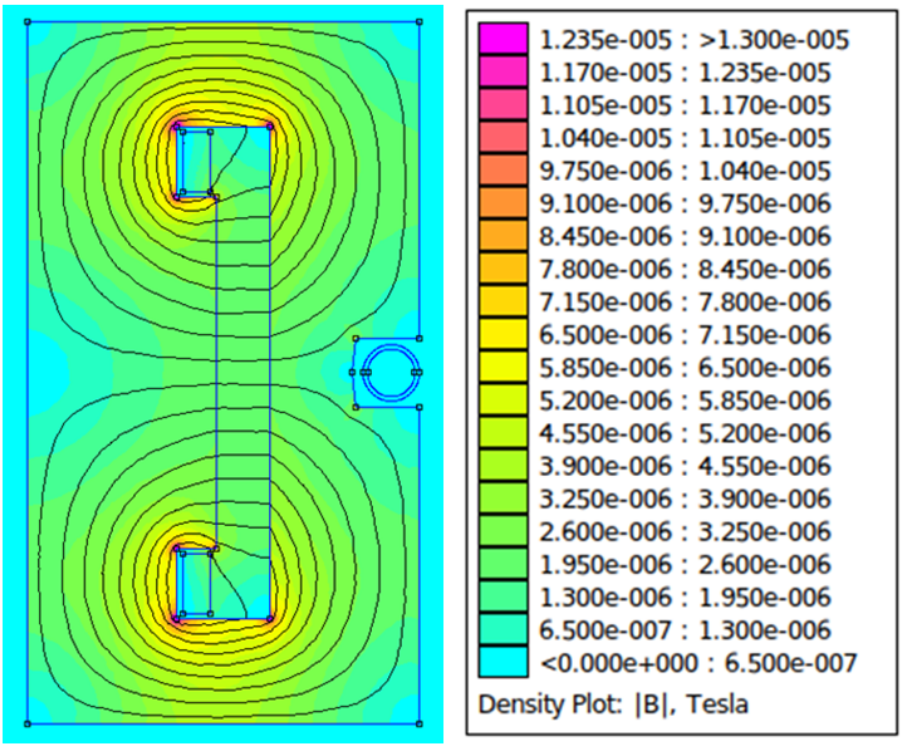

Figure 3.29: Contour plot of the magnetic fields in the Lambertson septum magnet designed.

The strength of the magnetic field along a vertical contour in the gap of the Lambertson septum shows the uniformity of the field there, denoted on the plot in red. Similarly with the kicker, the good field region is shown in blue. The black dotted lines mark the vertical gap between the coils where the good field region is best established.

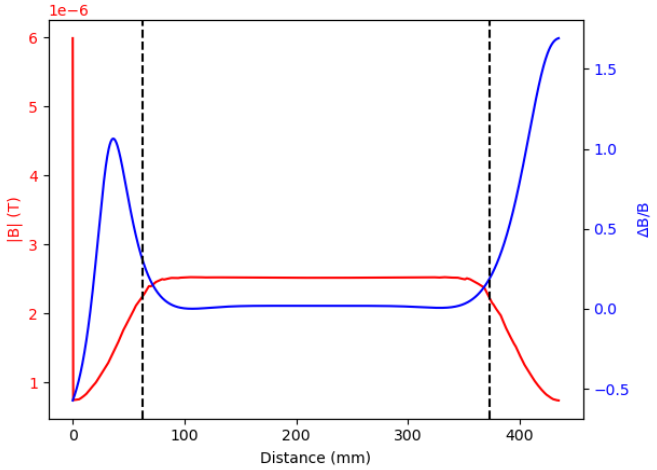

Figure 3.30: Graph of B vs. the distance along the contour in the Lambertson septum magnet designed

3.7 Wigglers

3.7.1 Design Goals

The role of the wiggler in the pDR is to make the beam oscillate, hence emitting synchrotron radiation. This radiation damping reduces the emittance of the beam. Including wigglers in the damping ring increases the amount of damping per turn and so reduces the damping time required to reach the desired beam emittance. Therefore, the principle property of a wiggler is how much radiation it causes the particle to emit. This can be calculated by modifying the equation for energy loss per turn due to synchrotron radiation to take into account the sum of the oscillations of the beam through each dipole section of the wiggler,

$$U_{wiggler} = \frac{e^2}{3\varepsilon_0 c^8}\frac{1}{m^4}\frac{E^4}{\rho}\frac{\theta N}{2\pi} \tag{3.21}$$

where m is particle mass, E is energy, ρ is radius of curvature, θ is the angle turned through in each dipole section in radians, N is the number of dipole sections and the rest are constants [44]. The constants and mass can be combined for electrons to give a simpler equation,

$$U_{wiggler} = 88.46\frac{E^4}{\rho}\frac{\theta N}{2\pi} \tag{3.22}$$

where energy is in GeV.

There are also spatial parameters to consider. The wiggler must be of an appropriate length to fit within the available space and minimise material costs, whilst being long enough to provide the required damping. The wiggler gap between poles must be large enough to leave sufficient space for the beam pipe. However, a smaller gap provides a stronger field between the opposing poles, therefore a greater amount of damping.

The period of the wiggler must also be considered as the smaller the period, the more significant the edge effects of the field, but the less the beam deviates from the axis. The width of the poles must also be sufficient to provide a good field region throughout the beam pipe.

The impact of the wiggler on the lattice should be accounted for. Ideally, the beam should have a closed trajectory, entering and leaving the wiggler with no positional or angular offset. This can be achieved by having poles of half strength at the ends of the wiggler or a series of poles with the strength ratios $B_0/4$, $3B_0/4$ and B_0 with the weakest at the end [45]. The benefit of the latter configuration is that the average beam position through the device is on-axis.

Other impacts on the lattice from the wiggler include vertical focusing effects and a beta-beat which should be accounted and compensated for in the storage ring optics.

As with all aspects of the accelerator; cost, energy usage, ease of maintenance and lifetime must also be taken into consideration.

3.7.2 Permanent Magnet Wiggler

A wiggler was designed using parameters from the MADX files describing the pDR. This included the field strength, period length and total number of periods. It was taken that the amount of damping provided by a wiggler with these properties was sufficient.

The first wiggler designed used two Halbach arrays of permanent magnets. A Halbach array is an arrangement of poles which creates a strong field one side of the magnet and a weak field on the other side, as shown in Fig. 3.31.

The wiggler was modelled using the values for the wiggler bending magnets defined in the MAD-X files for the magnets with vertically orientated fields and the drift space values for the magnets with horizontally oriented fields. The properties of the permanent magnet wiggler are summarised in Table.3.10. The material chosen for the wiggler magnets was ferrite (Y30 in the FEMM materials library) attached to a steel frame. The materials chosen and orientation of the magnetic polarisation for the permanent magnet wiggler is shown in Fig. 3.32.

Wiggler Properties	Value
Bending magnet length along axis	50.0 mm
Drift space length	30.0 mm
Magnet width in horizontal plane	100 mm
Total length	6.75 m
Magnitude of field max	0.166 T
Wiggler gap	60 mm
Energy emitted per wiggler per particle	40.7 keV
Cost of ferrite (Y30) and steel for 1 wiggler	CHF 365

Table 3.10: Properties of the permanent magnet wiggler.

Ferrite was a suitable material as it provided a field of 0.166 T with a wiggler gap of 60 mm. The MAD-X file gave a bending angle of 0.0175 rad (3sf) for the wiggler magnets, corresponding to a field of 0.162 T (3sf). The modelled value of 0.166 T is reasonably close to the desired value considering the limitations of modelling the magnet in 2D. The wiggler gap of 60 mm is to allow room for the 50 mm diameter beam pipe, with some allowance for the pipe wall thickness and other tolerances. The most significant spatial parameter affecting the field strength in the wiggler

is the wiggler gap, so an exact field strength could be optimised for by adjusting the wiggler gap. The maximum field strength varies approximately by the inverse cube law with gap width.

The cost of ferrite is lower than other materials considered, such as Samarium Cobalt magnets (SmCo32 in FEMM) and neodynium magnets (N52 in FEMM). The approximate material cost of the steel and ferrite needed for a single wiggler of the dimensions modelled was calculated to be 365 CHF, using a steel price of 0.46 CHF/kg and a ferrite price of 0.48 CHF/kg [46][47].

The wiggler was modelled in FEMM, as shown in Fig. 3.33. Other software, including RADIA from ESRF, was considered, but FEMM seemed to provide the simplest starting point and would make the wiggler design more cohesive with the other magnets. However, FEMM only models systems in 2D, which meant that edge effects from the dimensions not modelled were not taken into account. This was particularly an issue for the wiggler as it has a large number of edges between different magnetic poles. It became particularly apparent that this was an issue when comparing the wiggler modelled using the same parameters but in different planes. For example, the maximum field strength between the poles when modelling the wiggler in the z-y plane, as shown in Fig. 3.34, was 0.166 T. When modelled in the x-y plane using the same parameters, as shown in Fig. 3.35, the maximum field was 0.220 T; 1.33 times the value at the same point modelled in the other plane. The value from the z-y plane will be closer to the true value if the wiggler were modelled in 3D as more of the edges between the magnets are accounted for in that plane. However, it will still not be completely accurate and modelling the wiggler in 3D is needed to better understand the fields it would provide.

The issue with modelling in 2D meant that it was not possible to provide an accurate prediction of the good field region in the x-y plane and determine the optimal width of magnet in the x-y plane to provide a good field throughout the 50 mm beam pipe. A width of 100 mm was chosen for the purposes of estimating material costs.

To attempt to make the path of the beam through the wiggler closed and on average on axis, the $B_0/4$, $3B_0/4$, B_0 arrangement of end poles was chosen. To create these weaker fields, the wiggler gap was increased at the ends, as shown in Fig. 3.36. The gap distances needed were calculated using the inverse cube law. However, the wiggler gap values this inverse cube model gave did not provide the desired field when modelled in FEMM, as the values in Table 3.11 show. An inverse square model was also trialed and was closer, but still inaccurate, as shown in Table 3.12. The wiggler was modelled both with a horizontally polarised magnet drift section at either end and without and the design with them had some high field hot spots at the ends, so was disfavoured.

The 2D model of the wiggler end is shown in Fig. 3.36. The field between the end wiggler poles will be affected by the other nearby poles in the wiggler and other edge effects, so the inverse cube

Wiggler Gap, mm	Ideal Field, B_0	Ideal Field, T	Modelled Field, T	Modelled/ideal field, %
120	1/4	0.0415	0.106	255
69.3	3/4	0.1245	0.150	120
60	1	0.166	0.166	100

Table 3.11: Wiggler end pole gaps calculated using the inverse cube law and the ideal fields this would provide compared to the fields as modelled in FEMM.

Wiggler Gap, mm	Ideal Field, B_0	Ideal Field, T	Modelled Field, T	Modelled/ideal field, %
95.2	1/4	0.0415	0.0833	201
66	3/4	0.1245	0.141	113
60	1	0.166	0.161	97.0

Table 3.12: Wiggler end pole gaps calculated using the inverse square law and the ideal fields this would provide compared to the fields as modelled in FEMM.

model is too simplistic to model the field accurately. Further work is needed to create a better model for the field strength at the end of the wiggler or to optimise analytically, preferably in 3D. Particle tracking simulations through the wiggler would also be needed to optimise the design to keep the beam path closed and on axis on average.

3.7.3 Wiggler with Electromagnets

A second wiggler design was considered - one where each dipole was an electromagnet instead of a permanent magnet. It was hoped that such a design would allow the magnetic field of the wiggler to be varied (in case the wiggler is ever repurposed for different particles) and would allow the wiggler to be used for longer (as electromagnets do not demagnetise like permanent magnets). However, it was recognised that a wiggler with electromagnets would potentially require more (expensive) material than a permanent magnet wiggler. Hence, a working design was proposed so that a cost comparison could be made.

The wiggler with electromagnets used exactly the same materials as the dipole design (Section 3.2):

- Pure iron for the yoke, nonlinear B-H curve, electrical conductivity of 10.44 MS/m
- Copper for the coils, linear B-H curve, electrical conductivity of 58 MS/m

It was identified from the pDR MADX file [17] that there were 84 dipoles constituting the lattice, i.e. 42 N-S S-N pairs (cells). From the Conceptual Design Report, the total length of the wiggler was 6.64 m [22]. Hence, each cell of the wiggler should be roughly 158 mm long. By keeping the number of cells, total wiggler length, and magnetic field of each dipole the same as in the MAD-X file, it was ensured that the wiggler would achieve the desired emittance damping.

Note that, unlike the permanent magnet wiggler in Section 3.7.2, the wiggler was designed with electromagnets in a standard wiggler configuration with alternating dipoles instead of using a Halbach array. The coils required to operate the electromagnets took up additional room, which prevented the inclusion of any dipole electromagnets with field lines oriented horizontally. If such dipoles had been included, then the coils would have stuck out into the beam-pipe.

The design for one cell of the wiggler is shown in Figure 3.37:

To create enough space for the coils within the 158 mm cell length, the poles had to be severely thinned relative to the permanent magnet wiggler. The cross-sectional area of the coils themselves also had to be reduced. Therefore, to maintain the same cross-sectional size per turn as in the dipoles (139 mm^2/turn, Section 3.2), the number of turns per coil had to be reduced to eight. Furthermore, by reducing the number of turns per coil, the current had to be kept at a relatively high 151.198 A to achieve the desired central on-axis field of 0.1616 T. Note that this current is still only a third of that used in the JAI example file (450 A [36]). Despite all the constraints imposed above, and with a desired B-field nearly three times higher than that of the dipoles in Section 3.2, all the B-fields throughout the wiggler cell electromagnet remained below 1 T. Overall, this electromagnet is still far from saturation.

The wiggler cell in Fig. 3.37 was then duplicated 41 more times and connected horizontally to form a complete wiggler of length 6.636 m. The entire wiggler with electromagnets is shown in Fig. 3.38:

As explained in Section 3.7.2, using only FEMM to model the wiggler in 2D prevented us from properly characterising the good field region (GFR). The B-field in the xy-plane between the poles (in and out of the page) was substantially different from the B-field in the xz-plane between the poles (along the beam-pipe). Hence, it does not make sense to discuss "one-dimensional GFRs" for the wiggler. Nevertheless, the fractional difference relative to the target field along the entire axis was plotted. A cropped plot of this difference measured along the axis of one of the central cells is shown in Fig. 3.39. At the moment, the "one-dimensional GFR" is roughly 1 mm for each of the 84 dipoles, so further optimisation needs to be made.

Once there was a design for the wiggler with electromagnets, a basic estimate of the cost was made to compare it with that of a permanent magnet wiggler. For consistency with the permanent

magnet wiggler, the wiggler with electromagnets was assumed to have the same width in the horizontal plane of 100 mm. This width allowed us to estimate the volume of pure iron in the yoke and the volume of pure copper per turn per coil. The materials cost breakdown for one wiggler is given in Table 3.13:

Material	Price	Volume (one wiggler)	Cost (one wiggler)
Pure iron	4844 CHF/m^3 [48]	0.153 m^3	741 CHF
Pure copper	2.02×10^5 CHF/m^3 [49]	0.073 m^3	14 750 CHF
Total			15 491 CHF

Table 3.13: Materials cost breakdown of our wiggler design with electromagnets

The cost comparison of the two wiggler designs is in Section 3.7.4.

3.7.4 Comparison of Permanent and Electromagnetic Wiggler

The permanent magnet wiggler would be cheaper to build initially due to low material costs. However, permanent magnets demagnetise over time and demagnetisation can be increased by exposure to radiation. Further studies are needed to determine the rate of demagnetisation and therefore the lifetime of the permanent magnet wiggler expected before the magnets would need to be re-magnetised or replaced. If demagnetisation happens too quickly this could mean the permanent magnet wiggler would be more expensive overall due to higher maintenance costs, or even unfeasible altogether. However, an electromagnetic wiggler needs power from the grid to run. This increases the cost of running the wiggler as well as having a negative environmental impact.

Another consideration is the tuning of operation of the wiggler. The electromagnetic wiggler has the benefit of allowing adjustment of field strength by simply changing the current through the coils, whereas the permanent magnet wiggler is more challenging to adjust. The permanent magnet wiggler field strength could be adjusted by changing the wiggler gap but this introduces engineering challenges around how to precisely move the magnets. The wiggler gap is limited by the size of the beam pipe so as the permanent magnets demagnetise there will come a point where the field is no longer sufficient even with the minimum wiggler gap.

The initial materials cost of the electromagnetic magnet wiggler is far greater than for the permanent magnet wiggler, in most part due the cost of copper for the coils. The costs of the iron-based cores are comparable. The labour cost of the wiggler with electromagnets might also be higher as the copper coils must be wound around the cores.

Further work is needed to determine whether the wiggler should use a permanent magnet or electromagnet design. However, as environmental impact become an increasingly significant consideration when designing accelerators, increasing the use of permanent magnets where possible is preferred.

3.8 Conclusion

The dipole, quadrupole, sextupole, kicker, and septum were each designed with a sufficient good field region to ensure their effectiveness. For the wigglers the good field region analysis requires a full 3D simulation. Although, not strictly necessary, the B-field of all the magnets were kept below the saturation value to avoid the damage it would cause. This was of most importance for the kicker since it would subject to ramping. Whilst for the rest of the magnets only one possibility was explored, for the wiggler two different designs were looked at. The electromagnetic wiggler offered the benefit of tunability of the field, on the other hand the permanent magnet wiggler would be cheaper to build and run. The disadvantage of the permanent magnet wiggler would be that it may need more maintenance due to demagnetisation. Hence, further studies are required to determine which design is best suited for specific applications

3.9 Further Work

3.9.1 3D Analysis

One key aspect to improve the reliability of these designs is modelling the magnets in 3D which can be done using software such as Opera [50]. This enables the establishment of a comprehensive good field region. It is especially important for wiggler magnets, since edge effects can significantly impact their performance and can only be evaluated in 3D. Additionally, particle tracking in these 3D field maps can be used to evaluate the effectiveness of each magnet design. Software such as SIMION® could be utilised for this purpose [51]. Understanding the impacts of the magnets on the accelerator's lattice, such as vertical focusing, is also essential. 3D modelling also allows for the calculation of off-axis magnetic fields useful for validating circular symmetry. For example, in the case of the sextupole, analysis of the multipole expansion in 2D along different axes can help ensure the good field region has circular symmetry within it.

3.9.2 Cost Optimisation

Some consideration of the costs were taken into account, however, there is some scope left unexplored due to time constraints. There are a few ways of minimising costs, the main ones identified to be: material choice for all the different elements of the magnets, and the quantity of material used, which has to be weighed up against the geometrical fine tuning.

In terms of materials, more in-depth studies should be conducted to compare the performance of different mediums that could be used for the magnets. There is also structural and thermal analysis that could be carried out to determine whether the magnets can withstand the heat and stress they will encounter. This is particularly key for a kicker magnet that would be subject to ramping. Investigating these ramping effects on the kicker magnets would help improve performance. Also, a more in-depth comparison of different kinds of wigglers is required to determine the most effective design for specific applications. Further exploring of the choice of the magnet coolant is also important.

Some additional research needs to be done into chamfering and shimming possibilities for the magnets especially the sextupole, kicker, septum and wiggler. Chamfering is good from a safety point of view since it removes sharp edges. It also allows for the magnet to fit more snugly with other components within the damping ring. Shimming adjusts the homogeneity of a magnetic field which can extend the good field region, therefore making the magnet more efficient. Optimising the wiggler magnet ends to ensure the beam is on average on-axis is also necessary.

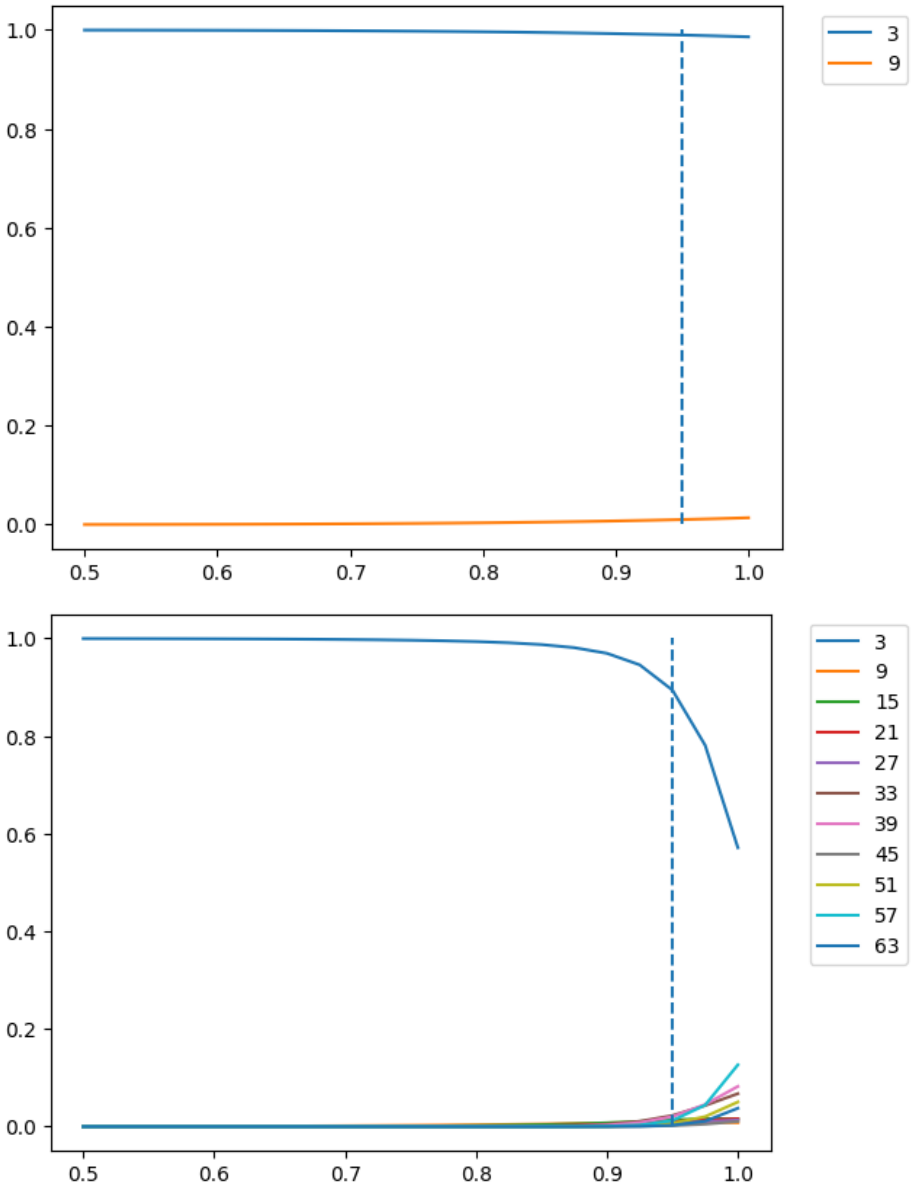

Figure 3.22: Contribution to sextupole field second derivative of different harmonics with radius. Sampling radius of 0.95 (in units of beam pipe radius) is shown with a dashed line. It is clear that within the sampling radius, the field is primarily formed from the fundamental harmonic. Left: 2 harmonics (fundamental +1). Right: 11 harmonics (fundamental +10).

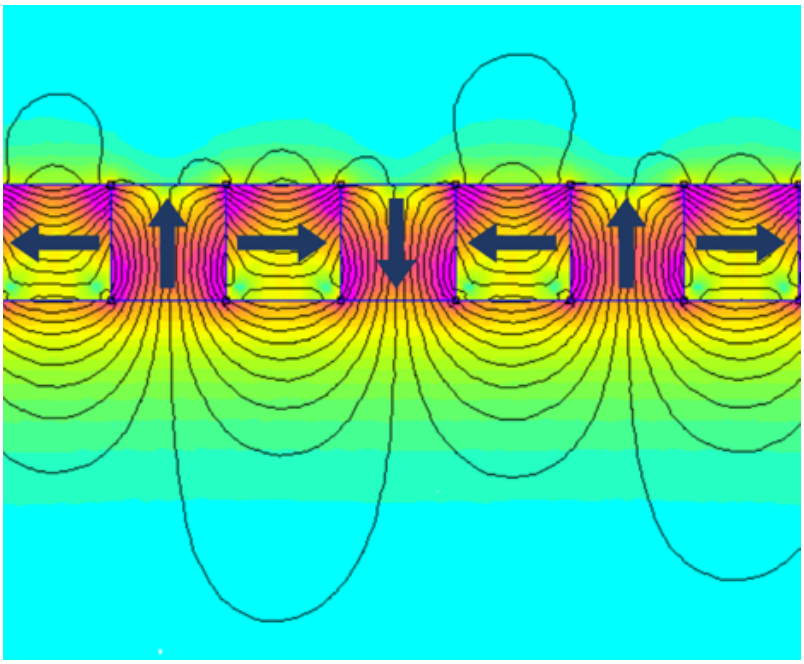

Figure 3.31: Simple Halbach array of permanent magnets modelled in FEMM with arrows to indicate the direction of each magnet's polarisation.

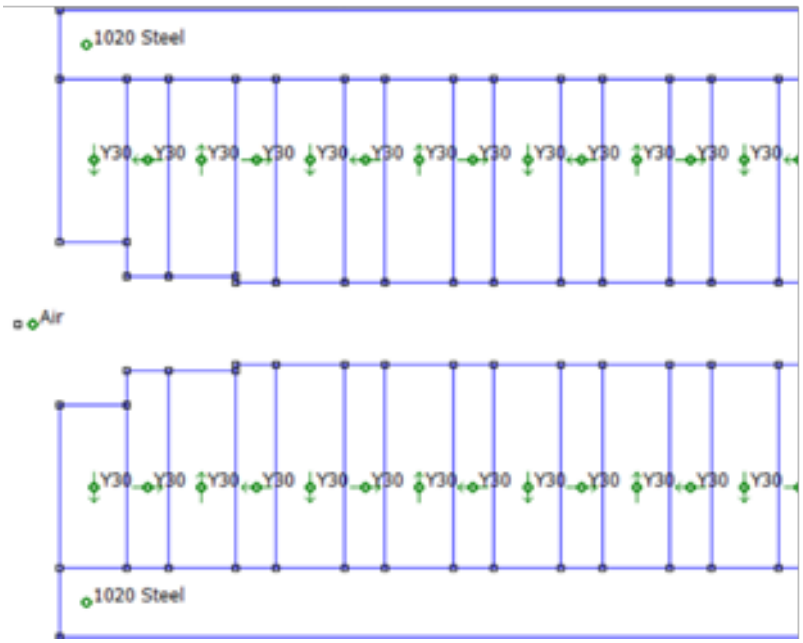

Figure 3.32: First few cells of the permanent magnet wiggler modelled in FEMM, showing the materials used in the model and the polarisation of the magnets in the two Halbach arrays.

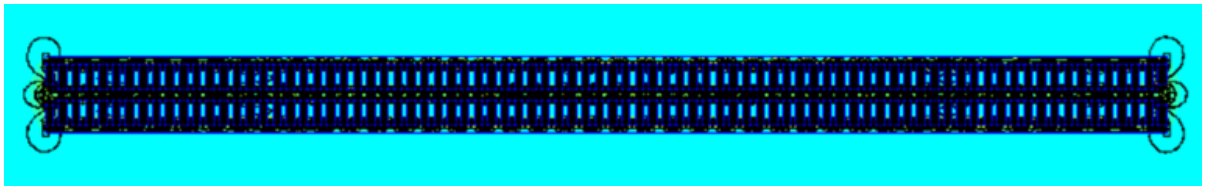

Figure 3.33: The entire permanent magnet wiggler modelled in the z-y plane in FEMM.

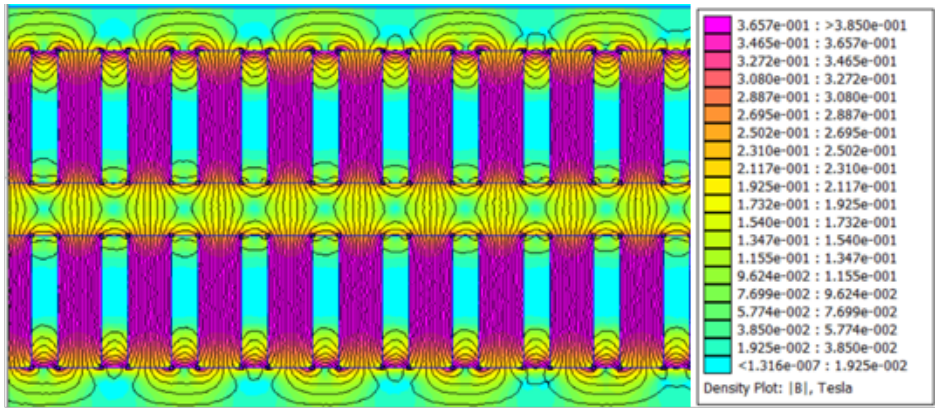

Figure 3.34: The permanent magnet wiggler modelled in the z-y plane in FEMM zoomed in.

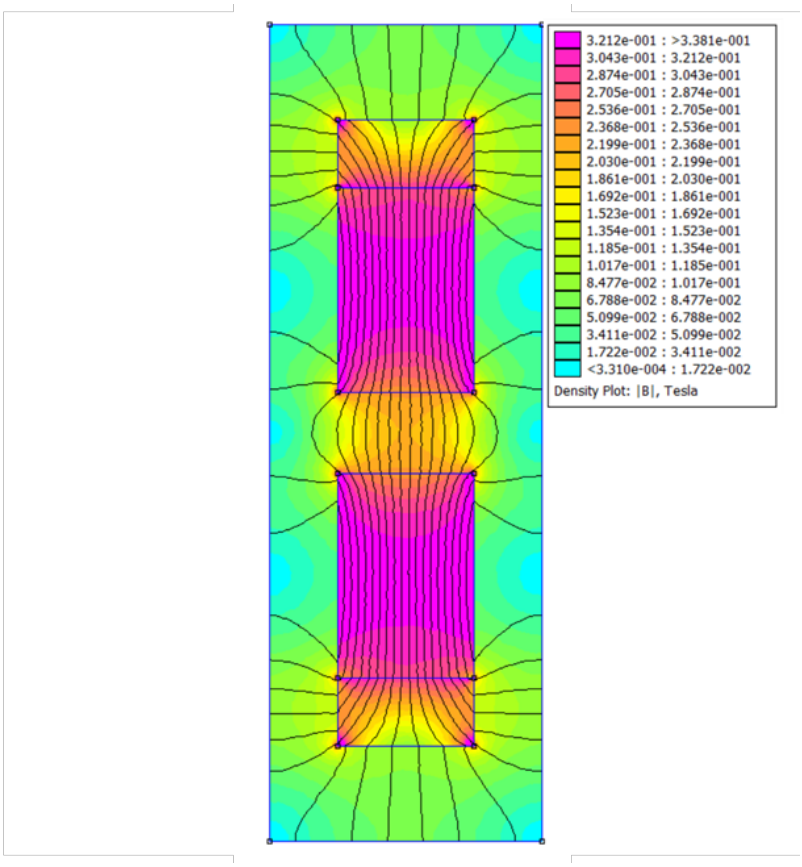

Figure 3.35: The permanent magnet wiggler modelled in the x-y plane in FEMM.

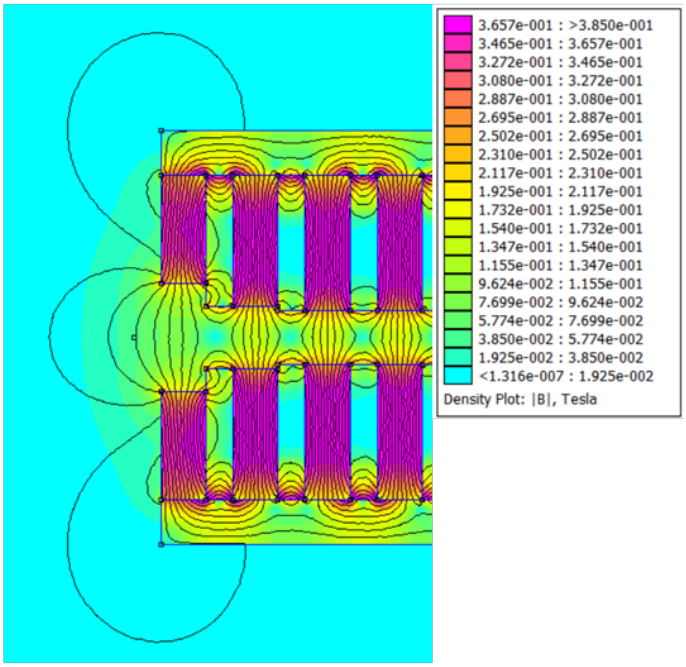

Figure 3.36: The permanent magnet wiggler modelled in the z-y plane in FEMM, zoomed in to show the fields at the wiggler ends, with the varying wiggler gap calculated using the inverse cube law.

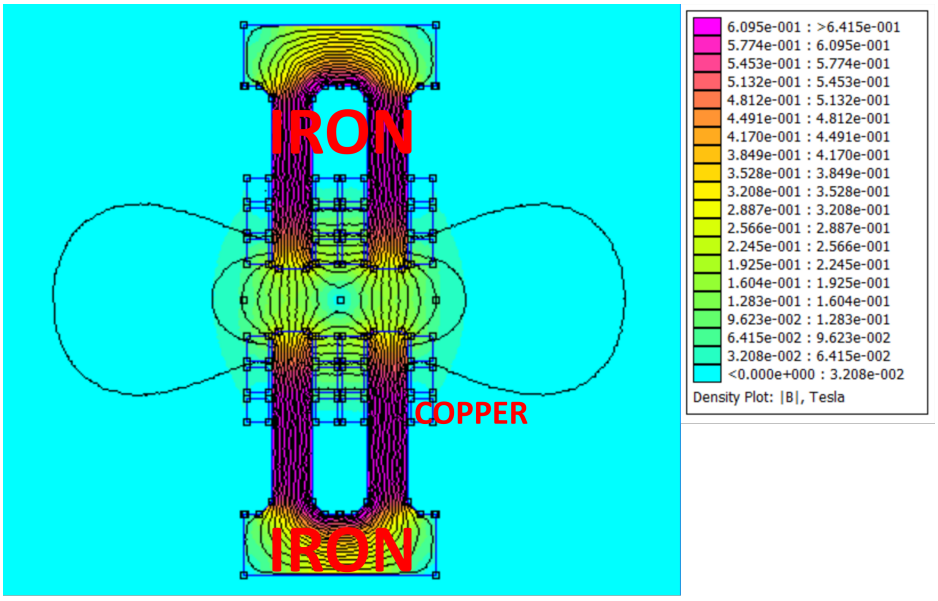

Figure 3.37: Cross-section of a potential two-dipole electromagnet cell for the FCC-ee pDR wiggler.

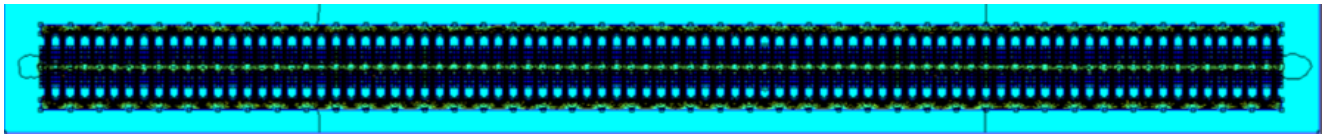

Figure 3.38: Cross-section of a potential wiggler design with electromagnets for the FCC-ee pDR wiggler.

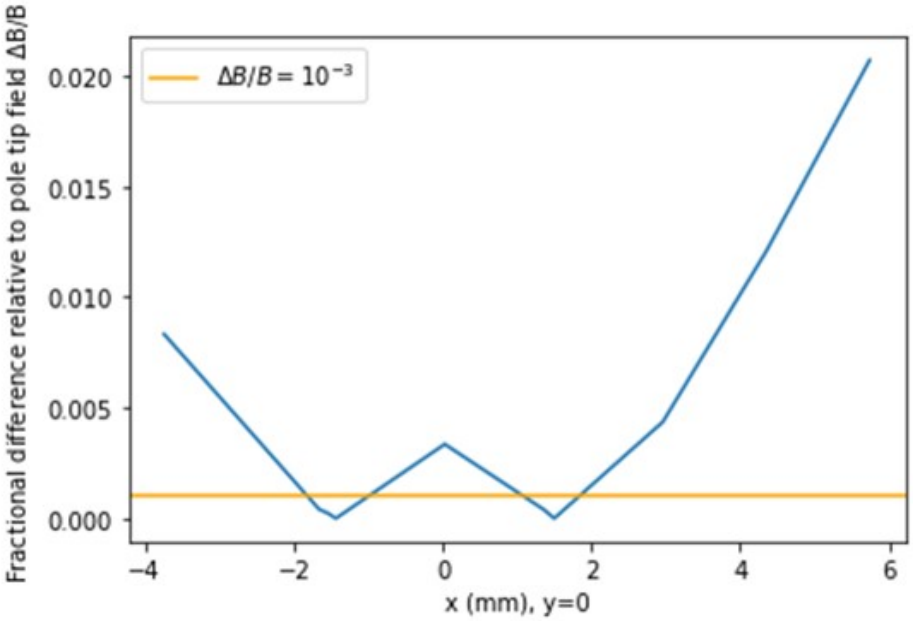

Figure 3.39: Fractional difference ("1D z-axis GFR") of the wiggler with electromagnets cropped to one of the central cells.

Chapter 4

RF cavities

4.1 Introduction

The pDR of the FCCee pre-injector complex reduces the emittance of a positron beam by the emission of synchrotron radiation. This is given off by the positrons when they interact with magnetic fields in the ring. To maintain the beam energy while reducing its emittance, RF cavities are used to generate electromagnetic fields that oscillate at the same frequency as the beam and accelerate it, replacing the energy lost to synchrotron radiation. This allows for an efficient damping of the positron beam and effective control over its size and shape [52].

4.2 Design Considerations

The pDR requires a set of RF cavities to mitigate losses from synchrotron radiation. The single particle energy loss per turn in a ring can be derived from

$$U_0[\text{keV}] = 88.46 \frac{E^4[\text{GeV}]}{\rho[\text{m}]}, \tag{4.1}$$

where E is the beam energy, and ρ is the bending radius [53]. The synchrotron radiation emitted from both the dipoles and wigglers in the pDR amounts to an energy loss per turn of 0.227 MeV [54]. The total radiated power from synchrotrons radiation per turn is given by,

$$P = N_p N_b \frac{e^2 E^4}{6\pi\epsilon_0 c^7 m_e^4 \rho^2}, \tag{4.2}$$

where N_p is the number of particles per bunch and N_b the number of bunches. A total of 16 kW will be radiated by the pDR [54]. To mitigate the energy loss from synchrotron radiation, a minimum

RF voltage of 4 MV is required per cavity. The infrastructure of the pDR limits the number of RF cavities to two, each 1.5 m in length [55]. A summary of the predefined design parameters for the RF cavities is given in Table 4.1.

Parameter	Unit	Value
Beam energy	GeV	1.54
Cavity length	m	1.5
Total RF voltage	MV	8.53
Minimum RF voltage	MV	0.225

Table 4.1: Design parameters of the RF cavities for the FCCee pDR.

4.2.1 RF Frequency

The operating frequency of the RF cavity is given by,

$$f_{\mathrm{RF}} = h f_{\mathrm{rev}}. \tag{4.3}$$

where h is the harmonic number and f_{rev} is the revolution frequency of the pDR. Given a harmonic number of 319, and a circumference of 239.26 m, an RF frequency of 399.7018 MHz is required. Since the harmonic number is proportional to the number of bunches, frequencies of 800 MHz can also be considered.

For the pDR, four different designs for the RF cavities were proposed, two 400 MHz and one 800 MHz elliptical superconducting cavities, as well as a 400 MHz side-coupled normal-conducting cavity.

4.2.2 Cavity Mode

RF cavities can be arranged in multi-cell configurations to enhance the accelerating efficiency [56]. Each cavity cell has a corresponding mode, similarly to a set of coupled oscillators. A series of modes of the same type forms a passband. The π mode, where π corresponds to the cell-to-cell phase difference, is the most commonly used accelerating mode for RF cavities. It allows for an equal distribution of the field energy across the cavity. Each cell therefore contributes equally to acceleration. For a cavity with more than ten cells, the $\pi/2$ mode is typically used.

Given the small number of cells required for the RF cavities in the pDR, a π mode was chosen for all three designs.

4.3 Software

The design parameters for the RF cavities were optimised using appropriate numerical design tools, SUPERFISH and CST Studio.

SUPERFISH is a software that utilises finite element solver technology to generate a 2D mesh and calculate field lines for a range of RF cavity designs. It allows the user to specify the desired geometry and frequency, which the software automatically tunes to match. The RF cavity can be simulated from an axisymmetric cross-section, which greatly improves the computational speed [57].

In the case of elliptical cavities, the solver's multi-cell extension, AUTOFISH, takes the user-defined geometry and frequency to produce the electric field on the cavity structure for a symmetric half-cell cavity. The cell number can also be specified, and the resulting figure can be interpolated to show the electric field's shape on the axis. The modulus of this graph can then be integrated to provide the integrated voltage for the setup [57].

However, SUPERFISH's ability is limited to only creating 2D meshes for the cavities. Therefore, CST Studio Suite is utilized to create a 3D mesh for the cavity. The standard procedure involves taking the well-optimized geometry values from SUPERFISH and implementing them into CST using an inbuilt macro to create a 3D design of the same cavity. In this project, the eigenmode solver in CST was used to compute electromagnetic fields and determine cavity modes in a given 3D model. The good agreement between the results obtained from CST and SUPERFISH validates the suitability of the cavity design [58].

4.4 Figures of Merit

The acceleration efficiency of an RF cavity can be described by a number of figures of merit, which depend on parameters of the cavity, including the geometry and materials used.

4.4.1 Quality Factor

The power loss in the cavity is determined by the quality factor Q, which represents the number of RF cycles required to dissipate the stored energy,

$$Q = \frac{\omega U}{P_{\text{loss}}}, \tag{4.4}$$

where U is the energy stored in the cavity, P_{loss} is the total power loss in the cavity, and ω is the operating frequency. The sources of loss include dielectric and magnetic, conduction, and external. The external loss comprises the electromagnetic energy propagating out of the cavity through the beam pipes or couplers. The loaded quality factor is derived from the addition in parallel of all Q-factors from each type of loss. In normal-conducting cavities, Q ranges from 10^5 to 10^6, while for superconducting cavities it ranges from 10^{10} to 10^{11}.

4.4.2 Transit Time Factor

The electric field on axis in an RF cell varies sinusoidally. Because of this effect, only a fraction of the peak voltage contributes to the acceleration of a particle in the cavity. The transit time factor determines the loss in energy gain from the longitudinal variation of the electric field in a cavity,

$$T = \frac{\int_{-L/2}^{L/2} E_z \cos\left(2\pi z/\beta\lambda\right) dz}{\int_{-L/2}^{L/2} E_z dz}, \tag{4.5}$$

where L is the length of the cavity, β is the relativistic factor, and λ is the RF wavelength.

The transit time factor is typically maximised in the design of a cavity. Given the relativistic beam energy of 1.54 GeV in the pDR, the cavity dimensions are comparable with half the RF wavelength. Therefore, a loss in efficiency from the transit time factor is not significant.

4.4.3 Surface Resistance

The RF surface resistance, R_s, varies with the cavity material, and is inversely proportional to the skin depth δ and conductivity σ,

$$R_s = \frac{1}{\sigma\delta}. \tag{4.6}$$

The skin depth is the distance required to suppress EM fields to $1/e$ of their initial value. The skin depth for a good conductor is given by

$$\delta = \sqrt{\frac{2}{\sigma\mu\omega}}, \tag{4.7}$$

where ω is the operating frequency, and μ is the permeability of the cavity material.

The RF surface resistance sets the maximum magnetic field on the cavity walls, which corresponds to 200 mT in niobium cavities at 2.0-4.5 K [59]. In normal-conducting copper cavities, R_s is of the order of a few mΩ, while in superconducting cavities it is of the order of nΩ. This allows for a significantly lower power loss in the cavity walls, and higher accelerating gradient. A geometrical factor $G = R_s Q$ was defined in order to remove the contribution of R_s from Q.

4.4.4 Shunt Impedance

The shunt impedance measured in units of Ω/m is a measure of the accelerating efficiency. It is a geometry-dependent factor. The shunt impedance per unit length can be derived from,

$$Z = \frac{E_0^2}{P/L} \tag{4.8}$$

where E_0 is the average axial electric field in the cavity, and P/L is the power dissipated in the cavity walls per unit length. The effective shunt impedance $r = ZT^2$ accounts for the finite particle velocity by including the transit time factor. Typical values for normal-conducting linear accelerator are in the order of 30 to 50 $\mathrm{M\Omega\,m^{-1}}$. The r/Q parameter is used to measure the efficiency of acceleration per unit stored energy.

Although the effective shunt impedance is not relevant for superconducting cavities, its value should be kept large enough to optimise ZT^2/Q within typical values in the order of 100 Ohms.

4.4.5 Kilpatrick Factor

The Kilpatrick limit sets the design electric field level [60]. The breakdown field in resonant cavities is related to the operating frequency,

$$f_{\mathrm{RF}} = 1.643 E_k^2 \exp\left(-8.5/E_k\right), \tag{4.9}$$

where E_k is the Kilpatrick limit of the electric field in MV/m and f_{RF} in MHz. Surface fields up to $2E_k$ can be achieved.

4.5 Normal and Superconducting Cavities

This section outlines the key differences between normal conducting (NC) and superconducting (SC) cavities. This is followed by a preliminary evaluation of the suitability of SC cavities for the pDR, due to an improved compatibility with the relevant figures of merit.

Superconducting RF cavities are made of materials that have zero electrical resistance at low temperatures, such as niobium. This allows for the cavities to operate at high electric fields without significant energy losses. Superconducting RF cavities are typically cooled to very low temperatures (below 2 K) using liquid helium, which is expensive and requires specialist equipment [61].

On the other hand, normal-conducting RF cavities are made of materials that have non-zero electrical resistance. This means that when an electric field is applied, energy is lost due to resistive heating. Normal-conducting RF cavities are typically cooled to room temperature using water or air cooling [61].

The main advantage of superconducting RF cavities over normal-conducting RF cavities is their higher accelerating gradient. This means that particles can be accelerated to higher energies in a shorter distance, which reduces the size and cost of the accelerator. Superconducting RF cavities also have lower power consumption, which reduces the operating costs of the accelerator. This is in part due to lower energy dissipation, which ensures a higher quality factor, Q, and geometrical factor, G [62].

However, superconducting RF cavities are more expensive to manufacture and require more specialised equipment for cooling and operation. Fortunately, a large amount of SC technology, equipment and cooling facilities is already available at CERN, which reduces the added costs [63].

In the case of the FCCee positron damping ring, preference is given to SC cavities, due to a better performance in terms of the relevant figures of merit and the technology already being available on-site.

4.6 Secondary Effects

The design of an RF cavity includes the mitigation of secondary effects which can negatively impact the relevant figures of merit. Given the software used for this report, SUPERFISH and CST Microwave Studio, a complete analysis of these effects could not be performed. Nevertheless, significant effects were listed, along with preliminary approaches to mitigate them through the geometrical factors.

A change in the profile or material of an RF cavity can affect its configuration. The input beam can lose part of its energy, which induces electromagnetic wake-fields for the passing of multiple bunches. To reduce the wake duration, an optimisation of the geometry and material of the cavity is required. Longitudinal wake-fields cause beam loading, where the beam energy and energy spread varies per bunch [64]. Transverse wake-fields cause instabilities excited by off-axis trajectories, called beam break-up [65].

Another effect occurs when the cavity geometry allows for the generation of secondary electrons, which can then be accelerated in one accelerating period and collide with the surface of the cavity. This process is called multi-impacting, or multipacting [66]. Provided enough energy is deposited

in the cavity, the resulting thermal effects can lead to breakdown in superconducting cavities, which will reduce the quality factor. To prevent this effect from taking place, parallel walls were avoided in the design of the superconducting cavities.

Provided high electric fields at the surface of the cavity, field emission can occur [67]. This reduces the potential barrier stopping electrons from escaping the cavity material. To reduce this effect, the E_{max}/E_0 ratio was minimised by tuning the geometrical parameters. Additionally, the magnetic field on the surface needs to be reduced below the critical field of the superconductor material of the cavity.

4.7 Higher Order Modes

An effect which was reproduced using CST Microwave Studio was the presence of higher order modes (HOMs) propagating in the cavity [68]. HOMs are a consequence of Maxwell's wave equations for a conductor, which allow for an infinite number of electromagnetic modes. These modes are described in terms of three integers m, n, q, which correspond to the field distribution in a cylindrical waveguide cavity. The fundamental transverse electromagnetic TEM_{010} mode is typically used to accelerate charged particles in an RF cavity. HOMs do not contribute to the particle acceleration and can be suppressed by increasing the bore radius, which shapes the cavity into a waveguide. Another option is adding an HOM coupler with a specific cut-off frequency.

CST Microwave Studio was used to compute the cavity modes. A sample of the electric and magnetic fields in an elliptical cavity is displayed in Fig. 4.1-4.2. The π mode was used to set the cavity length. The associated cell-to-cell phase difference of 180° for the π mode is shown in Fig. 4.2a. The H-field lines of the fundamental mode are shown in Fig. 4.1a, with peaks in the region corresponding to the dome ellipse of a cell. Note that the HOMs operate at significantly larger frequencies than the π mode frequency.

4.8 Optimisation of the Superconducting Cavity

An elliptical superconducting cavity was optimised for the pDR. The design was computed in 2D using SUPERFISH, which provided a fast evaluation of the cavity geometry. The final design was implemented in CST Microwave Studio, which allowed for a robust 3D modelling of the cavity.

The cavity geometry was optimised to increase both R_sQ and r/Q, resulting in less stored energy and less wall loss for a given gradient. Additionally, the electric and magnetic peak fields were

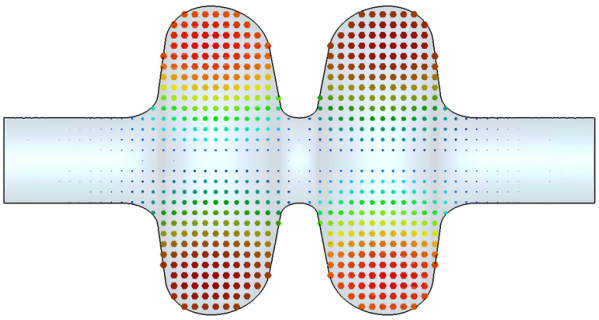

(a) H-field of the π mode at 400 MHz.

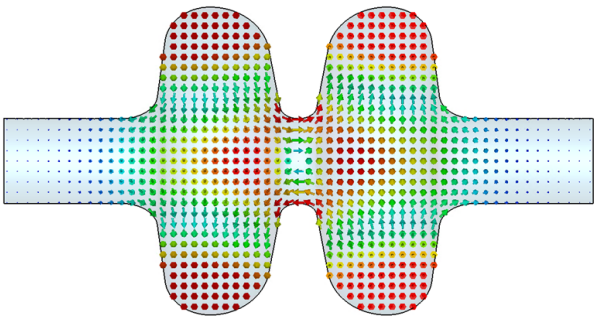

(b) H-field of the first HOM at 578 MHz.

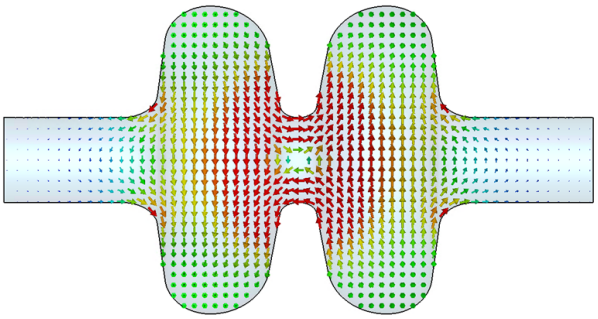

(c) H-field of the second HOM at 578 MHz.

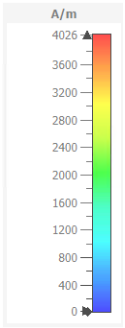

(d) Colour bar of the H fields.

Figure 4.1: Typical H fields of the modes of the 400 MHz elliptical superconducting cavity.

minimised, along with the ratio between the two, to avoid the superconducting field emission limit and quenching, which causes breakdown in the cavity [69].

The tunable geometrical parameters of the elliptical cavity are included in Fig. 4.3. The cell geometry is defined in terms of the bore radius R_{iris}, the cavity length $2L$, the iris axes a and b, the dome axes A and B, the cavity radius R_{eq}, and the wall angle α. These parameters were first optimised for a mid-cell, due to its symmetrical shape. To integrate the cavity in the pDR, a beam pipe was added to the design, and an asymmetrical optimisation of the end-cell was performed [70].

The cavity diameter, D, is used to tune the RF frequency. In a pillbox cavity, the diameter can be determined by solving

$$f_{\text{RF}} = \frac{cx_1}{\pi D}, \tag{4.10}$$

where c is the speed of light, and x_1 is a constant equal to 2.40483. This provided an initial value for the tuning the diameter of the cavities designed for the pDR.

The length of the cell is set by the cavity mode. For π mode cavities, the cavity length is equal to

$$L = \beta\lambda/2. \tag{4.11}$$

The cavity length scales inversely with f_{RF}, and therefore the length of the 800 MHz cell is half of the 400 MHz design. However, the smaller overall size of the 800 MHz cavity requires the use of

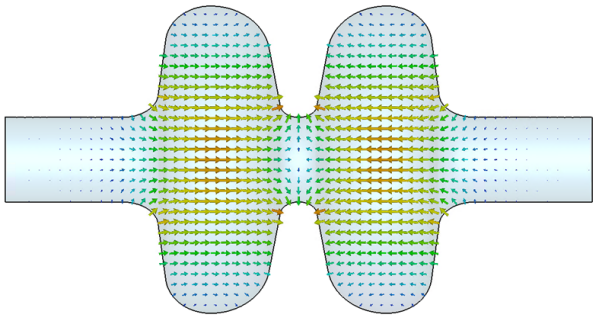

(a) E-field of the π mode at 400 MHz.

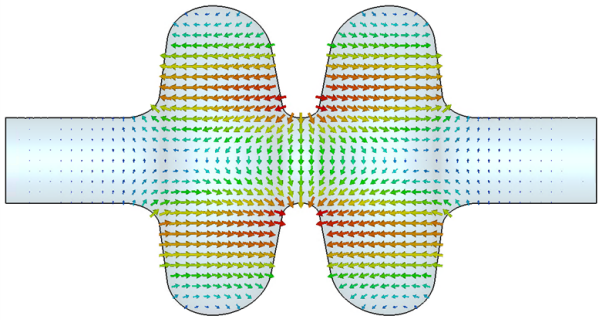

(b) E-field of the first HOM at 578 MHz.

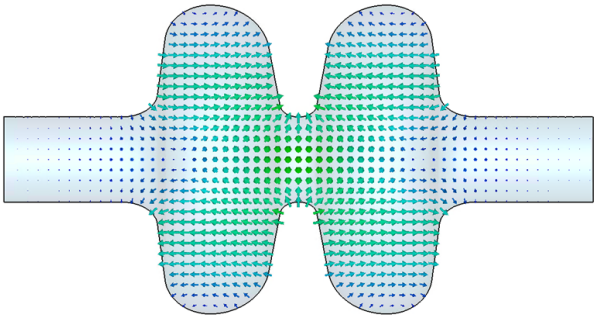

(c) E-field of the second HOM at 578 MHz.

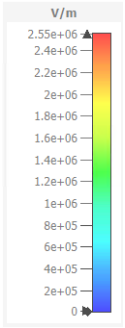

(d) Colour bar of the E fields.

Figure 4.2: Typical E fields of the modes of the 400 MHz elliptical superconducting cavity.

more cells to provide the required RF voltage.

The bore radius, or beam pipe radius, is typically set by integrating the main beam pipe in the cavity or by requirements of cell-to-cell coupling. A large bore radius dampens HOMs. However, the shunt impedance is subsequently reduced, which limits the maximum achievable accelerating gradient.

The side wall angle is defined with respect to the iris plane. A value close to 90° was avoided to prevent parallel walls in the cavity, which contribute to multipacting. The wall angle can be modified to tune the volume of the cavity and reduce the peak electric and magnetic fields.

The iris ellipse can be used used to tune the electric peak fields, while the dome ellipse can be used to tune the peak magnetic fields. The latter also has a a significant contribution to the geometry factor R_sQ, due to its larger size.

Most of the geometrical parameters have a nontrivial relation to the figures of merit, which required the use of parametric scans to establish their dependency.

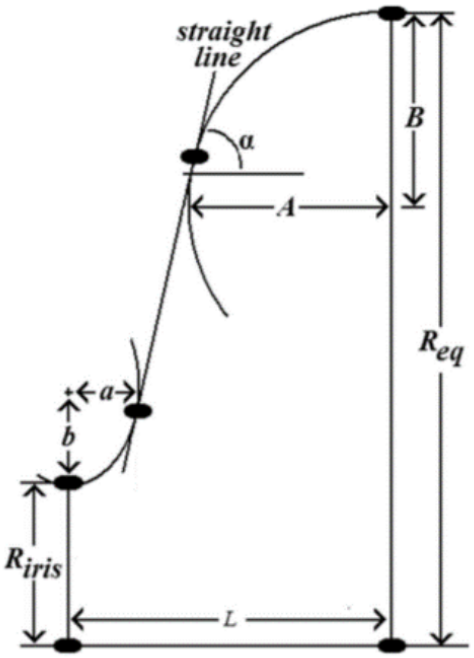

Figure 4.3: Schematic of the elliptical half-cell in POISSON SUPERFISH. Because of the axisymmetric geometry around the centerline, only the upper cross-section is shown.

4.8.1 Parametric Scans

To obtain the parametric scans, a preliminary design of a mid-cell was computed in SUPERFISH. Each geometrical parameter was tuned within realistic limits, and the changes in r/Q, R_sQ, $B_{\max}/E_{\max}$, $E_{\max}/E_0$ were tracked. After finding an optimum for a geometrical parameter, its value was fixed, and the next parameter was scanned. Results for the superconducting 400 MHz cavity from Fig. 4.4 are discussed in this section. All percentage changes were calculated with respect to the lowest computed geometry parameter. The final parameters for the geometry of the SC 400 MHz cavity are included in Table 4.2.

To suppress the HOMs, the bore radius needed to be increased. However, this led to a significant decrease in the quality of several figures of merit. In particular, a reduction of up to 40% of r/Q could be obtained by maximising the bore radius. The second most significant effect was an increase of up to 20% of $B_{\max}/E_{\max}$. To avoid quenching, the bore radius was set to 9 cm, which minimised the change in $E_{\max}/E_0$.

The dome occupies a large section of the cavity volume, where peak fields have the most significant effect. The parametric scans in Fig. 4.4b showed an equal decrease of $B_{\max}/E_{\max}$ and $E_{\max}/E_0$

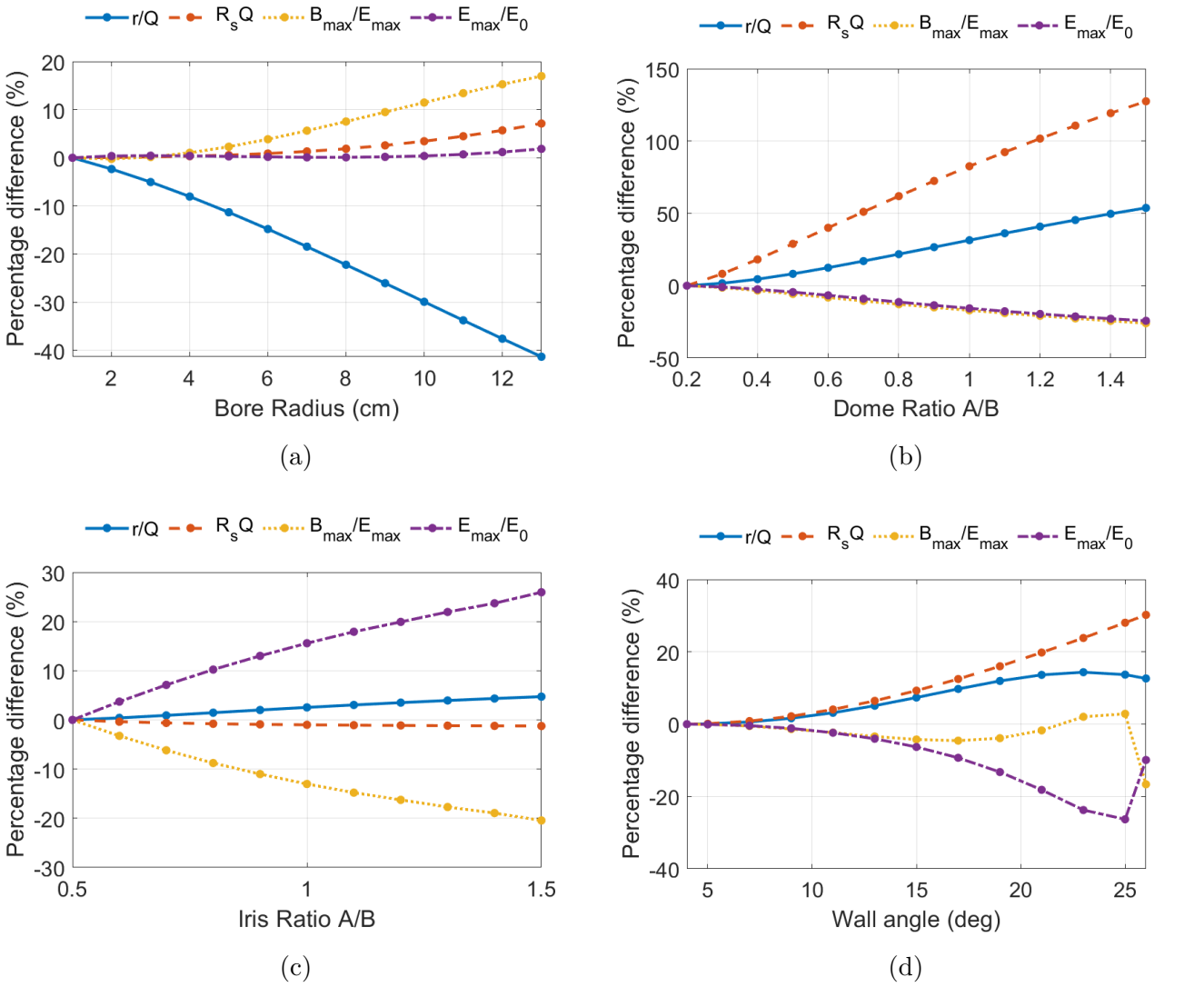

Figure 4.4: Parametric scans of the tunable geometry parameters of an elliptical superconducting cavity: bore radius (a), dome ellipse (b), iris ellipse (c), wall angle (d). The percentage difference is calculated with respect to the lowest value of the geometrical parameter.

from increasing the dome ratio from 0.2 to 1.4. However, decreasing the geometrical parameter also led to a reduction of up to 150% in R_sQ. To avoid this, the dome ratio was increased to 1.2. This choice also allowed for an increase in r/Q by 50%.

The iris is significantly smaller in size than the ellipse dome, which led to a reduction for the change in r/Q and R_sQ. However, the peak fields were also impacted. An increase in the iris ratio corresponds to a decrease of up to 20% of $B_{\max}/E_{\max}$, which can be compensated by an increase in $E_{\max}/E_0$ of up to 25%. To mitigate these effects, and maximise r/Q, the iris ratio was set to 1.5.

Side wall angles from 1° to 25° were considered, since a larger value would induce multipacting. From Fig. 4.4d, an increase in the wall angle corresponds to a rise in r/Q and R_sQ. A break in linearity of the peak fields can be seen for a wall angle of 24°. This value corresponds to the optimum flatness of the cavity surface, which can be used to avoid quenching. Nevertheless, the reduction in $E_{\max}/E_0$ and increase in r/Q and R_sQ was compensated by an increase in $B_{\max}/E_{\max}$, and the wall angle was minimised to 11°.

Parameter	Unit	Value
Length	cm	37.47
Diameter	cm	65.31
Left Dome B	cm	10.5
Right Dome B	cm	8.0
Dome A/B		1.2
Left wall angle	°	11
Right wall angle	°	7.8
Iris a/b		1.5
Bore radius	cm	9.0

Table 4.2: Summary of the geometrical parameters of the 400 MHz elliptical superconducting cavity. The optimisation was performed using SUPERFISH.

Because the positrons are stored in the pDR with a relativistic speed, the impact of the transit time factor was minimal. Simulations showed that the bore radius and wall angle had the most significant impact on the transit time factor, and both parameters would need to be minimised in order to maximise T.

The impact of the bore radius on the transit time factor was determined by adding a beam pipe to the cavity. The change in the field lines was tracked for a bore radius of 5 cm, 9 cm, and 15 cm in Fig.4.5. An extension of the electric field lines into the beam pipe was observed in SUPERFISH, which contributed to a loss in peak fields, cavity frequency, and transit time factor. Note that this effect scales with the size of the bore radius, which determines the volume of the beam pipe, and in turn the dispersion of the electric field lines. To dampen this effect, the bore radius was reduced.

In addition, for a cavity containing more than two cells, the loss in peak fields at the end-cell due to the presence of a beam pipe leads to a degradation in the field flatness of the cavity. This was avoided by reoptimising the outer half-cell to match the peak electric fields of the mid-cell. The cavity diameter was fixed by the mid-cell design, and the tuning of the RF frequency was performed using the horizontal radius of the dome ellipse.

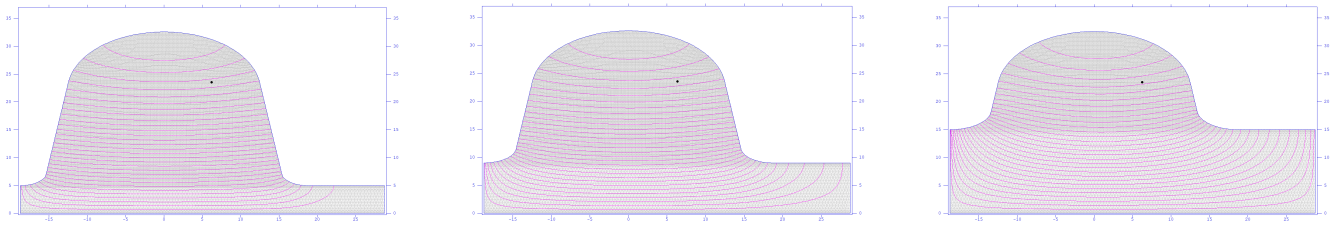

(a) (b) (c)

Figure 4.5: SUPERFISH plots showing the impact of the bore radius on the cavity field lines. An elliptical superconducting cavity of 400 MHz was implemented with a bore radius of 5 cm (a), 9 cm (b), and 15 cm (c).

The 2D model obtained in SUPERFISH was implemented in CST Microwave Studio, which allowed for a robust evaluation of the cavity properties in 3D. The results from CST were bench-marked against SUPERFISH. To achieve this, a tetrahedral mesh was chosen for the 3D model, due to its improved efficiency and in order to match the triangular meshing used in SUPERFISH. The number of mesh cells per wavelength was tuned to ensure a high accuracy.

4.8.2 400 MHz Superconducting Cavity

The results of the geometrical optimisation in SUPERFISH are shown in Table 4.2. Simulations showed that a cavity composed of two cells with an accelerating gradient of 10 MV/m would be able to provide an RF voltage of 7.8 MV, with a geometry factor, R_sQ, of 238.2 Ohms and a Kilpatrick factor of 0.87. The geometry of the mid-cell was found to be similar to the one obtained in a previous study of 400 MHz RF cavities for the FCC [69].

An optimisation of both the mid-cells and end-cells was performed. This allowed for a general design, which could be easily adapted to a cavity with three or more cells. The SUPERFISH design was implemented in CST Microwave Studio, as shown in Fig. 4.6, which allowed for a benchmark of the software.

The percentage difference between figures of merit from SUPERFISH and CST Microwave was determined in Table 4.3. The largest percentage difference was obtained for the peak fields, which was attributed to a lack of implementation in CST of the cavity material.

A comparison of the electric field on axis is shown in Fig. 4.7. The regions of interest were the tip of the fields, also used to evaluate the field flatness, and the field at the edge of the cavity. To match the results from SUPERFISH, where the field lines are set to 0 at the edge, the length of the beam pipe was increased until the electric field on axis at the edge of the cavity was negligible.

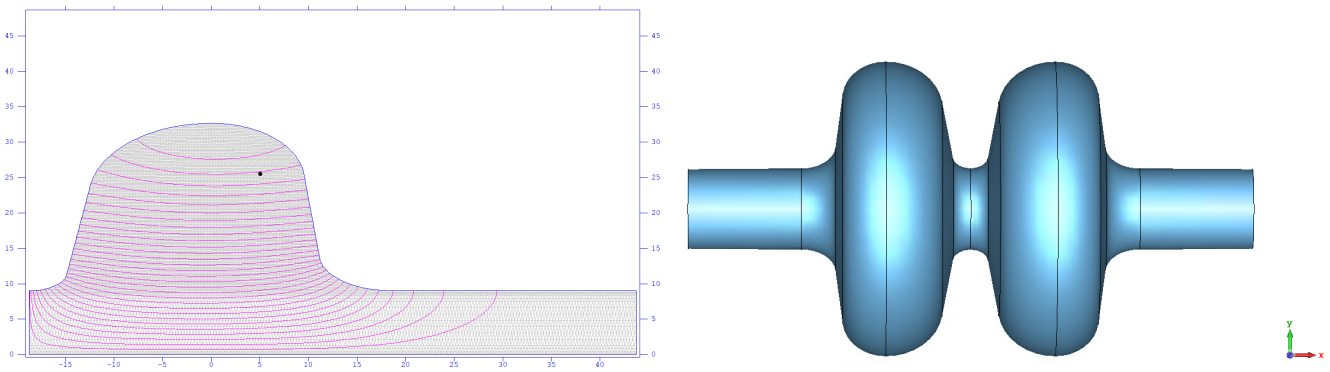

(a) (b)

Figure 4.6: Model of the two-cell 400 MHz elliptical superconducting cavity for the pDR. A half-cell is shown in SUPERFISH (a), and the full cavity in CST Microwave (b).

Parameter	Unit	Superfish	CST	Percentage difference (%)
Frequency	MHz	399.682	399.677	0.03
r/Q	Ω	134.206	134.228	0.01
T		0.7280	0.7279	0.02
RF voltage	MV	7.499	7.502	0.03
$E_{\max}$	MV/m	16.904	16.870	0.20
$H_{\max}$	A/m	25562.2	25565.0	0.01

Table 4.3: Figures of merit obtained for the 400 MHz elliptical superconducting cavity.

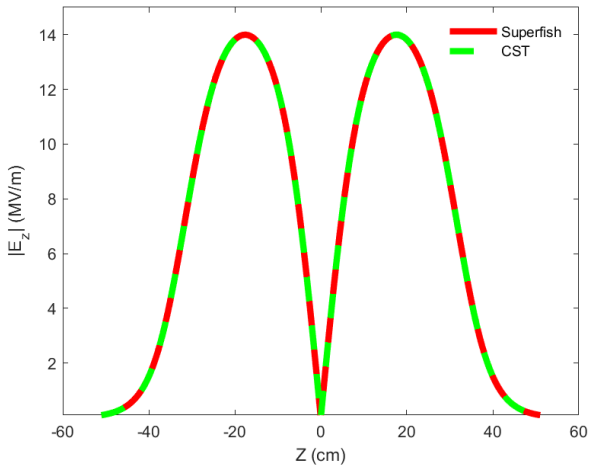

Figure 4.7: Comparison of the electric field on axis from SUPERFISH and CST of the 400 MHz superconducting cavity.

4.8.3 800 MHz Superconducting Cavity

This section discusses the design of the 800 MHz cavity in SUPERFISH. The optimised cavity is then implemented in CST for comparison.

	Unit	Design 1	Design 2
Length	cm	18.737	18.737
Diameter	cm	36.081	34.798
Left Dome B	cm	6.500	6.200
Right Dome B	cm	3.289	4.470
Dome A/B		1.200	1.1
Left wall angle	°	20.000	18.000
Right wall angle	°	20.000	18.000
Iris A/B		0.500	0.500
Bore radius	cm	9.000	7.500

Table 4.4: Summary of 800 MHz SUPERFISH cavity design parameters.

	Unit	Design 1	Design 2
Frequency	MHZ	800.051	799.999
$B_{\max}/E_{\max}$	mT/(MV/m)	1.009	1.8643
$E_{\max}/E_0$		3.645	1.8633
r/Q	Ω	98.960	125.656
R_sQ	Ω	298.057	284.096
T		0.634	0.648
the Killpatric		0.701	0.717
# of cells		3	3

Table 4.5: Comparison of two 800 MHz SUPERFISH cavity designs.

Table 4.4 and Table 4.5 illustrate the geometries and key figures of merit of two optimised SUPERFISH cavity designs. Both cavities have a 10 MV/m acceleration gradient. In Design 1, minimisation of $B_{\max}/E_{\max}$ is prioritised. This is achieved at the cost of a high E_{max} to E_0 ratio. For the second design, both ratios are minimised. Here, $B_{\max}/E_{\max}$ and $E_{\max}/E_0$ shows opposite trend, so this is essentially a compromise between the two parameters. Both designs require 3 cavities to reach the required voltage. They all meet the space requirements for the RF cavities. As illustrated by Fig. 4.8, in design 1 the dome radius of the edge cell is varied too far from the

mid-cell dome radius. The high degree of the asymmetry might pose technical difficulties for manufacturing. Additionally, design 2 shows better performance apart from with regards to $B_{\max}/E_{\max}$ and R_sQ.

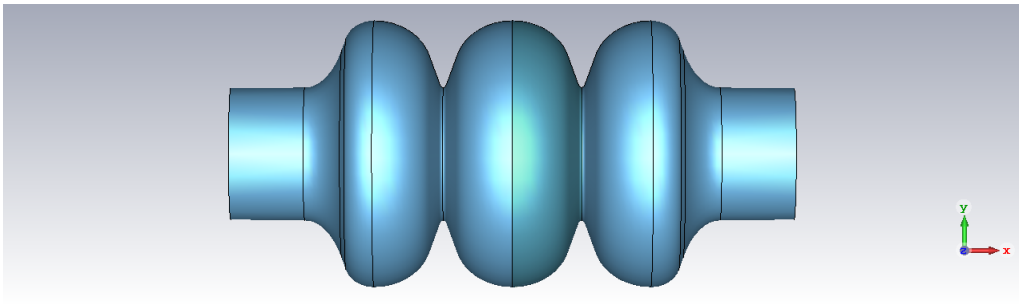

Figure 4.8: 800 MHz 3 cell cavity (Design 1)

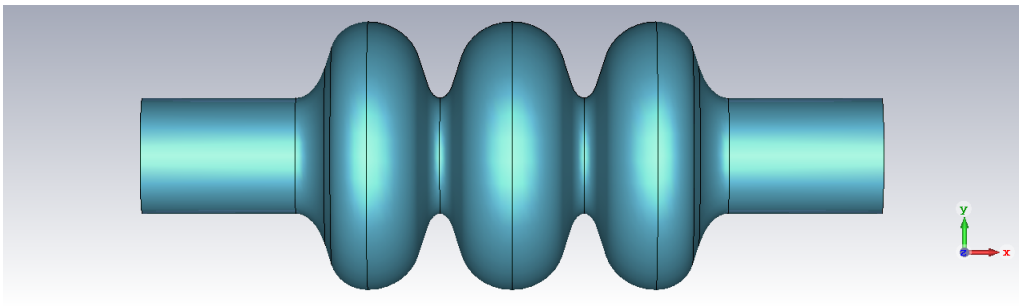

Figure 4.9: 800 MHz 3 cell cavity (Design 2)

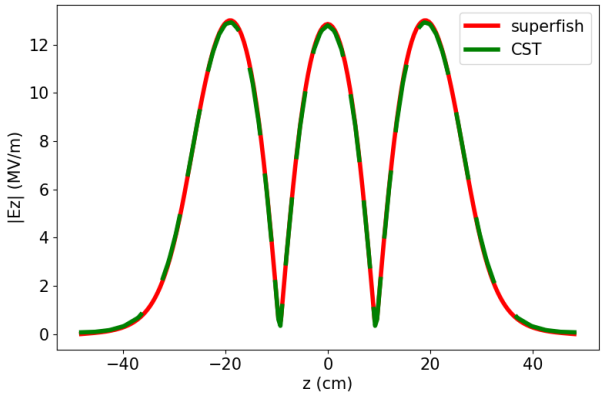

Figure 4.10: 800 MHz 3 cell cavity field on axis

Design 2 was then implemented in CST for comparison. Table 4.6 compares CST and SUPERFISH results. Apart from the maximum of the fields, CST and SUPERFISH show good agreement. This is further supported Fig. 4.8, which compares the field on axis. The large difference in the peak fields is due to the different approaches for computing the boundary conditions. In CST the cavity

is assumed to be a perfect electric conductor, whereas in SUPERFISH the material property is taken into account via critical temperature and residual resistance.

Parameter	Unit	SUPERFISH	CST	error
Frequency	MHZ	799.999	799.834	$< 1\%$
r/Q	Ω	125.656	125.745	$< 1\%$
T		0.648	0.647	$< 1\%$
RF Voltage	MV	5.622	5.623	$< 1\%$
$E_{\max}$	MV/m	18.633	19.502	5%
$H_{\max}$	A/m	27643	25776	7%

Table 4.6: Comparison of CST and SUPERFISH figures of merit for 800 MHz 3 cell cavity.

4.9 Optimisation of the Normal-Conducting Cavity

This section is going to provide details on how the optimisation of a 400 MHz side-coupled normal-conducting cavity was performed. Two software packages were used: SUPERFISH for the initial 2D optimisation, and CST Microwave Studio for the 3D modelling.

Similarly to what was done for the superconducting cavities, the aim of the 2D geometry optimisation stage was to produce a design which minimised both the peak magnetic $B_{\max}$ and electric $E_{\max}$ fields, and $B_{\max}/E_{\max}$. It was also important to minimise the electric field gradient $E_{\max}/E_0$ and maximise both R_sQ and r/Q. Keeping in mind that this was a NC cavity, the E_0 had to be lower than 3 MV/m and the Kilpatrick factor lower than 1.5.

Figure 4.11 shows an example of side-coupled half cell geometry, the tunable parameters are labelled on the schematic. In order to fully define a cavity one needs to set the bore radius R_{bore}, the length $2L$, the cavity radius R_{eq}, the inner and outer corner radii R_{ic}, R_{oc}, the inner and outer nose radii R_{in}, R_{on}, the flat length and the nose angle α.

The diameter of the cavity was tuned using Eq. 4.10 and since the cavity mode is π, the length was determined by Eq. 4.11. Changing the R_{bore} affects the $B_{\max}/E_{\max}$ ratio and the transit time factor.

The cavity would have to be inserted in the pDR by means of a beam pipe but designing this was not straightforward so, due to the time constraints on the project, this will be part of the future work. Similarly there was not enough time to optimise a multiple cavity design due to the non

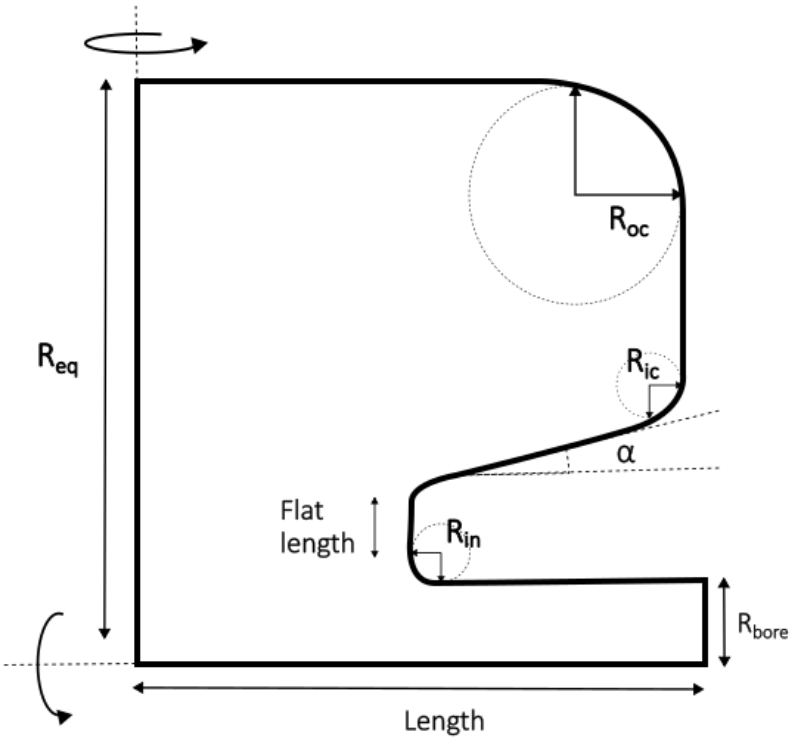

Figure 4.11: Schematic of the NC side-coupled half-cell in Poisson SUPERFISH.

trivial side-coupling structures needed.

Changing any of the geometrical parameters had an effect on the cavity performance, the various relationships between the input parameters and the outputs were analysed much in the same way as described in Section 4.8.1, i.e. producing parametric scans. In particular it was observed that increasing R_{ic}, R_{oc}, R_{in}, R_{on} lowered the peak electric field value, hence reducing the electric field gradient but increasing the value of $B_{\max}/E_{\max}$.

Increasing either the flat length or α lowered the $B_{\max}/E_{\max}$ ratio, but at the expense of the field flatness.

Changing the bore radius affected the transit time factor, in particular decreasing R_{bore} produced an increase in the transit time factor. In order to properly investigate this relationship, ideally a beam pipe should have been added, but as mentioned above this was not possible.

All the relationships between the geometrical parameters and the cavity performance parameters were taken into account to reach a final cavity design. The optimised input and output parameters are summarised in Tables 4.7 and 4.8.

Once the 2D optimisation was completed, the same cavity was modelled in 3D using CST Microwave Studio. The aim for this step was to match the cavity performance parameters already

Parameter	Unit	Value
Length	cm	18.75
Diameter	cm	47.84
Outer corner radius	cm	3.0
Inner corner radius	cm	1.0
Outer nose radius	cm	1.0
Inner nose radius	cm	1.0
Flat length	cm	4.0
Cone angle	°	30
Bore radius	cm	6.0

Table 4.7: Summary of the geometrical parameters of the 400 MHz side-coupled normal-conducting cavity. The optimisation was performed using SUPERFISH.

Parameter	unit	value
Frequency	MHZ	400.002
$B_{\max}/E_{\max}$	mT/(MV/m)	1.350
$E_{\max}/E_0$		2.999
r/Q	Ω	108.870
R_sQ	Ω	170.250
T		0.806
Kilpatric		0.460

Table 4.8: Performance parameters for the normal-conducting cavity obtained using SUPERFISH

obtained in SUPERFISH. The mesh used was tetrahedral and set to be adaptive.

4.9.1 400 MHz Normal-Conducting Cavity

The results of both the 2D and 3D optimisation of the normal-conducting cavity will be presented in this section. Tables 4.7 and 4.8 display respectively the input and the key figures of merit of the 2D SUPERFISH simulation. The accelerating gradient for this cavity was of 3 MV/m, which is the highest value supported by normal-conducting cavities, but is significantly lower than the gradients of 10 MV/m set for the superconducting cavities. In order to reach the overall voltage requirement of 4 MV, four cavities like the one presented would be needed, hence narrowly surpassing the 1.5 m length limit for the overall cavity.

The optimised single cavity 2D design was implemented in CST Microwave studio, the resulting 3D cavity is shown in Fig. 4.12 and the figures of merit obtained in 3D were bench-marked against the 2D ones as shown in Table 4.8. The electric fields on axis were plotted for the 2D and 3D case as shown in Fig. 4.13.

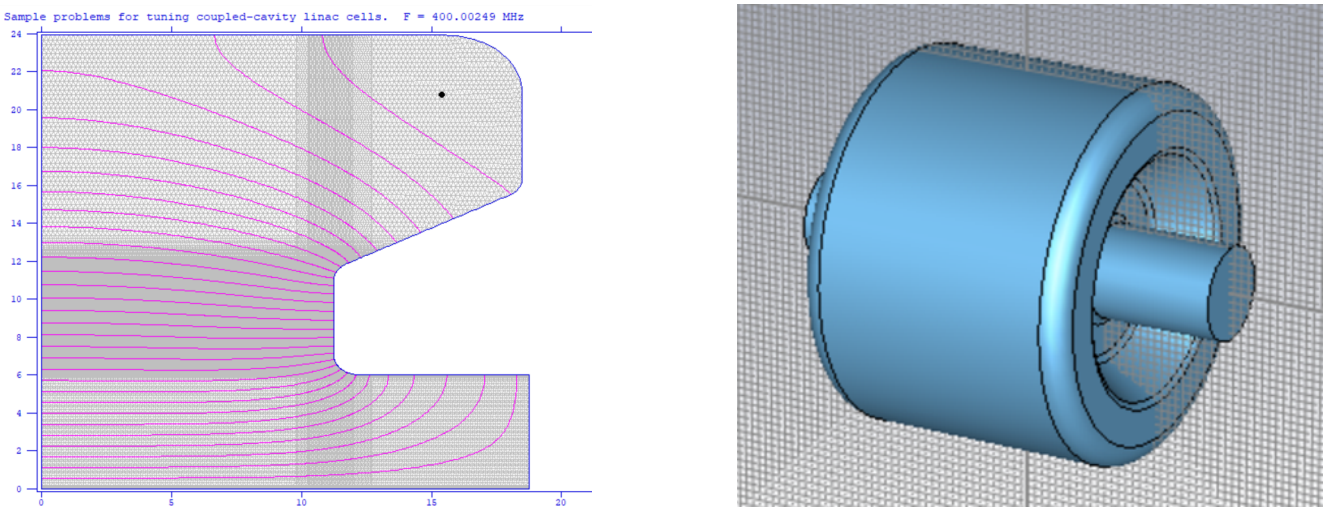

(a) (b)

Figure 4.12: Model of the single-cell 400 MHz side-coupled, normal-conducting cavity for the pDR. A half-cell is shown in SUPERFISH (a), and the full, single-cell, cavity in CST Microwave (b).

Parameter	SUPERFISH	CST	error
Frequency (MHZ)	400.002	399.956	$< 1\%$
r/Q (Ω)	108.870	109.040	$< 1\%$
T	0.787	0.807	2.4%
RF Voltage (MV)	1.116	1.142	2.3%
$E_{\max}$ (MV/m)	8.933	10.220	14.4%
$H_{\max}$ (A/m)	9599	9623	$< 1\%$

Table 4.9: Comparison of CST and SUPERFISH figures of merit for 400 MHz normal-conducting single-cell cavity

The 14.4% discrepancy between the peak electric fields in 2D and 3D is justified by the fact that CST did not allow the user to set the material properties for the cavity walls whereas SUPERFISH did, hence in the 3D model the resistive effects (particularly important in a normal-conducting cavity) were not taken into account. The 2.4% percentage difference in transit time values can be explained by recalling that, as anticipated in Section 4.9, the 2D design did not include a beam pipe, whereas the 3D one does and that the beam pipe strongly affects the transit time factor.

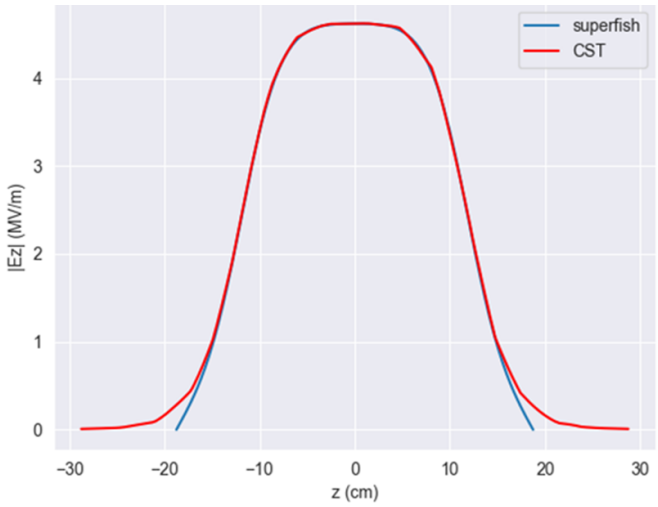

Figure 4.13: Comparison of the electric field on-axis from SUPERFISH and CST of the 400 MHz normal-conducting cavity.

This same flaw in our 2D design causes the plots of the fields on axis for the 2D and 3D case to not match perfectly in the region of electric field close to zero.

4.9.2 Comparison

We presented three different designs of the RF cavities. In this section the cavities are compared with respect to their figures of merit, as well as other relevant factors in their suitability for implementation in the FCCee injector complex.

Four cells are required for the 400 MHz normal-conducting cavity, constituting a total length of 1.5 m. Considering the beam pipes and damping structures, this design will not meet the space requirement of 1.5 m. Furthermore, normal conducting cavities dissipate much more power compared to superconducting cavities, making them less efficient. Therefore, superconducting cavities are the superior choice for the pDR.

The diameter of the cavity is inversely proportional to the resonance frequency, making each cell of the 800 MHz approximately half the size of the 400 MHz cavity. The length for the 800 MHz and the 400 MHz cavities is 0.56 m and 0.75 m, respectively. Though more space is required for 800 MHz cavity, they both satisfy the space limitation, However, a small diameter means that the transient time factor is heavily influenced by the geometry. Fig. 4.14 shows that for the 800 MHz cavity the minimisation of the field ratios is achieved at the expense of a lower transient time factor. Most significantly, the 400 MHz is widely available from the LHC [63]. The mature design and the high acceleration efficiency makes 400 MHz the appropriate choice for the task.

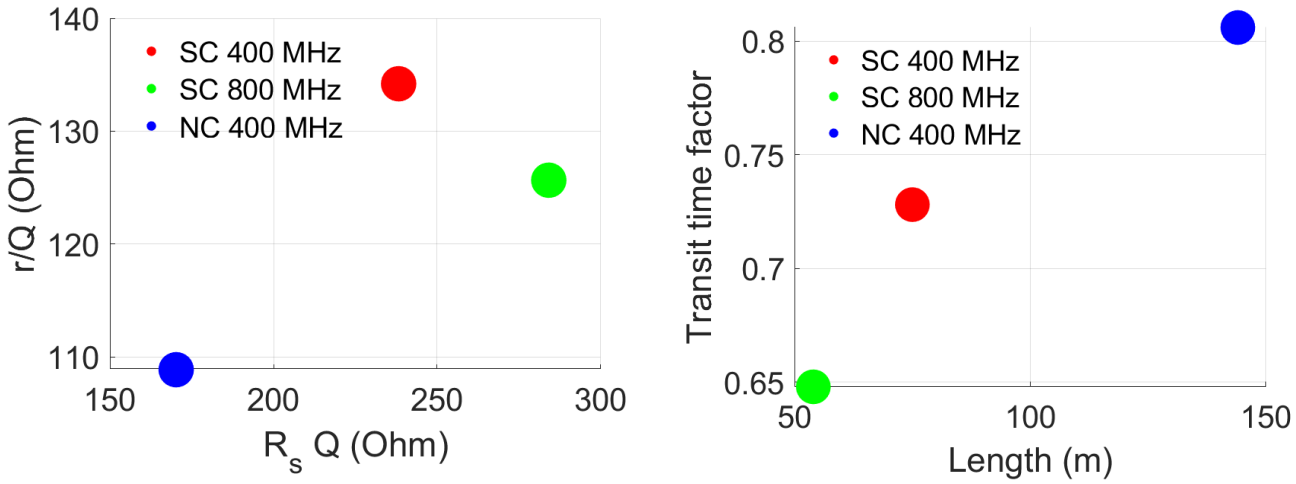

(a) (b)

Figure 4.14: Comparison of cavity performance: r/Q v.s. R_sQ (a), transit time factor vs length (b).

4.10 Conclusions

Based on the figures of merit defined in Section 4.4 and the availability of 400 MHz technology, the recommended RF cavity for the FCCee pDR is the 400 MHz superconducting cavity described in Section 4.8.2.

Normal-conducting cavities were considered not to be ideal for the damping ring, because of the size constraint and high power dissipation.

Out of four figures of merit (length, transit time factor, geometrical factor, r/Q), the 400 MHz cavity outperforms the 800 MHz cavity on two: r/Q and transit time factor. The 800 MHz cavity outperforms the 400 MHz cavity on the other two: length and geometrical factor.

The preference for 400 MHz superconducting technology was given due to its availability, since 800 MHz cavities have more novel designs, which have not yet been integrated in the CERN accelerator complex.

4.11 Further work

For both the normal-conducting and superconducting cavities, a more detailed study of the secondary effects, e.g. multipacting, beam loading, beam break-up, and field emission, will be needed. The analysis would require the use of additional software, or of additional features provided by SUPERFISH or CST.

4.11.1 Superconducting cavities

There are several areas of further work that could be pursued related to cryomodules and higher order mode (HOM) coupler configurations for RF cavities in the FCC at CERN.

While cryomodules are currently employed in the FCCee, there may be opportunities to further optimise their design for improved efficiency and reliability. This could involve exploring alternative materials, such as niobium-tin or niobium-titanium alloys, or investigating new cooling technologies.

HOM couplers are critical components in RF cavities, as they are responsible for removing unwanted energy from the cavities that can cause instabilities in the beam by inducing field lines that do not contribute to acceleration. Further work could be done to optimise the design and placement of these couplers to minimise losses and improve their efficiency.

For the 400 MHz superconducting cavity, the two cell configuration ensures a good field flatness. A more symmetric design for the end-cell could therefore be conceived, which would simplify production.

4.11.2 Normal-conducting cavities

For the normal-conducting cavity, two main improvements can be made to the design: adding the beam pipe in SUPERFISH and extending the single cell cavity to the full four cell cavity. In order to produce the multi-cell cavity the individual cells would need to be side-coupled via specific coupling structures to be implemented in SUPERFISH.

Furthermore, since one of the problems with the 400 MHz normal-conducting option was the total length occupied by the full four cell cavity, one could try modelling a 800 MHz alternative which would be more compact.

Chapter 5

Conclusion

In this report we have presented a preliminary design study for the FCCee pDR and transfer line. The three areas of focus were: designing a bunch compressor for the transfer line, designing magnets for the the pDR and designing RF cavities for the pDR.

The lattice section presented two different bunch compressor designs: dog-leg and C-bend. The C-bend design provides sufficient and tunable bunch compression, but has a large footprint. Around 75 m of additional tunnel would be needed for this design. The dog-leg design also provides sufficient bunch compression with a smaller footprint, but introduces chromatic effects that must be compensated for.

The magnets section presented and evaluated the designs for a dipole, quadrupole, sextupole, wiggler, kicker and septum. The magnetostatic performance of all magnets was evaluated using 2D models. Both electromagnetic and permanent magnet designs were explored for the wiggler, whereas for the other magnets just one design was optimised. All the designs provided sufficient good field regions, apart from the wiggler, which had too many edge effects to model a good field region in 2D.

The RF section presented three different cavity designs: 400 MHz superconducting, 400 MHz normal conducting and 800 MHz superconducting. The recommended design is the 400 MHz superconducting cavity, because its high quality factor and the availability of superconducting technology and corresponding expertise at CERN.

Following this preliminary study, all aspects of the accelerator analysed in this project require further optimisation.

Further research into the impact of the bunch compressor designs on beam energy, emittance and

chromaticity would inform the choice of design and compensations needed. The bunch compressor also requires a new RF cavity design.

For the magnets, the principal next step would be to model the designs in 3D to take into account edge effects. A materials study could be undertaken to determine the best materials to use in terms of performance, cost and energy efficiency. Permanent magnet designs for the magnets other than the wiggler (already explored) and kicker (requires ramping) could also be explored.

The RF cavities could be further optimised to increase field flatness. More detailed studies of the secondary effects should be undertaken. For the superconducting cavities, further research could also be done into alternative materials and cryo-cooling systems.

References

[1] *Hilary Term 2023 (19 January 2023 - 9 March 2023) · Indico*. [Online]. Available: https://indico.cern.ch/event/1230947/timetable/#day-2023-03-09.

[2] *JAI Advisory Board (27-28 March 2023): Contribution List · Indico*. [Online]. Available: https://indico.cern.ch/event/1262793/contributions/.

[3] A. Abada, M. Abbrescia, S. AbdusSalam, *et al.*, "Fcc-ee: The lepton collider: Future circular collider conceptual design report volume 2," *The European Physical Journal Special Topics*, vol. 228, pp. 261–623, 2019.

[4] C. Grojean, *FCC Physics Case: the once, the now, the future*, May 2022. [Online]. Available: https://indico.cern.ch/event/1064327/contributions/4893259/attachments/2452515/4432967/Grojean_FCCWeek_2022_05_30_eu.pdf.

[5] C. Biscari, L. Rivkin, P. Burrows, and F. Zimmermann, "Open Symposium towards updating the European Strategy for Accelerators summary," in *European Strategy Update*, Grenada, May 2019.

[6] *Linear collider plans move forward — symmetry magazine*. [Online]. Available: https://www.symmetrymagazine.org/article/february-2013/linear-collider-plans-move-forward.

[7] T. Raubenheimer and F. Zimmerman, *Accelerator Overview*, Paris, May 2022.

[8] O. Brüning, A. Seryi, and S. Verdú-Andrés, "Frontiers : Electron-Hadron Colliders: EIC, LHeC and FCC-eh," *Front. Phys.*, vol. 10, p. 886 473, Apr. 2022, ISSN: 2296424X. DOI: 10.3389/FPHY.2022.886473. [Online]. Available: https://cds.cern.ch/record/2811194.

[9] P. Craievich, *(Pre-)Injector Layout and Parameter Summary*, Paris, May 2022.

[10] B. Dalena, A. Chance, B. Dalena, B. Haerer, and H. de Grandsaignes, *Optics studies for the FCC-ee Booster ring: status and plan*, Jan. 2021. [Online]. Available: www.cea.fr.

[11] T. Raubenheimer, P. Emma, and S. Kheifets, "Chicane and wiggler based bunch compressors for future linear colliders," in *Proceedings of International Conference on Particle Accelerators*, IEEE, 1993, pp. 635–637.

[12] A. Wolski, "A short introduction to bunch compressors for linear colliders," *Notes for USPAS Course on Linear Colliders, Santa Barbara*, 2003.

[13] D. C. Nguyen, J. W. Lewellen IV, and L. D. Duffy, "Rf linac for high-gain fel bunch compression," Jun. 2014. [Online]. Available: https://uspas.fnal.gov/materials/14UNM/E_Bunch_Compression.pdf.

[14] S. D. Mitri, "Bunch length compressors," *CERN Yellow Reports: School Proceedings*, vol. 1, pp. 363–363, 2018 Apr. 2018, ISSN: 2519-805X. DOI: 10.23730/CYRSP-2018-001.363. [Online]. Available: https://e-publishing.cern.ch/index.php/CYRSP/article/view/392.

[15] T. Charles, M. Boland, K. Oide, and F. Zimmermann, "Bunch compression and turnaround loops in the fcc-ee injector complex," *Journal of Physics: Conference Series*, vol. 1067, p. 062 023, Sep. 2018. DOI: 10.1088/1742-6596/1067/6/062023.

[16] A. Sharma, "Optics design and optimisation of electron bunch compressor transfer line (with a case study of ctf3 bunch compressor)," Raja Ramanna Centre for Advanced Technology, 2013.

[17] R. R. et al. "Pdr.madx." (2022), [Online]. Available: https://indico.cern.ch/event/1230947/sessions/471591/#20230126.

[18] H. Grote, F. Schmidt, L. Deniau, and G. Roy, *The mad-x program (methodical accelerator design) version 5.02.08 user's reference manual*, EUROPEAN LABORATORY FOR PARTICLE PHYSICS, Mar. 2016. [Online]. Available: http://mad.web.cern.ch/mad/releases/5.02.08/madxuguide.pdf.

[19] W. Lau, M.-C. Chou, N.-Y. Huang, A.-p. Lee, and J. Wu, "Design of a Dogleg Bunch Compressor with Tunable First-Order Longitudinal Dispersion," TUP031, 2018. DOI: 10.18429/JACoW-FEL2017-TUP031.

[20] H. G. Morales, *John adams institute: Transverse dynamics lectures*, Oct. 2022. [Online]. Available: https://indico.cern.ch/event/1192266/sessions/455351/#all.

[21] A. Milanese, *John adams institute lecture notes: An introduction to magnets for accelerators*, Jan. 2023. [Online]. Available: https://indico.cern.ch/event/1230947/sessions/471586/#20230119.

[22] M. Benedikt, V. Mertens, F. Zimmermann, *et al.*, "Fcc-ee: The lepton collider: Future circular collider conceptual design report volume 2," *Eur. Phys. J. Spec. Top.*, vol. 228, no. CERN-ACC-2018-0057, pp. 261–623, 2018.

[23] T. J. Hughes, *The finite element method: linear static and dynamic finite element analysis*. Courier Corporation, 2012.

[24] D. Meeker *et al.*, "Finite element method magnetics," *FEMM*, vol. 4, no. 32, p. 162, 2010.

[25] C. Conejo Rodriguez, "Fem calculations current flow for submerged arc furnaces and eddy currents-heat transfer for power cables," M.S. thesis, 2013.

[26] D. Meeker, *Finite element method magnetics: Pyfemm user's manual*, 2018.

[27] C. R. Harris, K. J. Millman, S. J. van der Walt, *et al.*, "Array programming with NumPy," *Nature*, vol. 585, no. 7825, pp. 357–362, Sep. 2020. DOI: 10.1038/s41586-020-2649-2. [Online]. Available: https://doi.org/10.1038/s41586-020-2649-2.

[28] R. Chartrand, "Numerical differentiation of noisy, nonsmooth data," *ISRN Appl. Math.*, vol. 2011, Jan. 2011. DOI: 10.5402/2011/164564.

[29] *scipy.signal.butter — SciPy v1.10.1 Manual*. [Online]. Available: https://docs.scipy.org/doc/scipy/reference/generated/scipy.signal.butter.html.

[30] P. Virtanen, R. Gommers, T. E. Oliphant, *et al.*, "SciPy 1.0: Fundamental Algorithms for Scientific Computing in Python," *Nature Methods*, vol. 17, pp. 261–272, 2020. DOI: 10.1038/s41592-019-0686-2.

[31] "TYPES OF ACTIVE FILTERS," [Online]. Available: http://www.circuitstoday.com/active-filter-types.

[32] stur86, *Tvregdiff*, https://github.com/stur86/tvregdiff, 2018.

[33] A. Ghaith, D. Oumbarek, C. Kitégi, M. Valléau, F. Marteau, and M.-E. Couprie, "Permanent magnet-based quadrupoles for plasma acceleration sources," *Instruments*, vol. 3, no. 2, p. 27, 2019.

[34] P. Lebrun, "Interim Summary Report on the Analysis of the 19 September 2008 Incident at the LHC," *CERN EDMS document*, vol. 973073, 2008.

[35] *Hollow conductors*. [Online]. Available: https://www.luvata.com/products/hollow-conductors.

[36] J. Bauche and A. Aloev, "Design of the beam transfer line magnets for hie-isolde," *5th International Particle Accelerator Conference*, pp. 1289–1291, 2014. [Online]. Available: https://commons.wikimedia.org/wiki/File:Magnetic_field_of_an_idealized_sextupole.svg.

[37] W. Hillert, *Transverse linear beam dynamics*, 2021. arXiv: 2107.02614 [physics.acc-ph].

[38] S. Guiducci, "Chromaticity, frascati national laboratories-infn, frascati, italy," *URL: https://s3.cern. ch/inspire-prod-files-d/d799d74f3e0c9c019759e315d479c931*,

[39] C. Doose and A. Jain, "Aps-u definitions of signs and conventions related to magnets," Argonne National Lab.(ANL), Argonne, IL (United States), Tech. Rep., 2014.

[40] W. Commons. "Magnetic field of an idealized sextupole." (2012), [Online]. Available: https://commons.wikimedia.org/wiki/File:Magnetic_field_of_an_idealized_sextupole.svg.

[41] M. Fraser, *Injection, Beam Transport and Extraction*, Feb. 2023. [Online]. Available: https://indico.cern.ch/event/1230947/sessions/471587/#20230216.

[42] M. Barnes, *Kicker Systems - Part 1 - Introduction and Hardware*, Mar. 2017. [Online]. Available: https://cas.web.cern.ch/sites/default/files/lectures/erice-2017/barnesi.pdf.

[43] F. Bordry, L. Bottura, A. Milanese, D. Tommasini, and et al, "Accelerator Engineering and Technology: Accelerator Technology," in *Particle Physics Reference Library : Volume 3: Accelerators and Colliders*, S. Myers and H. Schopper, Eds. Cham: Springer International Publishing, 2020, pp. 337–517, ISBN: "978-3-030-34245-6". DOI: "10.1007/978-3-030-34245-6_8". [Online]. Available: https://doi.org/10.1007/978-3-030-34245-6_8.

[44] I. Martin, *Lecture 3 Radiation Damping Contents*, 2022.

[45] I. Martin, *Michaelmas Term 2022 (12 October 2022 - 1 December 2022): Lecture 15 - Undulators & Wigglers · Indico*, Nov. 2022. [Online]. Available: https://indico.cern.ch/event/1192266/contributions/5012570/.

[46] *AISI 1020 Low Carbon/Low Tensile Steel*. [Online]. Available: https://www.azom.com/article.aspx?ArticleID=6114.

[47] *Ferrite Magnet Price Trends - Bunting - Berkhamsted*. [Online]. Available: https://www.bunting-berkhamsted.com/ferrite-magnet-price-concerns/.

[48] A. B. C. G. S. 1989. "Armco soft iron, sheet metal." (), [Online]. Available: https://www.anodefactory.com/products/armco-jarn-plat-2000-1000-10mm?variant=43722096148730.

[49] B. UK. "10kg spools." (), [Online]. Available: https://brocott.co.uk/10kg-spools/.

[50] *Opera — SIMULIA by Dassault Systèmes®*, 2023. [Online]. Available: https://www.3ds.com/products-services/simulia/products/opera/.

[51] *SIMION® Ion and Electron Optics Simulator*, 2020. [Online]. Available: https://simion.com/.

[52] S. Ogur, T. Charles, K. Oide, *et al.*, "Layout and performance of the FCC-ee pre-injector chain," *Journal of Physics: Conference Series*, vol. 1067, no. 2, p. 022 011, Sep. 2018. DOI: 10.1088/1742-6596/1067/2/022011. [Online]. Available: https://dx.doi.org/10.1088/1742-6596/1067/2/022011.

[53] A. Hofmann, *The physics of synchrotron radiation* (Cambridge monographs on particle physics, nuclear physics, and cosmology). Cambridge: Cambridge Univ. Press, 2004. DOI: 10.1017/CBO9780511534973. [Online]. Available: https://cds.cern.ch/record/712871.

[54] A. De Santis, C. Milardi, R. Ramjiawan, and Y. Dutheil, "FCC-ee injector: Positron damping ring design status," FCC Week, 2022.

[55] M. Benedikt, A. Blondel, O. Brunner, *et al.*, "FCC-ee: The Lepton Collider: Future Circular Collider Conceptual Design Report Volume 2. Future Circular Collider," CERN, Geneva, Tech. Rep. 2, 2019. DOI: 10.1140/epjst/e2019-900045-4. [Online]. Available: https://cds.cern.ch/record/2651299.

[56] E. Jensen, "RF Cavity Design," 2014, Comments: 25 pages, contribution to the CAS - CERN Accelerator School: Advanced Accelerator Physics Course, Trondheim, Norway, 18-29 Aug 2013. DOI: 10.5170/CERN-2014-009.405. [Online]. Available: http://cds.cern.ch/record/1982429.

[57] K. Halbach and R. F. Holsinger, "SUPERFISH - a computer program for evaluation of rf cavities with cylindrical symmetry," *Part. Accel.*, vol. 7, pp. 213–222, 1976. [Online]. Available: https://cds.cern.ch/record/700607.

[58] "CST MicroWave Studio." (2022), [Online]. Available: https://www.3ds.com/products-services/simulia/products/cst-studio-suite. (accessed: 15.03.2023).

[59] T. P. Wangler, *Principles of RF linear accelerators* (Wiley series in beam physics and accelerator technology), eng. New York ; Chichester: Wiley, 1998, ISBN: 9780471168140.

[60] W. D. Kilpatrick, "A criterion for vacuum sparking designed to include both RF and DC," Apr. 1957. [Online]. Available: https://escholarship.org/uc/item/3rs8w60.

[61] H. Podlech, *Superconducting versus normal conducting cavities*, en, 2013. DOI: 10.5170/CERN-2013-001.151. [Online]. Available: http://cds.cern.ch/record/1533028.

[62] A. Gurevich, "Theory of RF superconductivity for resonant cavities," *Supercond. Sci. Technol.*, vol. 30, no. 3, p. 034 004, 2017. DOI: 10.1088/1361-6668/30/3/034004. [Online]. Available: https://iopscience.iop.org/article/10.1088/1361-6668/30/3/034004.

[63] D. Boussard, E. Chiaveri, E. Haebel, *et al.*, "LHC superconducting cavities," vol. 2, 1999.

[64] A. Gamp, "Beam loading," 2013, Comments: 25 pages, contribution to the CAS - CERN Accelerator School: Course on High Power Hadron Machines; 24 May - 2 Jun 2011, Bilbao, Spain. DOI: 10.5170/CERN-2013-001.117. arXiv: 1303.1358. [Online]. Available: https://cds.cern.ch/record/1524062.

[65] J. Le Duff, "Beam break up," 1987. DOI: 10.5170/CERN-1987-003-V-2.610. [Online]. Available: https://cds.cern.ch/record/165944.

[66] R. Prakash, A. R. Jana, and V. Kumar, "Multipacting studies in elliptic SRF cavities," eng, *Nuclear instruments & methods in physics research. Section A, Accelerators, spectrometers, detectors and associated equipment*, vol. 867, pp. 128–138, 2017, ISSN: 0168-9002.

[67] B. Bonin, "Field emission in RF cavities," 1996. DOI: 10.5170/CERN-1996-003.221. [Online]. Available: http://cds.cern.ch/record/399571.

[68] P. Tavares, F. Cullinan, Å. Andersson, D. Olsson, and R. Svärd, "Beam-based characterization of higher-order-mode driven coupled-bunch instabilities in a fourth-generation storage ring," *Nuclear Instruments and Methods in Physics Research Section A: Accelerators, Spectrometers, Detectors and Associated Equipment*, vol. 1021, p. 165 945, 2022, ISSN: 0168-9002. DOI: https://doi.org/10.1016/j.nima.2021.165945. [Online]. Available: https://www.sciencedirect.com/science/article/pii/S0168900221009025.

[69] S. Gorgi Zadeh, "Accelerating cavity and higher order mode coupler design for the Future Circular Collider," Presented 15 Mar 2021, 2021. [Online]. Available: https://cds.cern.ch/record/2776785.

[70] B. Aune, R. Bandelmann, D. Bloess, *et al.*, "The Superconducting TESLA Cavities," *Phys. Rev. Spec. Top. Accel. Beams*, vol. 3, p. 092 001, 2000, Dedicated to the memory of Bjorn H. Wiik. DOI: 10.1103/PhysRevSTAB.3.092001. [Online]. Available: https://cds.cern.ch/record/429906.

Appendix A

A.1 Sextupole Sensitivity Test Results

Plots showing the variation of the mean and standard deviation of the second derivative of the field strength are shown below. The first 15 parameters shown are all for the same default magnet configuration discussed above. For this test, the number of coils was not varied, as it had been decided to hold fixed due to considerations on the number of coils (laid out in 3.1.7). An example for a different trial magnet is shown to show the expected linear relationship of mean second derivative with number of coils (while outside the saturated regime).

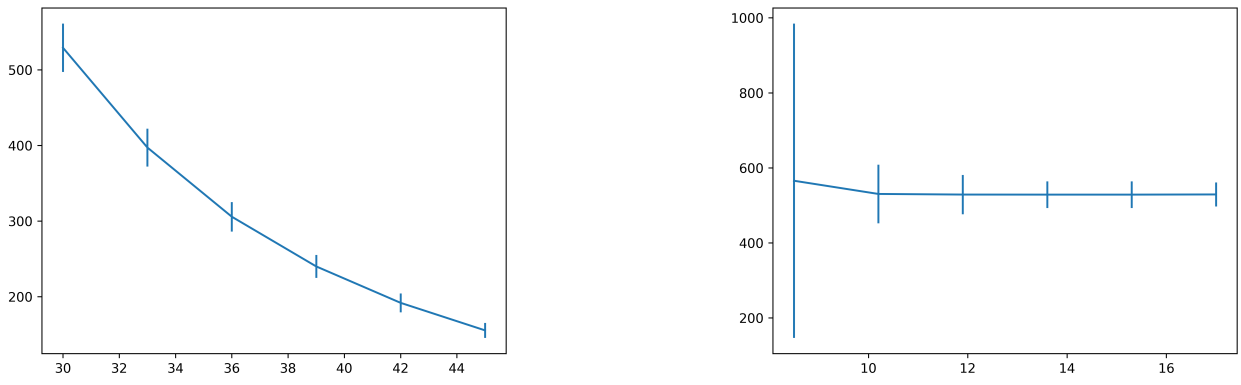

Figure A.1: Left: Sensitivity test for parameter A, showing clear variation. Right: Sensitivity test for parameter B, showing divergence of the standard deviation as the pole tip becomes too narrow

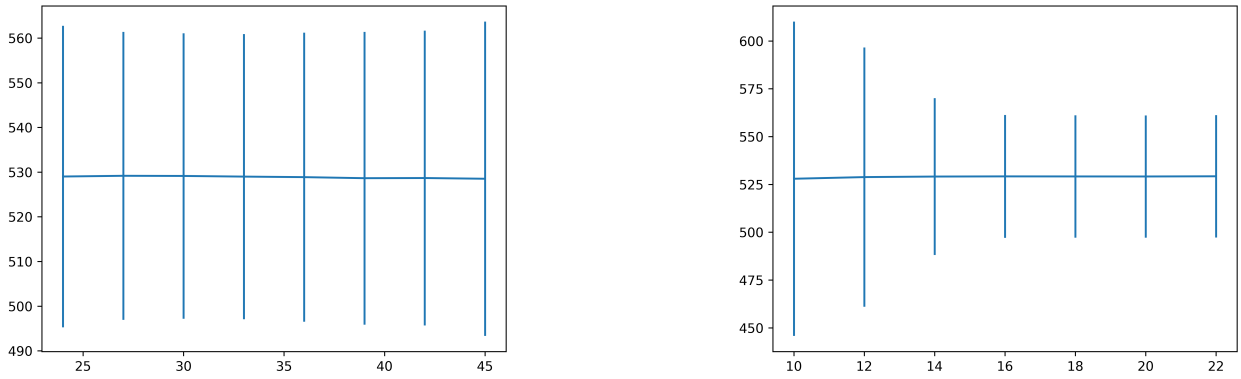

Figure A.2: Left: Sensitivity test for parameter C, showing no variation. Right: Sensitivity test for parameter D, showing reduction in standard deviation with increase in parameter

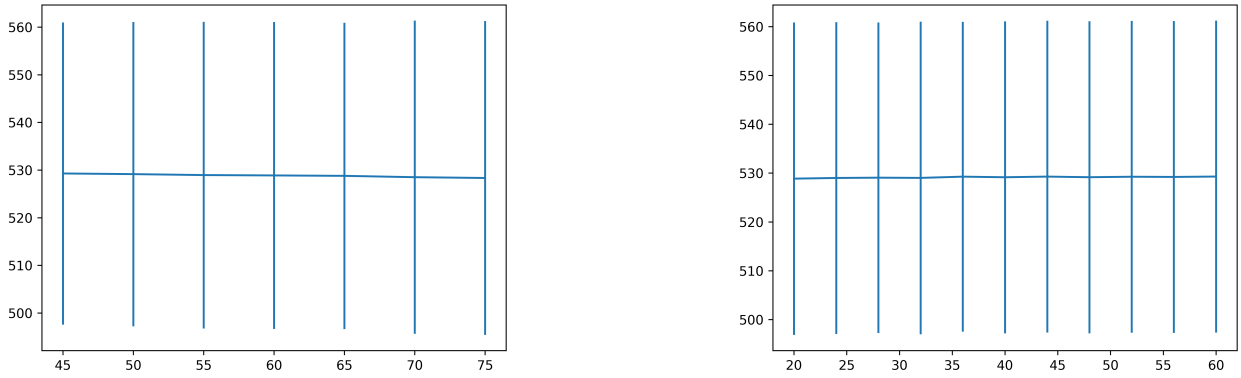

Figure A.3: Left: Sensitivity test for parameter E, showing no variation. Right: Sensitivity test for parameter F, showing no variation

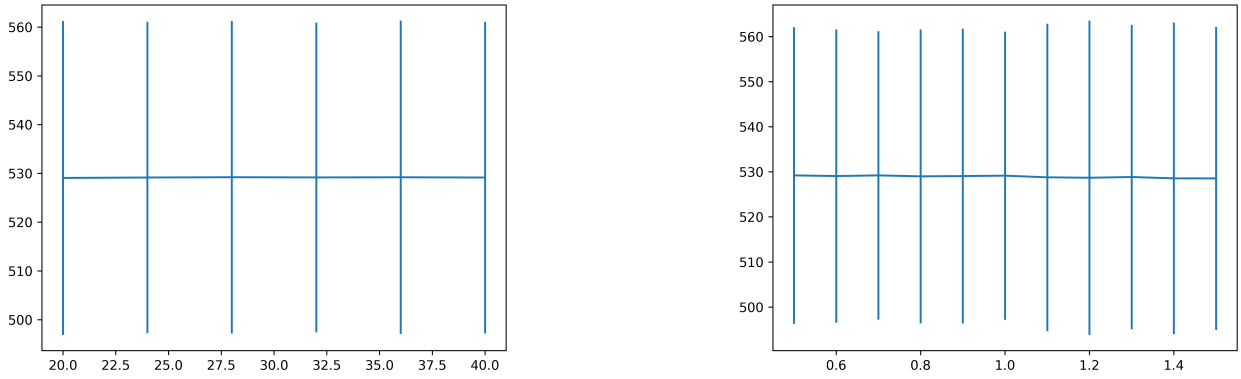

Figure A.4: Left: Sensitivity test for parameter G, showing no variation. Right: Sensitivity test for parameter Hyperbola Step, showing some variation at high values

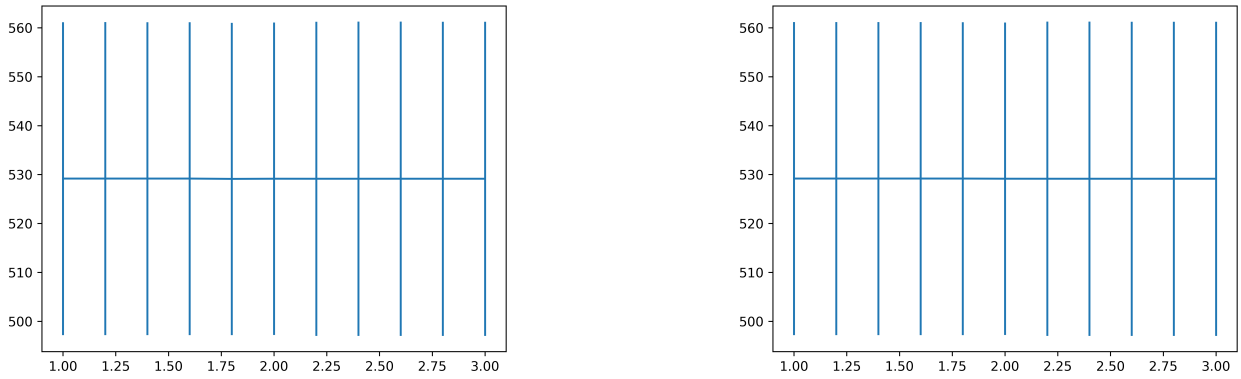

Figure A.5: Left: Sensitivity test for parameter J, showing no variation. Right: Sensitivity test for parameter K, showing no variation

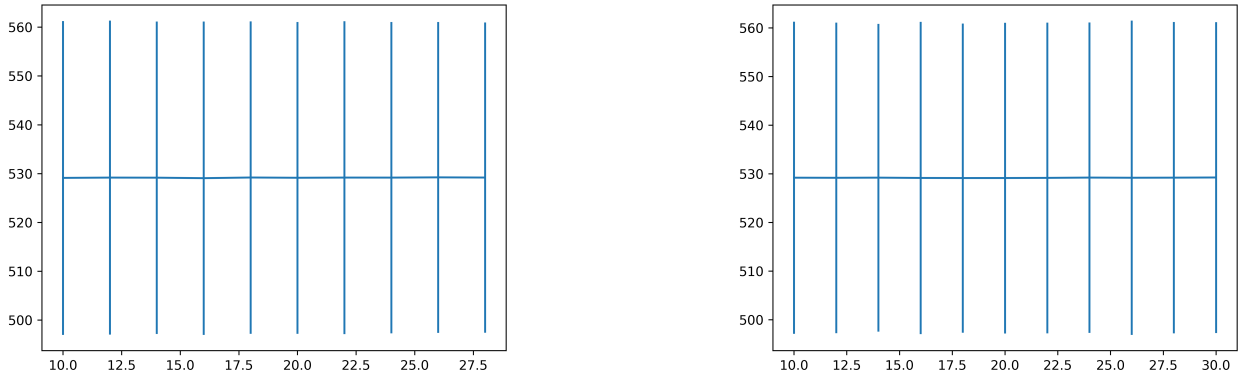

Figure A.6: Left: Sensitivity test for parameter L, showing no variation. Right: Sensitivity test for parameter M, showing no variation

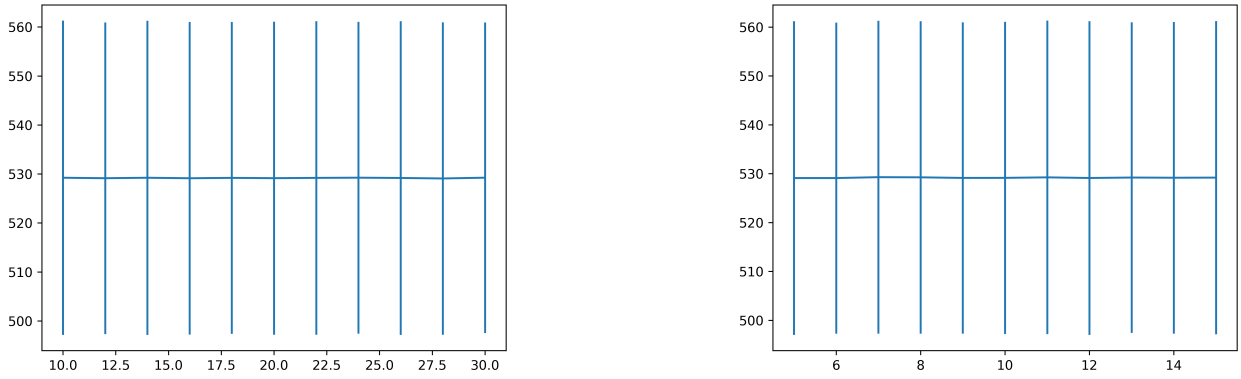

Figure A.7: Left: Sensitivity test for parameter N, showing no variation. Right: Sensitivity test for parameter O, showing no variation

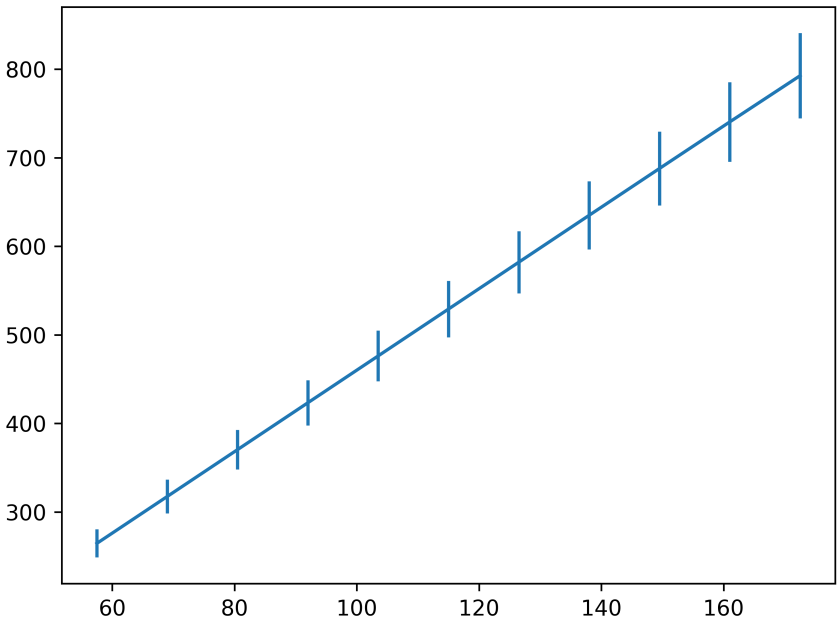

Figure A.8: Sensitivity test for parameter Current, showing a clear linear trend, as expected far from the saturated regime. The standard deviation appears directly proportional to the mean value. This is likely correlated due to the noise that amplifies with the value of the current.

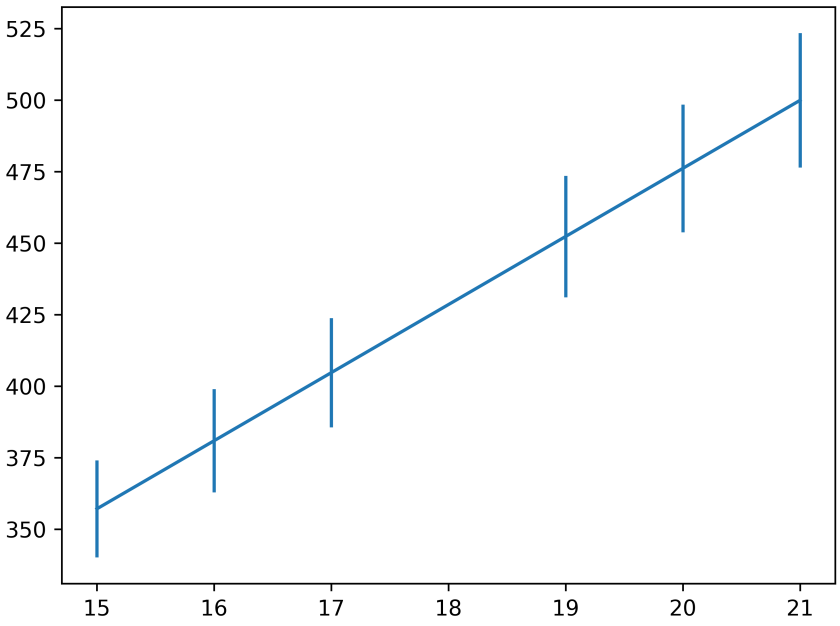

Figure A.9: Sensitivity test for parameter Number of Coils, showing a clear linear trend, as expected far from the saturated regime.

A.2 2D Multipole Analysis Code

```
import numpy as np
import femm

def Multipole_Analyse(
    self,
    no_harmonic_components = 5,
    sp = 200,
    relative_radius = 0.95):
    """
    Multipole coefficient analysis

    Adapted from code by Attilio Milanese (Attilio.Milanese@cern.ch)

    With thanks to Enzo Kuo

    no_harmonic_components: How many harmonics to extract
    sp: Number of sample points
    """

    # Points at every mesh size step along the diameter + tolerance
    points_line = int(2*(self.geometry["beam_pipe_radius"]+1)/(self.meshsize) +1)
    # Define a line to sweep the aperture
    points = np.linspace(
        -(self.geometry["beam_pipe_radius"]+1),
        (self.geometry["beam_pipe_radius"]+1),
        points_line)
    self.points = points

    # Reference radius
    R = self.geometry["beam_pipe_radius"]
    # Set the relative radius as the reference radius
    Rs = self.geometry["beam_pipe_radius"]*relative_radius

    # Maximum value of theta (sextupole sym)
    thmax = np.pi/6
```

```
# Minimum allowed harmonic mode
ihmin = 3
# Step in allowed harmonic modes
ihstep = 6
# Fundamental harmonic mode (same as minimum....)
ihfund = 3
# Caclulate the maximum harmonic
no_harmonics = int(ihmin + (ihstep * no_harmonic_components) + 1)

# Multiplication factor, to include mirror copies
fact = 2*np.pi/thmax

# Angular increment
dth = thmax/(sp-1)

# The below section is completed twice to give the normal and skew components
# Normal Component here
# Sampling Br and A
Br = {}
Ath = {}
# Find the central value (0,0) for reference
A,B1,B2,Sig,E,H1,H2,Je,Js,Mu1,Mu2,Pe,Ph,ff = femm.mo_getpointvalues(0,0)
# Central value of magnetic potential
Actr = A

# Iterate through sample points along a constant radius
for ip in range(1,sp+1):
    # Here this theta is shifted as this magnet is constructed skew
    th = (ip-1)*dth + np.pi/6
    # th = (ip-1)*dth
    xs = Rs*np.cos(th)
    ys = Rs*np.sin(th)
    A,B1,B2,Sig,E,H1,H2,Je,Js,Mu1,Mu2,Pe,Ph,ff = femm.mo_getpointvalues(xs,ys)
    # Radial componenet of magnetic field
    Br[ip] = B1*np.cos(th) + B2*np.sin(th)
    # Theta componenet of magnetic potential
    Ath[ip] = A - Actr
```

```
    # harmonics from A
    Bn = {}
    bn = {}
    for ih in range(1,no_harmonics+1):
        Bn[ih] = 0

    for ih in range(ihmin,no_harmonics,ihstep):
        Bn[ih] = Ath[1]*np.cos(np.pi/6)/2
        for ip in range(2, sp):
            Bn[ih] = Bn[ih] + Ath[ip]*np.cos(ih*((ip-1)*dth + np.pi/6))
        Bn[ih] = Bn[ih] + Ath[sp]*np.cos(ih*(thmax + np.pi/6))/2
        Bn[ih] = fact*Bn[ih]*dth/np.pi*(-ih/Rs)*1000
        Bn[ih] = ((R/Rs)**(ih-1))*Bn[ih]

    self.Multipole_Harmonics_Bn = Bn

    # Repetition here
    # Sampling Br and A
    Br = {}
    Ath = {}
    # Find the central value (0,0) for reference
    A,B1,B2,Sig,E,H1,H2,Je,Js,Mu1,Mu2,Pe,Ph,ff = femm.mo_getpointvalues(0,0)
    # Central value of magnetic potential
    Actr = A

    # Iterate through sample points along a constant radius
    for ip in range(1,sp+1):
        th = (ip-1)*dth
        xs = Rs*np.cos(th)
        ys = Rs*np.sin(th)
        A,B1,B2,Sig,E,H1,H2,Je,Js,Mu1,Mu2,Pe,Ph,ff = femm.mo_getpointvalues(xs,ys)
        # Radial componenet of magnetic field
        Br[ip] = B1*np.cos(th) + B2*np.sin(th)
        # Theta componenet of magnetic potential
        Ath[ip] = A - Actr
```

```
    # harmonics from A
    An = {}
    an = {}
    for ih in range(1,no_harmonics+1):
        An[ih] = 0

    for ih in range(ihmin,no_harmonics,ihstep):
        An[ih] = Ath[1]*np.cos(0)/2
        for ip in range(2, sp):
            An[ih] = An[ih] + Ath[ip]*np.cos(ih*((ip-1)*dth))
        An[ih] = An[ih] + Ath[sp]*np.cos(ih*thmax)/2
        An[ih] = fact*An[ih]*dth/np.pi*(-ih/Rs)*1000
        An[ih] = ((R/Rs)**(ih-1))*An[ih]
    self.Multipole_Harmonics_An = An

    def Field_From_Harmonics(x):
        """
        Calculate the B field along a line from multipoles
        """
        By = np.sum(
        [Bn[harm] * ((x/R)**(harm-1)) for harm in range(ihmin,no_harmonics,ihstep)],
        axis =0
        )
        return(By)

    def Second_Gradient_From_Harmonics(x):
        """
        Calculated B field second derivative from multipoles
        """
        d2bdx2 = np.sum(
        [Bn[harm] * (harm-1) * (harm-2) * (1/R)**2 * ((x/R)**(harm-3))
            for harm in range(ihmin,no_harmonics,ihstep)],
        axis =0
        )
        # Convert to per metres squared
        d2bdx2 = d2bdx2*1000**2
        return(d2bdx2)
```

```
def Field_From_Harmonics_2():
    """
    Returns complex B field By + iBx

    Calculated from multipoles
    """
    X,Y = np.meshgrid(self.points, self.points)
    B = np.sum(
        [(Bn[harm] + 1j * An[harm]) * (((X + 1j * Y)/R)**(harm-1))
            for harm in range(ihmin,no_harmonics,ihstep)],
        axis =0
    )
    return B

def Second_Gradient_From_Harmonics_2():
    """
    Returns complex second derivative of B field By + iBx

    Calculated from multipoles
    """
    X,Y = np.meshgrid(self.points, self.points)
    Grad2 = np.sum(
        [(Bn[harm] + 1j * An[harm])
            * (harm - 1) * (harm - 2) * (1/R**2) * (((X + 1j * Y)/R)**(harm-3))
            for harm in range(ihmin,no_harmonics,ihstep)],
        axis =0
    )
    Grad2 = Grad2*1000**2
    return Grad2
return
```